UC San Diego

UC San Diego Electronic Theses and Dissertations

Title

Biogeochemical Observations in a Southern California Lagoon

Permalink

https://escholarship.org/uc/item/2vb6k6nc

Author

Shipley, Kenisha

Publication Date

2022

Peer reviewed|Thesis/dissertation

eScholarship.org Powered by the California Digital Library
University of California

UNIVERSITY OF CALIFORNIA SAN DIEGO

Biogeochemical Observations in a Southern California Lagoon

A dissertation submitted in partial satisfaction of the
requirements for the degree Doctor of Philosophy

in

Earth Science

by

Kenisha Marie Shipley

Committee in charge:

Professor Todd R. Martz, Chair
Professor Lihini Aluwihare
Professor Andreas Andersson
Professor Sarah Giddings
Professor Ryan Kastner

2022

Copyright

Kenisha Marie Shipley, 2022
All rights reserved.

The Dissertation of Kenisha Marie Shipley is approved, and it is acceptable in quality and form for publication on microfilm and electronically:

University of California San Diego

2022

DEDICATION

To my husband and daughter who have supported and encouraged me throughout this journey.

EPIGRAPH

If there is no struggle, there is no progress.

-Frederick Douglass

TABLE OF CONTENTS

LIST OF FIGURES

LIST OF TABLES

ACKNOWLEDGEMENTS

I am forever grateful to God, my family, and friends who have continually shown their support and encouragement over the years. I would like to thank my advisor, Todd Martz for giving me the opportunity to work in his lab and for providing mentorship and guidance over the years. I have learned so much from him and truly appreciate his support.

I would also like to thank my dissertation committee, Lihini Aluwihare, Sarah Giddings, Andreas Andersson, and Ryan Kastner for their feedback and inquisitive questions to help me grow as a scientist and researcher. I am also grateful for the past and current members of the Martz lab for their friendship and support. They have helped me so much during my time here and made my experience at Scripps even better. Thank you to my MCG cohort for their friendship, support, and constant encouragement. You all are amazing!

I would especially like to thank my husband Jacques who has been with me every step of the way and been my number one supporter. I could not have done this without you. Your motivation, words of wisdom, and love have meant everything to me. Finally, thank you to my baby Rayne for inspiring me to be the best mom and person I can and for loving me unconditionally. I love you and daddy the most.

=====

Chapter 2, in full is currently being prepared for publication as: Shipley, K., Martz, T., Hales, B., Giddings, S., Andersson, A. (2022) Physical and Biological Controls on the Seasonal CO_2 Cycle in the Agua Hedionda Lagoon. Carlsbad, CA. The dissertation author was the primary investigator and first author of this paper.

Chapter 3, in full has been submitted for publication as: Shipley, K., Martz, T., Bresnahan, P., and Wirth, T. (2022) Metabolic Rates in the Agua Hedionda Lagoon during a Southern California red tide event. *Elementa*. The dissertation author was the primary investigator and first author of this paper.

VITA

2012	Bachelor of Science in Chemistry
	San Diego State University
2014	Master of Science in Environmental Science
	California State University, Los Angeles
2022	Doctor of Philosophy in Earth Science
	Scripps Institution of Oceanography University of California San Diego

PUBLICATIONS

1. Wolfe, W.H, Shipley, K., Bresnahan, P.J., Takeshita, Y., Wirth, T., Martz, T.R. (2021). Technical Note: Stability of tris pH buffer in artificial seawater stored in bags. Ocean Science. 10.5194/os-17-819-2021.

2. Bresnahan, P.J., Wirth, T., Martz, T.R., Shipley, K., Rowley, V., Anderson, C., Grimm, T. (2020). Equipping Smart Coasts with Marine Water Quality IoT Sensors. Results in Engineering. DOI:10.1016/j.rineng.2019.100087.

ABSTRACT OF THE DISSERTATION

Biogeochemical Observations in a Southern California Lagoon

by

Kenisha Marie Shipley

Doctor of Philosophy in Earth Science

University of California San Diego, 2022

Todd Martz, Chair

Estuarine environments are uniquely diverse coastal subsystems located at the land-river-ocean interface. Across different systems, carbon dioxide (CO_2) parameters and anthropogenic inputs can vary greatly given the heterogeneity between individual estuarine systems, which makes it difficult to characterize coastal ocean systems as a whole. The Agua Hedionda Lagoon (AHL) is a tidal estuary located on the southern California coast, which supports a diverse ecosystem while serving numerous

recreation activities, a marine fish hatchery, a shellfish hatchery (Carlsbad Aquafarm, CAF), and the largest desalination plant in the western hemisphere.

This dissertation contains three main chapters. Chapter 1 provides the information about sampling design and instrumentation used for biogeochemical data collection at the AHL. The detailed steps and procedures required for quality control and processing of the data are also included. In Chapter 2, a one-year time series of carbon dioxide (CO_2) data is used to establish baseline and seasonal average inorganic carbon conditions in the AHL. Based on a mass balance model of the lagoon, we propose that the outer lagoon of the AHL is a source of inorganic carbon to the adjacent ocean, through advective export, and a direct source of CO_2 to the atmosphere. In Chapter 3, a time series from autonomous sensors deployed in AHL captured the effects of a massive red tide occurring along the Southern & Baja California coast during the spring of 2020. Biogeochemical data (pH and O_2) were examined using an open-source model designed to filter out the influence of tides and estimate net ecosystem metabolism (NEM). Contemporaneous pH and O_2 observations allowed simultaneous, independent evaluations of production, respiration and NEM.

Introduction

Coastal marine systems are uniquely diverse environments and often exhibit great biogeochemical heterogeneity (Bauer et al., 2013; Paulsen et al., 2018). These coastal systems are affected by many of the same sets of local drivers, including the adjacent ocean and surrounding landscape through runoff and river discharge (Paerl et al., 2006; Howarth et al., 2011; Windham-Myers et al., 2018). In comparison to offshore ecosystems, near-shore ecosystems are more often subjected to anthropogenic stressors, which makes understanding the metabolic state of these systems of great importance (Hewitt et al., 2005). Semi-enclosed coastal systems (e.g. estuaries, lagoons, intertidal zones, wetlands) are important to a wide number of natural processes in addition to societal and commercial uses (Ramesh et al., 2015). In many cases, the proximity to civilization makes the ecosystems operating within these coastal systems highly influenced by anthropogenic effects such as eutrophication from nutrient loading and habitat loss due to land use change (Bauer et al., 2013; Howarth et al., 2011; Windham-Myers et al., 2018). In addition to these long-recognized issues, climate change (warming, acidification, deoxygenation) in the coastal ocean (Hauri et al., 2009; Gruber et al., 2012; Kessouri et al., 2021) and shallow coastal systems (Feely et al., 2010; Waldbusser et al., 2014; Cai et al., 2021) is now a well-established area of research.

Over the past decade observation programs have become particularly important in coastal systems, particularly in the Pacific Northwest due to an upwelling event in 2009, which led to unambiguous demonstration that oyster larval mortality was impacted by abnormally low saturation state of the intake water at a commercial shellfish hatchery (Barton et al., 2012). This observation along with other studies (Waldbusser et. al., 2015, Doney et.al., 2020) documenting the sensitivity of shelled organisms to increased dissolved CO_2 and acidification has led to the installment of continuous flow, shore station systems which measure the aqueous CO_2 chemistry parameters at various shellfish hatcheries and aquafarms along the Pacific coast. This initiative was part of the Integrated Ocean Observing System (IOOS) program through NOAA, to provide real-time information to assist local

stakeholders and shellfish growers on the CO_2 content of the waters at the intake of the aquafarms and shellfish hatcheries. Understanding the carbonate system is also an important step in attempting to constrain net fluxes on a more global scale which requires better estimates from semi-enclosed coastal lagoons and estuaries (e.g., Cai, 2011; Wang et al., 2016). Existing studies are limited and those that exist have a wide range of flux estimates and thus are not well constrained (Cai, 2011; Paulsen et al., 2018).

In this work, we make biogeochemical observations at the Agua Hedionda Lagoon, an urbanized lagoon located in Carlsbad, CA, making up a total of about 1.6×10^6 m^2 along the Southern California coastline. The original wetland was converted into the present lagoon structure in 1954 by the Encina Power Station and is maintained in its present form by semi-annual dredging. The lagoon is comprised of three interconnected basins, including an outer (26.7×10^4 m^2), middle (10.9×10^4 m^2), and inner basin (1.2×10^6 m^2) (Figure 1) (Elwany et al., 2005). The Ocean, connected by an inlet located on the western side of the outer basin, dominates physical forcing in all three basins, with tidal lags of up to 4 hours at the creek (Jenkins and Wasyl, 2006). The inner basin receives freshwater input from Agua Hedionda Creek during rain events which occur primarily in winter and spring. During the rest of the year, the creek is dry, and the lagoon is purely tidal.

The AHL is highly utilized and a popular destination for the Carlsbad community and tourists and provides a thriving ecosystem for many diverse species of plants and animals. There are two primary industrial features, which include the Encina Power Station (fully decommissioned by January 2019) and the Carlsbad Desalination Plant, both of which rely on water intake from the outer basin for once-through cooling of the power plant and as desalination source water. Other features of the AHL include agriculture (primarily strawberry fields bordering the inner basin), the Hubbs-SeaWorld Marine Fish Hatchery, which breeds white seabass, and the Carlsbad Aquafarm (CAF)—a sustainable mussel and oyster farm, which operates in the outer basin. Both the fish hatchery and aquafarm (which grows calcifying organisms sensitive to pH) rely on adequate flushing of the lagoon by the ambient ocean in order to maintain oxygen and calcium carbonate saturation levels above thresholds critical to growth.

The CAF, which was the primary location of our observations, has been in operation since 1990 as a sustainable aquaculture facility that uses a suspension system method to culture mussels and oysters. The aquafarm typically raises over one million pounds of Mediterranean Blue Mussels (*Mytilus edulis*) and Pacific oysters (*Crassostrea gigas*) every year. In order to maintain the quality and quantity of shellfish production for the community, local restaurants, and wholesale industry, the CAF is reliant on the condition of the lagoon's water chemistry. Mussels and oysters are filter feeders and rely on clean water that is free of contaminants and waste build up. Accordingly, it is important for aquafarms to operate in well-flushed lagoons and/or actively pump water from the nearby ocean into the aquafarm for water quality purposes. This dissertation improves our understanding of the baseline chemical distribution and variability in estuarine systems by implementing spatio-temporal measurements of biogeochemical observations for the conservation of lagoon systems in a changing climate.

References

Barton A, Hales B, Waldbusser GG, Langdon C, Feely RA. 2012. The Pacific oyster, Crassostrea gigas, shows negative correlation to naturally elevated carbon dioxide levels: Implications for near-term ocean acidification effects. *Limnology and Oceanography* **57**(3): 698–710. doi: 10.4319/lo.2012.57.3.0698

Bauer JE, Cai W-J, Raymond PA, Bianchi TS, Hopkinson CS, Regnier PAG. 2013. The changing carbon cycle of the coastal ocean. *Nature* **504**(7478): 61–70. doi: 10.1038/nature12857

Cai W-J. 2011. Estuarine and coastal ocean carbon paradox: CO2 sinks or sites of terrestrial carbon incineration? *Annual review of marine science* **3**: 123–45. doi: 10.1146/annurev-marine-120709-142723

Cai WJ, Feely RA, Testa JM, Li M, Evans W, Alin SR, Xu YY, Pelletier G, Ahmed A, Greeley DJ, Newton JA, Bednarscaronek N. 2021. Natural and Anthropogenic Drivers of Acidification in Large Estuaries. *https://doi.org/101146/annurev-marine-010419-011004* **13**: 23–55. Annual Reviews . doi: 10.1146/ANNUREV-MARINE-010419-011004

Doney SC, Busch DS, Cooley SR, Kroeker KJ. 2020. The impacts of Ocean acidification on marine ecosystems and reliant human communities. *Annual Review of Environment and Resources* **45**: 83–112.

Elwany H, Flick R, White M. 2005. Agua Hedionda Lagoon hydrodynamic studies.

Feely RA, Alin SR, Newton J, Sabine CL, Warner M, Devol A, Krembs C, Maloy C. 2010. The combined effects of ocean acidification, mixing, and respiration on pH and carbonate saturation in an urbanized estuary. *Estuarine, Coastal and Shelf Science* **88**(4): 442–449. doi: 10.1016/j.ecss.2010.05.004

Gruber N, Hauri C, Lachkar Z, Loher D, Frolicher TL, Plattner G-K. 2012. Rapid Progression of Ocean Acidification in the California Current System. *Science* **337**(6091): 220–223. doi: 10.1126/science.1216773

Hauri C, Gruber N, Plattner G-K, Alin S, Feely RA, Hales B, Wheeler PA. 2009. Ocean acidification in the California current system. *Oceanography* **22**(4): 60–71.

Hewitt JE, Anderson MJ, Thrush SF. 2005. Assessing and monitoring ecological community health in marine systems. *Ecological Applications* **15**(3): 942–953. doi: 10.1890/04-0732

Howarth R, Chan F, Conley DJ, Garnier J, Doney SC, Marino R, Billen G. 2011. Coupled biogeochemical cycles: Eutrophication and hypoxia in temperate estuaries and coastal marine ecosystems. *Frontiers in Ecology and the Environment* **9**(1): 18–26. doi: 10.1890/100008

Jenkins SA, Wasyl J. 2006. Coastal Processes Effects of Reduced Intake Flows at Agua Hedionda Lagoon.

Kessouri F, McWilliams JC, Bianchi D, Sutula M, Renault L, Deutsch C, Feely RA, McLaughlin K, Ho M, Howard EM, Bednaršek N, Damien P, Molemaker J, Weisberg SB. 2021. Coastal eutrophication drives acidification, oxygen loss, and ecosystem change in a major oceanic upwelling system. *Proceedings of the National Academy of Sciences of the United States of America* **118**(21): 1–8. doi: 10.1073/pnas.2018856118

Paerl HW, Valdes LM, Peierls BL, Adolf JE, Harding LW. 2006. Anthropogenic and climatic influences on the eutrophication of large estuarine ecosystems. *Limnology and Oceanography* **51**(1 II): 448–462. doi: 10.4319/lo.2006.51.1_part_2.0448

Paulsen M-L, Andersson AJ, Aluwihare L, Cyronak T, D'Angelo S, Davidson C, Elwany H, Giddings SN, Page HN, Porrachia M, Schroeter S. 2018. Temporal changes in seawater carbonate chemistry and carbon export from a Southern California estuary. *Estuaries and Coasts* **41**(4): 1050–1068. doi: 10.1007/s12237-017-0345-8

Ramesh R, Chen Z, Cummins V, Day J, D'Elia C, Dennison B, Forbes DL, Glaeser B, Glaser M, Glavovic B, Kremer H, Lange M, Larsen JN, Le Tissier M, Newton A, Pelling M, Purvaja R, Wolanski E. 2015. Land-Ocean Interactions in the Coastal Zone: Past, present & future. *Anthropocene* **12**(2015): 85–98. Elsevier B.V. doi: 10.1016/j.ancene.2016.01.005

Waldbusser GG, Hales B, Langdon CJ, Haley BA, Schrader P, Brunner EL, Gray MW, Miller CA, Gimenez I. 2015. Saturation-state sensitivity of marine bivalve larvae to ocean acidification. *Nature Climate Change* **5**(3): 273–280. doi: 10.1038/NCLIMATE2479

Waldbusser GG, Salisbury JE. 2014. Ocean Acidification in the Coastal Zone from an Organism's Perspective: Multiple System Parameters, Frequency Domains, and Habitats. *Annual Review of Marine Science* **6**(1): 221–247. doi: 10.1146/annurev-marine-121211-172238

Wang ZA, Kroeger KD, Ganju NK, Gonneea ME, Chu SN. 2016. Intertidal salt marshes as an important source of inorganic carbon to the coastal ocean. *Limnology and Oceanography* **61**(5): 1916–1931. doi: 10.1002/lno.10347

Windham-Myers L, Cai W-J, Alin SR, Andersson A, Crosswell J, Dunton KH, Hernandez-Ayon JM, Herrmann M, Hinson AL, Hopkinson CS, Howard J, Hu X, Knox SH, Kroeger K, Lagomasino D, Megonigal P, Najjar RG, Paulsen M-L, Peteet D et al. 2018. Tidal wetlands and estuaries. Second state of the carbon cycle report (SOCCR2): A sustained assessment report. doi: 10.7930/soccr2.2018.ch15

Chapter 1: Field Sampling and Observations in the Agua Hedionda Lagoon

1.1. Abstract

Estuarine environments are uniquely diverse coastal subsystems located at the land-river-ocean interface. Across different systems, carbon dioxide (CO_2) parameters and anthropogenic inputs can vary greatly given the heterogeneity between individual estuarine systems, which makes it difficult to characterize coastal ocean systems without continuous, long-term observations. The Agua Hedionda Lagoon (AHL) is a highly dynamic lagoon subject to impacts from the surrounding urbanization, land use, and densely populated community. This chapter will focus on the technical details of the observational techniques and sensors used for the collection of data at the AHL. It will also describe the various methods used for quality control (QC) and processing of the collected data from a continuous flow-through carbon dioxide (CO_2) instrument and in-situ mooring sensors. AHL data was collected intermittently from 2015 through 2018 with the CO_2 instrument and during periods from 2018 to 2020 with the in-situ sensors. Descriptions of each instrument including measurements made and sampling mechanisms are provided, as they were an integral part of the data collection and are specific to the instruments used in this research. In addition, the steps taken for QC and data processing required for each dataset are described in detail below.

1.2. Introduction

Understanding the various physical and chemical processes within a coastal ecosystem requires obtaining quality data with a certain level of accuracy (Dickson, 2010; Pierrot et al., 2009). There are standard practices and guidelines for the collection and processing of oceanographic data, in order to achieve a dataset with a certain level of uncertainty. For this research, the uncertainties achieved were in line with weather objective goals, which can be used to establish baseline conditions and address many aspects of the carbon budget and biogeochemical parameters in highly variable coastal marine environments. Field sampling was conducted at the Agua Hedionda Lagoon (AHL) (Figure 1.1) and implemented the use of two instruments to achieve long-term and continuous measurements within a coastal environment.

The automated CO_2 instrument (Figure 1.2) was in operation at the AHL (Figure 1.1) from 2015-2018 and provided long term, continuous measurements including partial pressure of CO_2 (pCO_2), dissolved inorganic carbon (DIC), pH, temperature, and salinity. The in situ mooring sensors (Figure 1.3), which included a SeapHOx and miniDOT were deployed at various locations within the AHL at different periods from 2018-2020 (see Table 1.1) and made biogeochemical measurements, which included dissolved oxygen (DO), temperature, salinity, pH, and pressure. The following sections are dedicated to describing the various steps taken to QC and process data to obtain high quality datasets used in the analyses performed in chapters 2 and 3 of this dissertation.

1.3. Materials and Methods

1.3.1. CO_2 Instrument Sampling

The CO_2 instrument (Figure 1.2) is an autonomous instrument developed by Prof. Burke Hales at OSU, which measures the aqueous CO_2 parameters in a continuous flowing seawater stream. The measured CO_2 parameters include pCO_2, DIC, pH, temperature, salinity, total alkalinity (A_T), and the saturation state of aragonite (Ω_{Arag}). This system was installed at the Carlsbad Aquafarm (CAF), located in the outer basin of the AHL with an intake near the docks of the CAF at 1 m below the surface (Figure 1.1). The lagoon water was pumped through about 25 m of PVC piping to a small lab at the CAF where the CO_2 instrument was housed. The incoming lagoon water is first filtered through a nylon screen T-strainer to remove large debris from the sample water, which then passes through a line containing a Honeywell 4905 conductivity probe and a Honeywell Durafet sensor to obtain in situ salinity, temperature, and pH (total scale) measurements. Water then enters an enclosed headspace showerhead equilibrator, which contains a bubbling tube to facilitate equilibration of the CO_2 between the headspace and water (Fairchild and Hales, 2021, Hales et al., 2004). The CO_2 gas is circulated to a LI-820A non-dispersive infrared (NDIR) detector to measure the mole fraction of the CO_2 (xCO_2) gas. At hourly intervals, the instrument switches to DIC mode and the sample water flows through a separate DIC sample line where it passes through a stainless-steel tangential flow filter to remove micron size particles from the sample water. The filtered sample water is then acidified with 10% hydrochloric acid (HCl) and

is passed through a mixing coil. The acidified sample water flows through the inside of a hydrophobic gas permeable membrane contactor (Liqui-Cel, G543), while simultaneously, a CO_2 free gas flows opposite of the liquid stream at a specified flow rate on the outside of the membrane contactor. The effluent CO_2 gas is extracted, then dried, and directed to the NDIR detector to determine the xCO_2 (Bandstra et al., 2006) and obtain the DIC of the sample water. Additional CO_2 system calculations for A_T and Ω for aragonite and calcite are performed within the LabView program which operates through the instrument's computer. The sample frequency and storage of the data were specified at 15 sec intervals for in situ and pCO_2 data, and hourly intervals for DIC and calculated parameters.

The CO_2 system required regular maintenance including daily cleaning of the T-strainer, monthly flushing of the sample lines with bleach and hydrochloric acid to remove biological material and build-up within the tubing, and bi-monthly liquid DIC standard and HCl acid preparation. The system was also monitored daily via remote desktop to monitor real-time data to identify any discrepancies or issues with the measurements. The data collected using this instrument occurred from 2015-2018 with many gaps and inconsistencies in data over the first several years due to repairs and power failures and in Jan 2019, the instrument was taken offline. Data collected from Dec 2017 to Dec 2018 provided the most consistent dataset, which was used in the following, chapter 2 analyses.

1.3.2. In-situ Mooring Sampling

The in-situ mooring consists of two primary sensors that measure multiple biogeochemical properties. The diagram in Figure 1.3 provides the schematic of the deployed mooring, which includes an oxygen-temperature logger (PME miniDOT) to measure temperature and dissolved oxygen (DO) at the surface and a SeapHOx sensor package to measure pH (Honeywell Durafet), DO (Aanderaa optode), temperature and salinity (Sea-Bird SBE-37) and pressure (Honeywell M5200 series) at depth (Bresnahan et al., 2014). Both sensors were set to make measurements at 30-minute intervals. The surface buoy shown in the diagram, houses a cellular modem and controller connected directly to the SeapHOx, allowing hourly updated, real-time data access (Bresnahan et al., 2020). The SeapHOx data were made publicly available by the Southern California Coastal Ocean Observing System (SCCOOS) through an

online database (ERDDAP): see https://sccoos.org/ocean-acidification/ and https://erddap.sccoos.org/erddap/tabledap/pH-AHL.html. The lagoon moorings were deployed in the outer basin and middle basin, and an additional mooring was deployed with Prof. Uwe Send's group approximately 1 mile offshore from the AHL, which had a slightly different design as it was deployed in the Ocean, but included the same sensors shown in Figure 1.3. Mooring deployment began August 2018 with dates and lengths of deployment shown in Table 1.1. The data were monitored using the real-time observation capabilities to determine when recovery was necessary and on average, was after the sensor had been deployed for 3-4 months, except in 2020 where the mooring was deployed closer to 5-months due to the pandemic restrictions. Locations of the deployments were chosen based on several factors including accessibility, depth, and flow (ideally low to moderate in order to minimize mooring drag due to tidal current).

1.3.3. Data Processing and QC

CO_2 Instrument

This section describes the detailed steps that were implemented for the QC and processing of the dataset used in chapter 2. The CO_2 instrument undergoes a real-time automated calibration sequence using CO_2 gas and DIC liquid standards every 6 hours. The concentrations of the set of gas standards are 200, 800, and 1500 µatm which were purchased from Scott-Marin and provided in gas cylinders. The set of DIC liquid standards contained a solution mixture of ultrapure water (>18 MΩ resistivity), sodium bicarbonate-$NaHCO_3$, oven dried sodium carbonate-Na_2CO_3 and 0.1 M HCl. The standards were gravimetrically prepared at the Scripps Institution of Oceanography (SIO) in concentrations of 1900, 2100, and 2300 µmol kg^{-1} every 12-14 days and stored in custom made gas impermeable Mylar bags (IMPAK P75C0919). As further described in (Fairchild and Hales, 2021), during a gas calibration sequence, a linear regression is performed in real-time to verify the accuracy of the NDIR detector and apply a correction to the respective pCO_2 data to account for any offsets in the raw xCO_2 measurements. It is also during the gas standard sequence that an atmospheric CO_2 measurement is made from a separate

line that extends outside. The liquid standard sequence occurs directly after the gas standards and also produces a linear regression in real-time. While the gas standard regressions typically achieved high linearity with $R^2 = 0.999$ or better, the liquid standards frequently experienced $R^2 \leq 0.999$. In cases where linearity was lower in the liquid standard regression, it was identified that when the liquid standard bags became too low or if air was trapped inside the bag, air bubbles were able to enter the line. This resulted in additional QC steps in post processing which are described below.

Bottle samples were collected monthly from the main sample water line of the instrument into 250 mL borosilicate bottles (3x rinsed and filled) for laboratory analyses on the benchtop density meter (Mettler-Toledo DM45) which was calibrated with seawater and an air measurement. The density measurement was converted to salinity (PSU) using the density conversion function from the GSW toolbox in MATLAB. The recorded instrument salinity and density meter salinity were compared and any difference between the two was applied via remote desktop access where the adjusted data were then automatically stored in an output file. Salinity corrections were only applied if the check sample salinity was off by more than ±0.05. Bottle samples were also collected and poisoned with mercuric chloride for DIC and pH validation. A total of 4 bottle samples were collected and analyzed on the benchtop spectrophotometric pH system and the DIC analyzer which were compared against certified reference materials (CRMs) (Table 1.2). A pH offset of -0.18 was applied directly to the durafet sensor output in April 2018 based on bottle sample analyses and this offset was also applied to the Dec. 2017 – April 2018 to bring the full pH timeseries into agreement (Figure 1.4). Bottle samples analyzed in 2019 determined an insignificant drift in pH (< 0.005) and no additional pH offsets were applied.

As mentioned previously, there were additional steps required to QC the DIC data based on bad calibration data that were applied to the raw DIC data, resulting in significant step changes (Figure 1.5). A monthly running average of the calibration data from liquid and gas standards, which include the slope and intercept, were taken for the full year, and the DIC is recalculated using the following equation,

$$DIC = \frac{(\boldsymbol{xCO_2} \times \boldsymbol{g_{cal}m} + \boldsymbol{g_{cal}b})(\boldsymbol{liq_{cal}m} + \boldsymbol{liq_{cal}b})}{\boldsymbol{\rho_{sw}}} \quad (1.1)$$

where xCO_2 is the mole fraction of CO_2 measured during hourly DIC measurements, multiplied by the sum of the gas and liquid calibration slopes and intercepts, and divided by the seawater density. This leveled out the DIC date to more reasonable values. The remaining step taken to QC the DIC data utilized the analyses of bottle samples described above, on the benchtop DIC analyzer, which was calibrated using CRM's. Three bottle samples were analyzed and revealed an offset in the corrected instrument DIC and 20 µmol kg^{-1} were added to the final DIC dataset to account for the difference (Figure 1.6). The initial instrument pCO_2 measurements were determined to be compromised (Figure 1.7) due to an air leak and the final pCO_2 dataset analyzed in this study was derived in CO2SYS from the QC'd DIC and pH data. The additional calculated parameters including A_T and Ω_{arag} were also recalculated in CO2SYS using the QC'd DIC and pH data (Figure 1.8 and 1.9).

Prior to analyses, all data were processed using a 30-d low pass filter (LPF) using the *filtfilt* MATLAB function to isolate the seasonal cycle and a 24 hr LPF to remove the daily variability and or noise, except temperature, which required a 7-d LPF due to diel temperature amplitude measured by the instrument being unduly high. The source of this problem was a delivery line from the lagoon to the instrument, extended across the roof of a building where the line underwent excessive heating throughout the day. Based on in situ mooring measurements in the lagoon the LPF instrument temperature agrees with average lagoon temperature, making the LPF temperature a viable approximation of the lagoon.

In-situ Mooring

While additional data were collected (see Figure 1.10), the following steps described are those applied to outer basin sampling from the SeapHOx during Nov-Dec 2018 and Feb-June 2020, which are used in chapter 3 analyses. Prior to each mooring deployment, the SeapHOx undergoes pre-conditioning to test the sensor accuracy and obtain a set of internal calibration coefficients, which are used to derive the pH upon recovery of the mooring (Bresnahan 2014). Due to a discrepancy between the January 2020

and August 2019 calibration points, the previous calibration points from 2019 were used in the initial calculations of pH, which produced more reasonable pH values based on additional data observed in the lagoon (Figure 1.11). Initial processing of the raw, 30-minute data included interpolating data to a common hourly timestamp. It was also observed for 2020 data that during the first two weeks the sensors were still conditioning (based on measurements being out of agreement with the remaining time series) and this period was removed to begin the time series on Feb. 5th. Raw oxygen data were salinity corrected, using data from the SBE-37 following the equation from the Aanderaa manufacturer manual,

$$O_{2C} = [O_2] \cdot e^{(S-S_0)(B_0 + B_1 T_S + B_2 T_S^2 + B_3 T_S^3) + C_0 (S^2 - S_0^2)} \quad (1.2)$$

where, S is measured salinity, and $B_{0,1,2,3}$ and $C_{o\ are}$ constants and Ts is measured temperature converted to Kelvin. The final DO dataset used in the chapter 3 analyses were converted to mg L^{-1}.

Validation samples were collected during the recovery of the mooring at the beginning of 2019 but were not possible in 2020 due to restrictions associated with the pandemic. For a bottle validation sample, a Niskin was filled near the sensor and then subsampled into a 250 ml borosilicate bottle and poisoned with mercuric chloride ($HgCl_2$). The sample was later analyzed for pH using a benchtop spectrophotometric pH system. This bottle sample measurement is used to adjust the mooring pH values by applying a constant offset determined at the time of sampling, which is corrected to in situ temperature from the mooring at the time of bottle collection. This offset was applied to the 2018 dataset, but because the pandemic did not allow for validation samples during the 2020 deployment, the pH sensor offset determined in 2019 was also carried forward for the 2020 dataset (the same Durafet pH sensor was used in the SeapHOx). Based on our previous experience, we estimate the accuracy of the time series to be 0.05 pH, and in line with the manufacturer's stated accuracy for oxygen (±2 mmol m^{-3}) and salinity (±0.003).

CO_2 system calculations to derive DIC and pCO_2 were performed using CO2SYS for MATLAB (van Heuven et al., 2011), using equilibrium constants as recommended by (Dickson and Millero, 1987). Phosphate and silicate as inputs to CO2SYS were set to zero because, although they were not measured in this study, a brief campaign in 2016 observed concentrations in these nutrients at levels (maximum observed: Phosphate = .35 µmol L^{-1}; Silicate = 6.7 µmol L^{-1}) that are near-negligible in their effect on pH (~0.001 pH unit). The derived parameters use measured temperature, salinity, pH, and a local A_T-S relationship was established from data recorded during a runoff event in 2018 where five paired pH and DIC measurements were used to establish the relationship: A_T (µmol kg^{-1}) = 29.2×S+1238 (RMSE = 6.3, R^2 = .98, n = 5).

1.4. Conclusions

The data processing involves a series of straightforward steps that currently require a fair amount of manual data manipulation. Automating this process on any level will increase our efficiency, given that data QC were a critical component of obtaining finalized datasets for analyses in chapters 2 and 3. Although there were several methods utilized, the collection and analyses of bottle samples provided the most accurate source for determining and applying offsets in pH and DIC space. The CO_2 instrument's automated slope-intercept corrections for pCO_2 and DIC through the standard calibration sequences were a useful step for implementing data QC in real-time. However, the step changes in DIC measurements that continually arose as a result of a bad liquid standard calibration resulted in additional QC steps, which under ideal circumstances would not have been required. This issue was unusual and was in most cases, a result of bags being depleted before replacement liquid standards were ready. An additional and likely explanation is that the positioning of the bags (laying flat, see Figure 1.2) impacted the flow from out of the bag during a liquid standard sequence or in some cases due to bags not being completely free of excess air after being filled with the standards. While this issue was inconvenient, the real-time access to the data through remote desktop allowed this issue to be seen and addressed in a timely manner. Unfortunately, the gas leak issues that arose with pCO_2 were not identifiable remotely, but the issues were potentially preventable if there had been additional steps in place to check and compare seawater pCO_2

and atmospheric CO_2 measurements on a regular basis by plotting these specific parameters. This additional check would have allowed the operator to see that seawater pCO_2 levels were very similar to atmospheric pCO_2 which is a clear indicator of a leak (e.g., pCO_2 gas escaping before being measured on the NDIR detector) or other issue that needs to be addressed. While, certain checks are implemented to identify leaks, they are difficult to pinpoint and thus can go on for long periods as in the case of 2018 measurements.

A total of three sensors were used to obtain field measurements with each sensor requiring different steps for downloading and processing data. Streamlining steps to incorporate multiple sensors, specifically for merging, averaging, and interpolating data to a common timestamp is a particularly critical first step. Future sampling efforts would benefit from a more standardized process since timestamp errors can be particularly problematic and difficult to identify immediately. The in-situ mooring did not require the same degree of technical oversight when deployed, compared to the CO_2 instrument. One downfall, regarding data QC was that accessibility to the mooring was reliant on CAF staff, which prevented more bottle samples to be collected during deployments. The mooring design element, which allowed the almost real-time data access was a novel feature that provided a good indicator of battery life and sensor activity. This feature enabled better efficiency in determining when sensors or batteries needed to be replaced rather than waiting until the recovery of the instrument. As possibly the first major sampling effort at the AHL utilizing multiple sensors, over several years, it was a major feat that resulted in several valuable datasets that were made publicly available.

1.5. Acknowledgements

We thank all past and current Martz lab members who have contributed to deployments, recoveries, and bottle sampling. We also thank the CAF for the use of their boat and facilities.

1.6. Tables and Figures

Table 1.1. Lists the locations and depth of mooring sensor deployments, periods deployed, and measurements made.

Location Description	Measurements	Sensor	Start date	Days deployed
Outer Lagoon				
1 m below surface	pCO_2, DIC, pH, S, T	BoL	11/1/2015	1,192
6-7 m below surface	S, pH, DO, T, P	SeapHOx1	8/20/2018	73
10 m below surface	S, pH, DO, T, P	SeapHOx2	11/2/2018	69
surface	DO, T	miniDOT-1	8/20/2018	288
5-6 m below surface	S, pH, DO, T, P	SeapHOx2	1/22/2020	146
Middle Lagoon				
6-7 m below surface	S, pH, DO, T, P	SeapHOx	9/21/2018	112
surface	DO, T	miniDOT-2	9/21/2018	112
surface	S, T	CTD	9/21/2018	112
Carlsbad Offshore				
6-7 m below surface	S, pH, DO, T, P	SeapHOx	8/17/2018	285

Table 1.2. Provides CO_2 instrument bottle sample information and lab analyses results for DIC and pH along with the corrections applied.

		CO_2 Instrument bottle sample data					
Date	**Action taken**	**Temp**	**Salinity**	**DIC**	**pCO2**	**pH**	**TA**
1/18/2018	CAF bottle Sample 1 collected	17.99	33.4	2063.4	595.03	7.8859	2218
1/25/2018	CAF bottle Sample 2 collected	15.35	33.7	2069.2	640.1	7.8524	2197
2/13/2018	CAF bottle Sample 3 collected	17.17	33.66	2038.5	510.2	7.9444	2214
2/22/2018	CAF bottle Sample 4 collected						
4/17/2018	pH offset of -0.18 applied to CAF UDA						
10/15/2019	pH offset of -0.18 applied to Jan-April durafet pH data		**Lab Results**				
10/28/2019	Bottle samples 1-3 analyzed w/ CRM		**Raw DIC results**			**Spec pH results**	
		Sample #	**Avg DIC**	**Corrected DIC**	**Temp**	**Avg pH**	**Temp**	**ΔDIC offsets**
CRM 183	(DIC= 2040.25, TA= 2230.52, S= 33.42, pH= 7.946)	CRM 183	2096.8	2040.25	23.7	7.926	19.939	
		1	2138.26	2080.592	22.18	7.849	19.943	17.2
		2	2149.98	2091.996	22.15	7.845	19.943	22.8
		3	2144.54	2086.702	22.17	7.821	19.947	48.2

Figure 1.1. Map of AHL including locations of the sensors (red X), features of the lagoon and sites of interest, which include the Carlsbad Aquafarm (CAF), Encina Power Station (EPS), Desalination Plant (DP), Strawberry fields (SF), Recreational water sports and activities (RS), and the Hubbs-SeaWorld Fish Hatchery (HFH). Image from Google Earth.

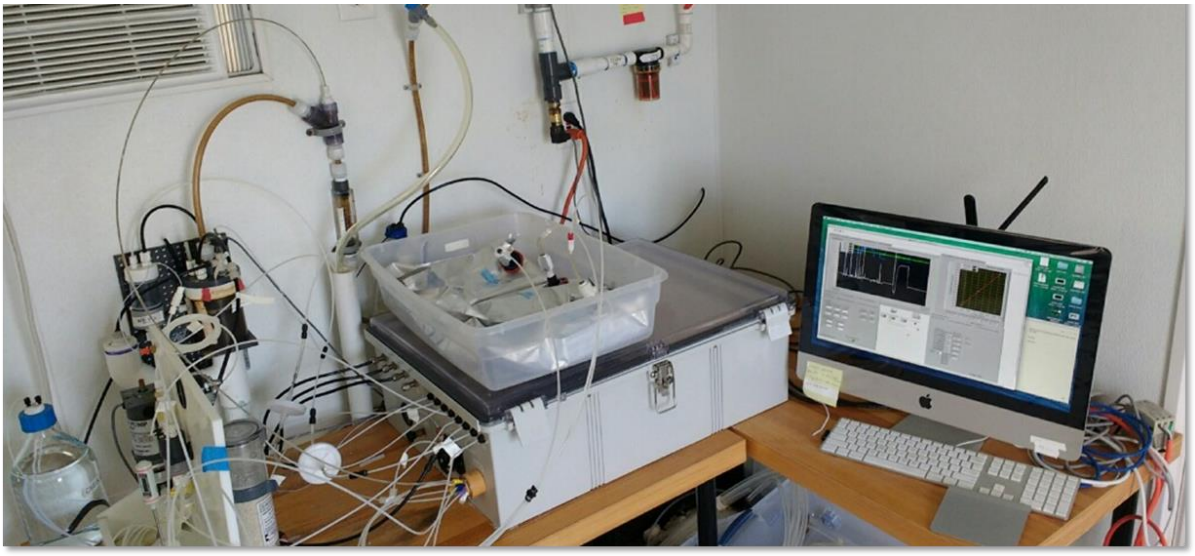

Figure 1.2. Image of CO_2 instrument setup at the CAF.

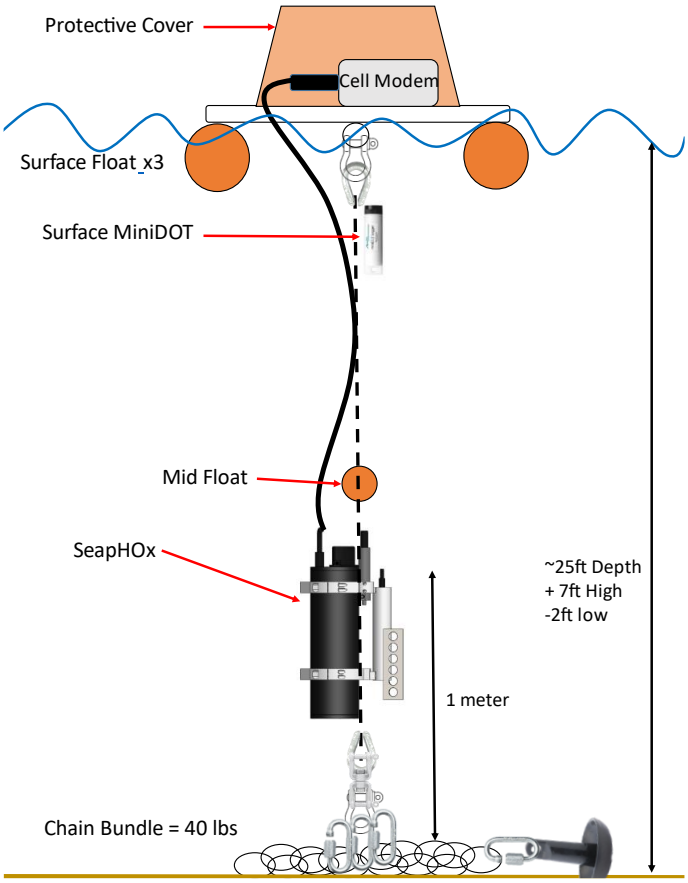

Figure 1.3. Schematic of in situ mooring design including sensors, hardware, and cell modem used in real-time data acquisition

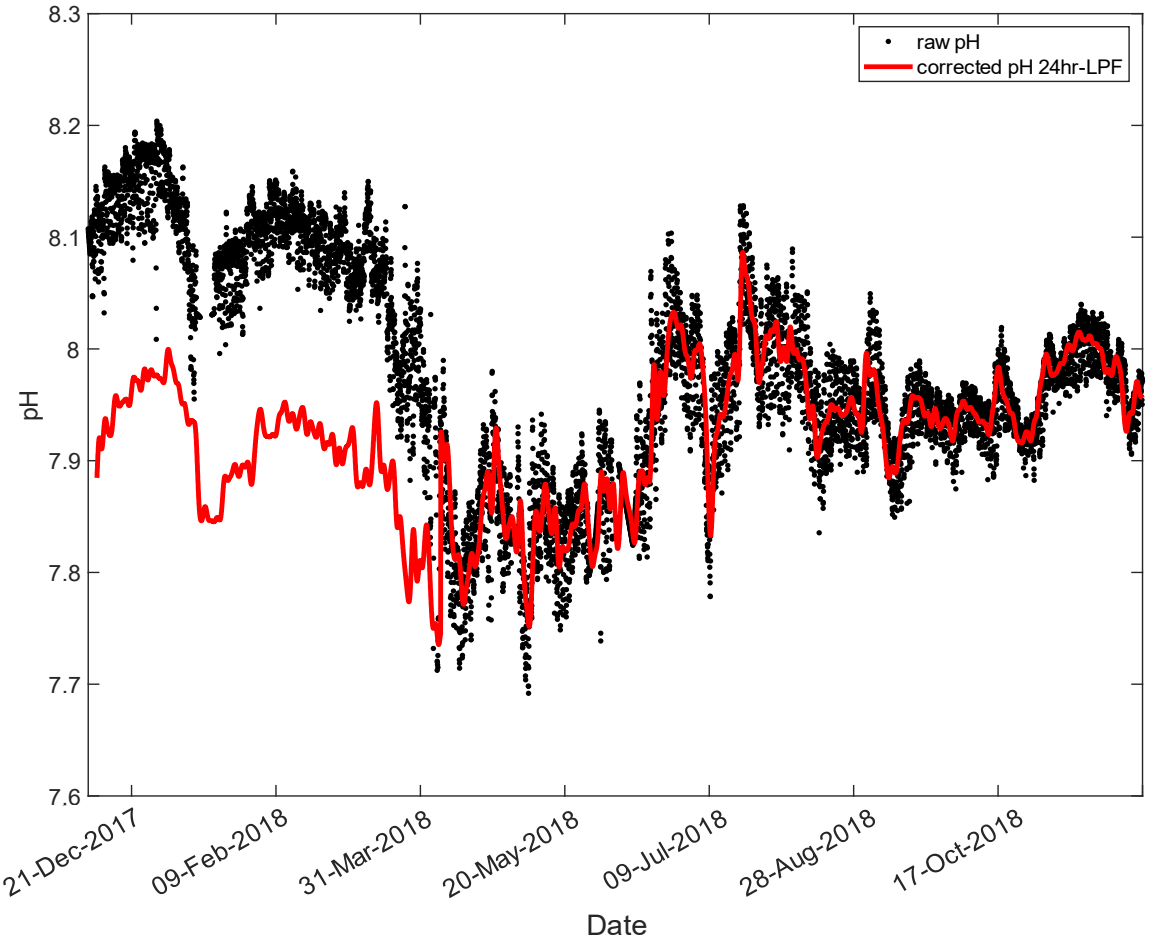

Figure 1.4. Shows the pH data measured from the CO_2 instrument. Raw data is shown in black, and data corrected based on a bottle sample analysis is shown in red.

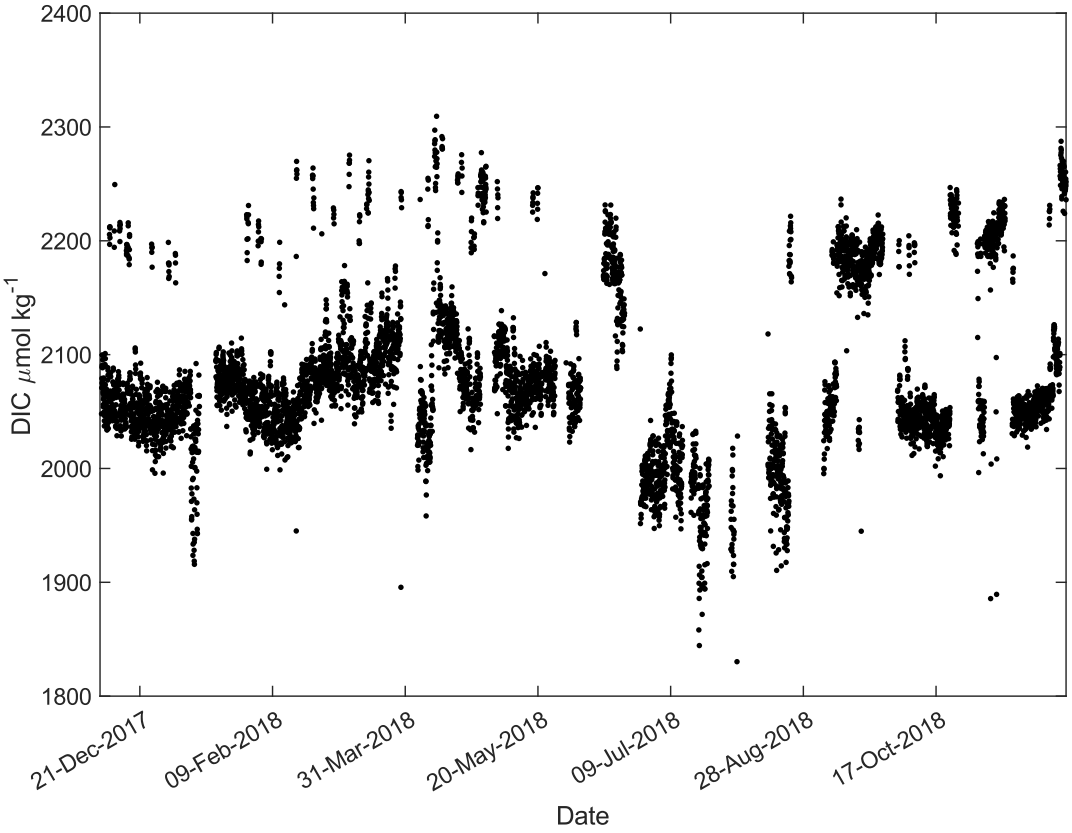

Figure 1.5. Figure of DIC measured on the CO_2 instrument prior to processing with monthly averaged calibrations and bottle sample offset.

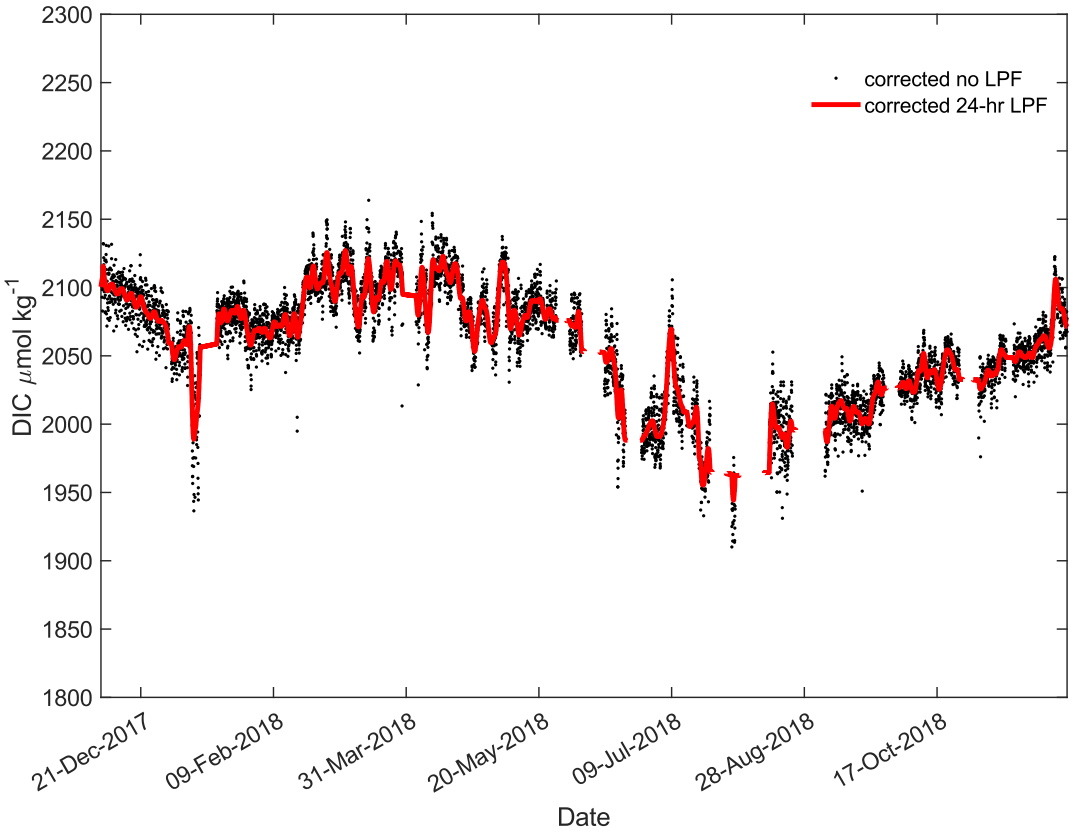

Figure 1.6. Figure of corrected DIC with 24-hr LPF in red and no filter in black. Monthly averaged calibration data and the bottle sample offset has been applied.

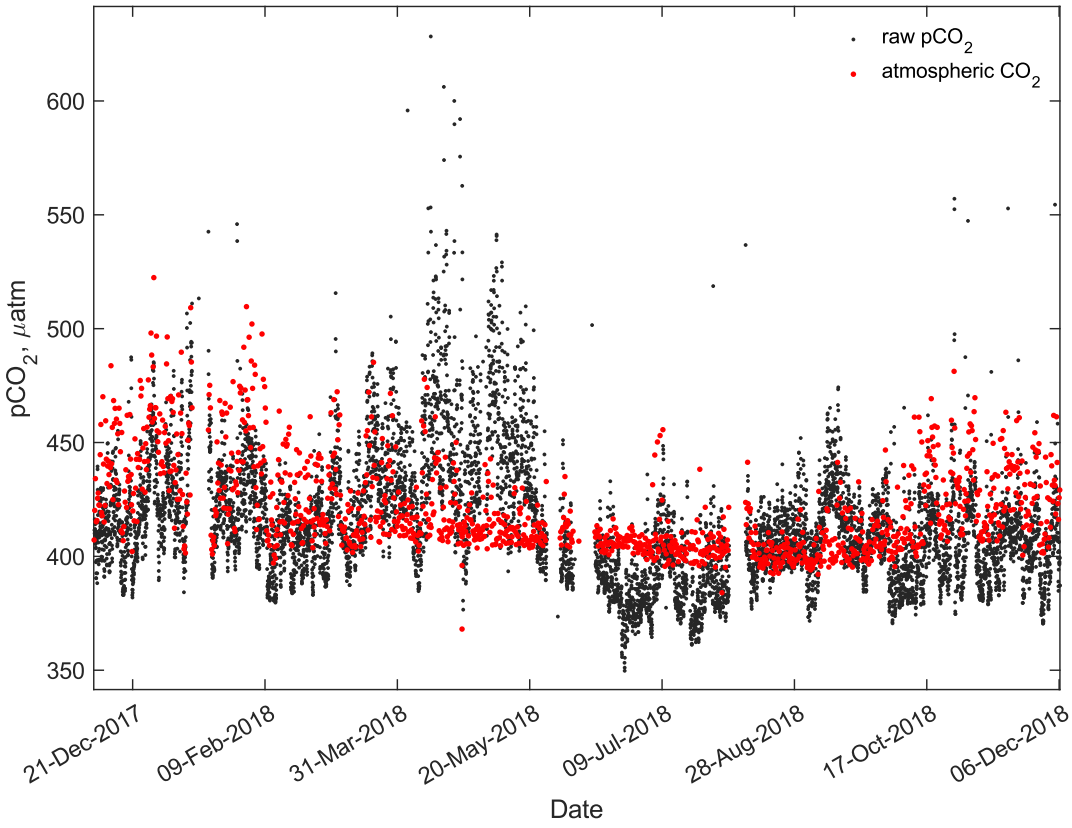

Figure 1.7. Plot of measured pCO_2 and atmospheric CO_2 from the CO_2 instrument.

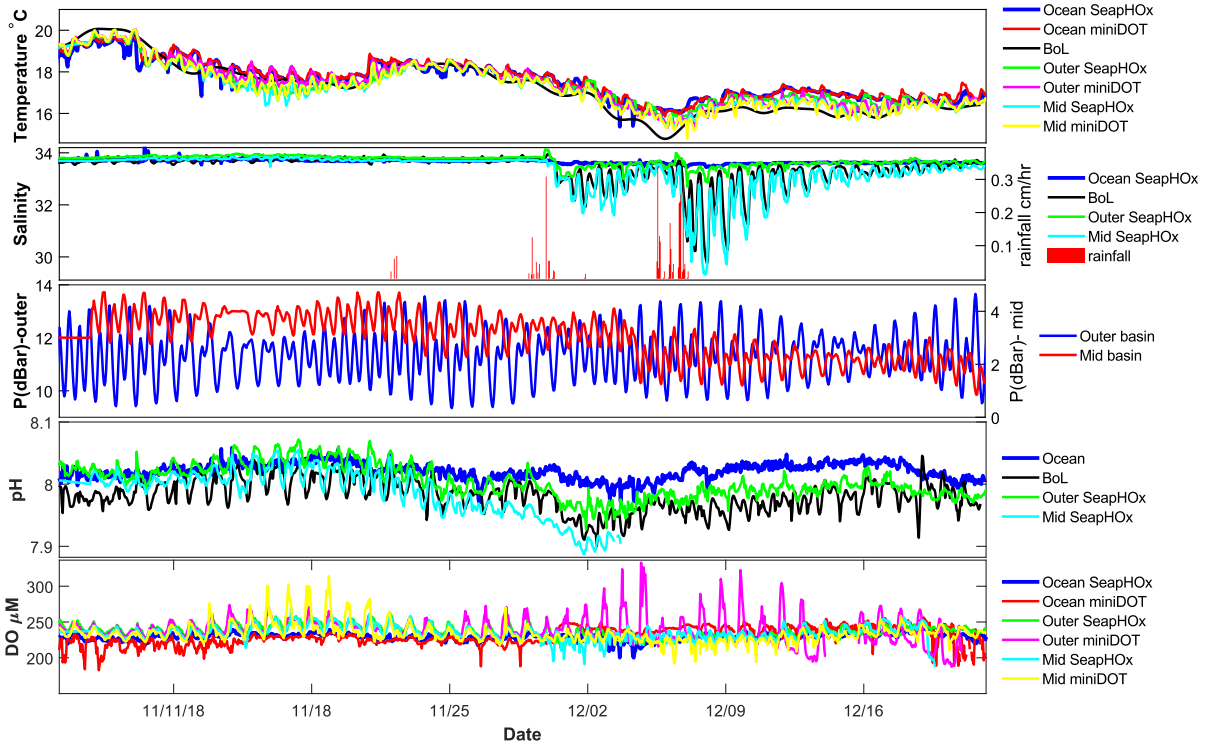

Figure 1.8. Example of 2-month period of QC'd data collected from all the in situ mooring sensors at the AHL.

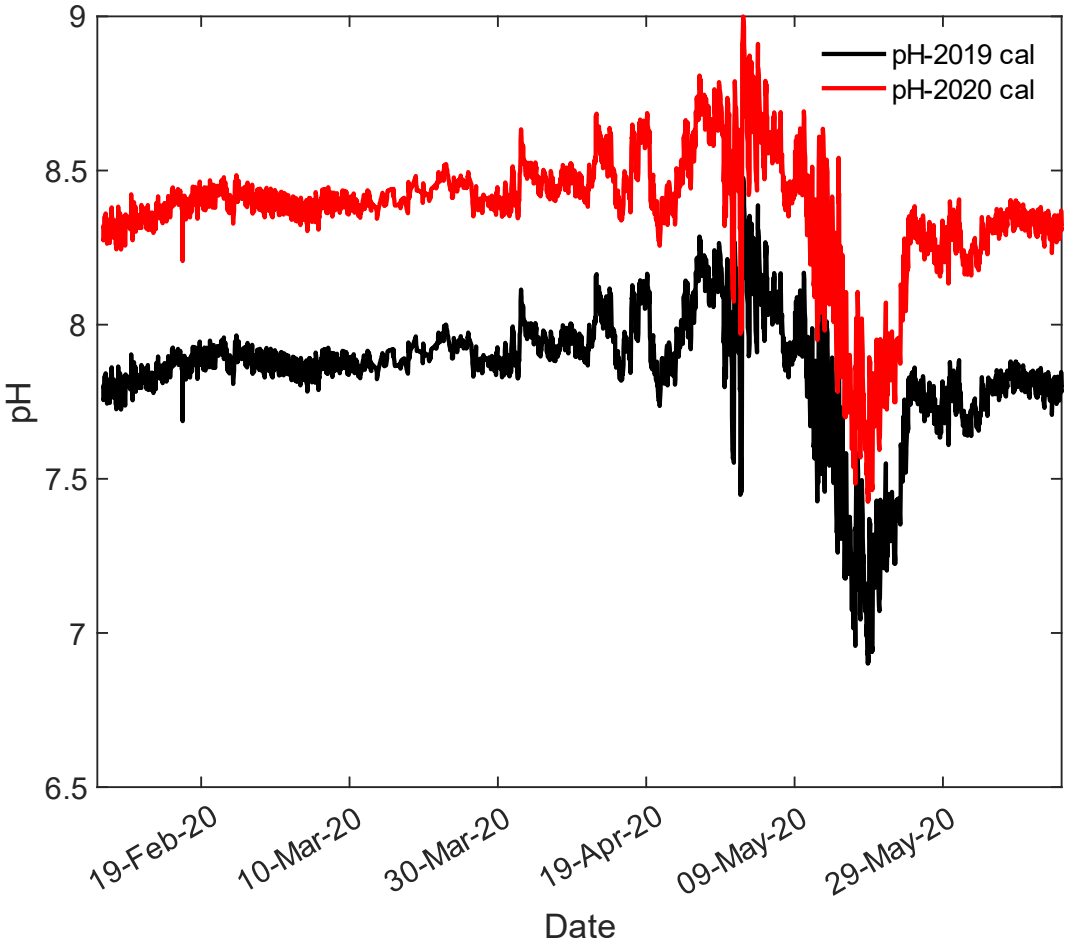

Figure 1.9. Figure showing the 2020 pH measured on the outer basin SeapHOx. Black shows the pH calculated using the 2019 calibration point (used in Ch.3 analyses) and the red showing the 2019 calibration point calculation.

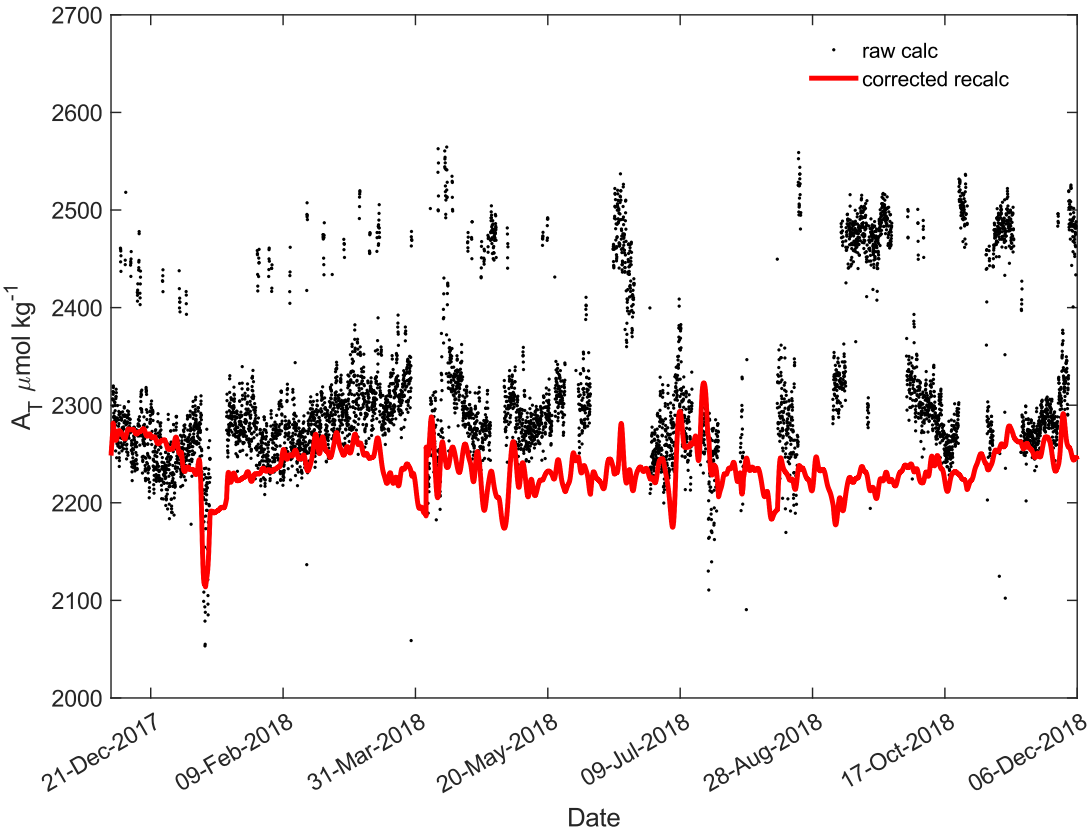

Figure 1.10. Figure showing initial derived A_T (black) based on CO_2 instrument measurements and the recalculated A_T (red) after data QC and processing.

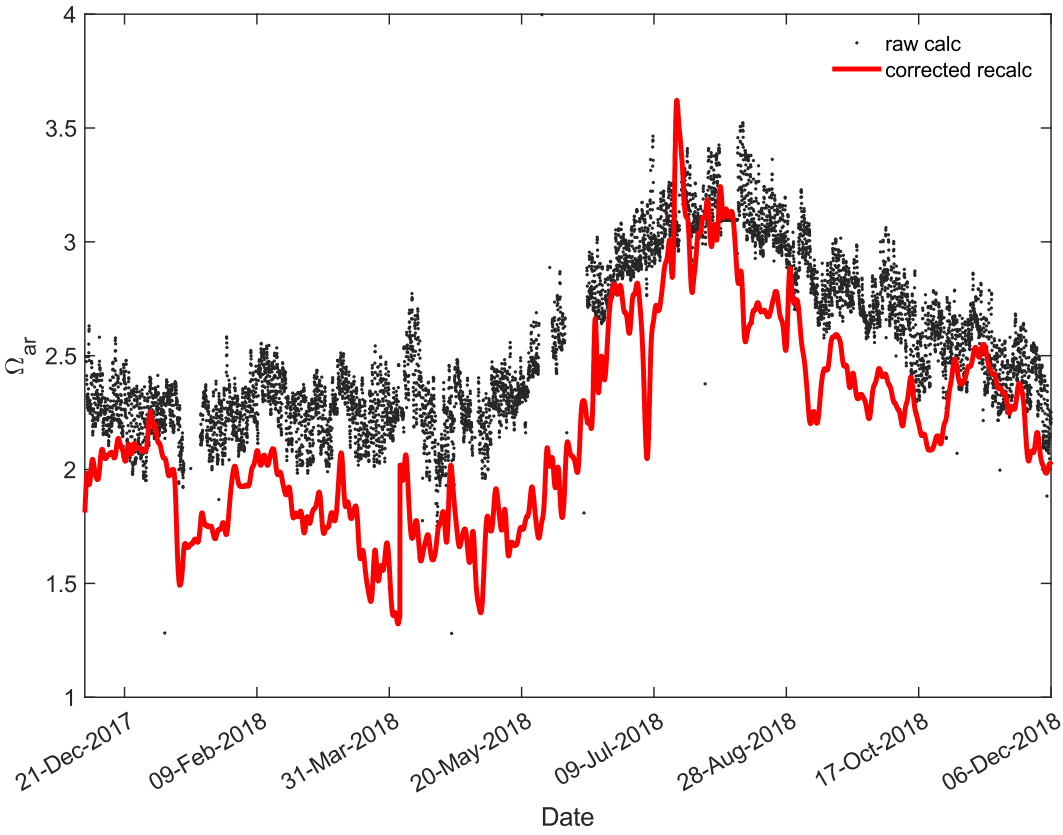

Figure 1.11. Figure showing initial derived Ω_{Ar} (black) based on the CO_2 instruments raw measurements and the recalculated Ω_{Ar} (red) after data QC and processing.

1.7. References

Bandstra L, Hales B, Takahashi T. 2006. High-frequency measurements of total CO2: Method development and first oceanographic observations. *Marine Chemistry* **100**(1–2): 24–38. doi: 10.1016/j.marchem.2005.10.009

Bresnahan PJ, Martz TR, Takeshita Y, Johnson KS, LaShomb M. 2014. Best practices for autonomous measurement of seawater pH with the Honeywell Durafet. *Methods in Oceanography* **9**(October): 44–60. doi: 10.1016/j.mio.2014.08.003

Bresnahan PJ, Wirth T, Martz T, Shipley K, Rowley V, Anderson C, Grimm T. 2020. Equipping smart coasts with marine water quality IoT sensors. *Results in Engineering* **5**. Elsevier Ltd. doi: 10.1016/j.rineng.2019.100087

Dickson AG. 2010. Standards for ocean measurements. *Oceanography* **23**(3): 34–47. doi: 10.5670/oceanog.2010.22

Dickson AG, Millero FJ. 1987. A comparison of the equilibrium constants for the dissociation of carbonic acid in seawater media. *Deep Sea Research Part A, Oceanographic Research Papers* **34**(10): 1733–1743. Elsevier. doi: 10.1016/0198-0149(87)90021-5

Fairchild W, Hales B. 2021. High-Resolution Carbonate System Dynamics of Netarts Bay, OR From 2014 to 2019. *Frontiers in Marine Science* **7**. Frontiers Media S.A. doi: 10.3389/fmars.2020.590236

Hales B, Chipman D, Takahashi T. 2004. High-frequency measurement of partial pressure and total concentration of carbon dioxide in seawater using microporous hydrophobic membrane contactors. *Limnology and Oceanography: Methods* **2**(11): 356–364. doi: 10.4319/lom.2004.2.356

van Heuven S, Pierrot D, Rae JWB, Lewis E, Wallace DWR. 2011. MATLAB program developed for CO2 system calculations. Carbon dioxide information analysis center, Oak Ridge National Laboratory, U.S. Department of Energy, Oak Ridge, Tennessee.

Pierrot D, Neill C, Sullivan K, Castle R, Wanninkhof R, Lüger H, Johannessen T, Olsen A, Feely RA, Cosca CE. 2009. Recommendations for autonomous underway pCO2measuring systems and data-reduction routines. *Deep-Sea Research Part II: Topical Studies in Oceanography* **56**(8–10): 512–522. doi: 10.1016/j.dsr2.2008.12.005

Chapter 2. Physical and Biological Controls on the Seasonal CO_2 Cycle in the and Agua Hedionda Lagoon, Carlsbad, CA

2.1. Abstract

The Agua Hedionda Lagoon (AHL), a tidal estuary located on the southern California coast, supports a diverse ecosystem while serving numerous recreation activities, a marine fish hatchery, a shellfish hatchery (Carlsbad Aquafarm, CAF), and the largest desalination plant in the western hemisphere. In this work, a one-year time series of carbon dioxide (CO_2) data is used to establish baseline and seasonal average inorganic carbon conditions in the AHL. Based on a mass balance model of the lagoon, we propose that the outer basin of AHL is a source of inorganic carbon to the adjacent ocean, through advective export, at a rate of 2.4×10^6 mol C yr^{-1}, and a source of CO_2 to the atmosphere of 0.17×10^6 mol C yr^{-1} (0.9 mol C m^{-2} yr^{-1}), implying a net heterotrophic system on the order of 2.5×10^6 mol C yr^{-1} (12 mol C m^{-2} yr^{-1}). Although heterotrophic on average, the lagoon may shift into a net autotrophic state during the late summer. The combination of drivers including advection, ecosystem metabolism, and temperature act to balance a seasonal cycle in properties (pH, pCO_2 and $CaCO_3$ saturation state) of importance to both natural and human-made components of this complex environment.

2.2. Introduction

Semi-enclosed coastal systems (e.g. estuaries, lagoons, intertidal zones, wetlands) are important to a wide number of natural processes in addition to societal and commercial uses (Ramesh et al., 2015). In many cases, the proximity to civilization makes the ecosystems operating within these coastal systems highly influenced by anthropogenic effects such as eutrophication from nutrient loading and habitat loss due to land use change (Bauer et al., 2013; Howarth et al., 2011; Windham-Myers et al., 2018). In addition to these long-recognized issues, climate change (warming, acidification, deoxygenation) in the coastal ocean (Hauri et al., 2009; Gruber et al., 2012; Kessouri et al., 2021) and shallow coastal systems (Feely et al., 2010; Waldbusser et al., 2014; Cai et al., 2021) is now a well-established area of research.

Over the past decade, the US Pacific Northwest has been recognized as a bellwether in the study of coastal acidification (Hales et al., 2005; Feely et al., 2008; Evans et al., 2011). Of particular note, an upwelling event in 2009 led to unambiguous demonstration that oyster larval mortality was impacted by abnormally low saturation state of the intake water at a commercial shellfish hatchery (Barton et al., 2012). This finding, along with other growing evidence of organismal sensitivity to increasing dissolved CO_2 and acidification (Doney et al., 2020) has led to the widespread recognition of the need to better observe the coastal ocean carbonate system globally. In particular, there is a need to understand the carbonate system within semi-enclosed coastal lagoons and estuaries and their net fluxes to the coastal ocean and to the atmosphere (e.g., Cai, 2011; Wang et al., 2016). Existing studies are limited and those that exist have a wide range of flux estimates and thus are not well constrained (Cai, 2011; Paulsen et al., 2018).

In parallel with OA research, coastal ocean observing systems are steadily growing in breadth and autonomy (Tilbrook et al., 2019; Barth et al., 2019); and coastal management and stewardship programs such as the National Estuarine Research Reserves (NERR) increasingly rely on observing system data to develop their strategies (NOAA, 2017). Among these is an initiative by NOAA to partner with a selection of shellfish growers in an effort to better understand the baseline conditions of the growers' local lagoons and estuarine systems (Barton et al., 2015; Hales et al., 2017). A central piece of equipment that has been deployed in this effort is a continuous flow multiparameter instrument developed at Oregon State University (OSU) (Hales et al., 2004; Bandstra et al., 2006; Fairchild and Hales, 2021). This system characterizes the full suite of CO_2 chemistry parameters (partial pressure of CO_2 - pCO_2, total dissolved inorganic carbon - DIC, pH, total alkalinity - A_T, and $CaCO_3$ saturation state - Ω) either directly or by derivation using well-established thermodynamic relationships.

The Agua Hedionda Lagoon (AHL) is one of six tidal estuaries located along the northern San Diego County coast (Beller et al., 2014), although it is characterized as a low-inflow estuary, an estuarine type found worldwide. Low-inflow estuaries (LIEs) are estuaries where the total freshwater inflow is

small, episodic, and/or seasonal. LIEs are found throughout Southern California (e.g., Southern California Wetlands Recovery Project, 2018; Doughty et al., 2018), but also worldwide in regions with steep watersheds and/or Mediterranean climates (Largier et al. 1997; Largier et al. 2010).

In this work we analyze and interpret a full year of CO_2 system observations at the AHL, collected using the OSU continuous flow system. Salinity data are first used in a simple mixing model to establish a robust estimate of the mean flushing time of the lagoon. Flushing time is then used in a mass balance of the outer basin to estimate the rate of advection and net ecosystem metabolism (NEM). In addition to presenting average seasonality in all CO_2 parameters mentioned above, the results of the mass balance are used to perform a decomposition of pH, pCO_2 and Ω. We found the decomposition to be an instructive step in visualizing how the effect of each driver (temperature, advection, NEM, gas exchange) evolves throughout the year to determine the composite average and seasonal cycle of CO_2 in the AHL. Given the need to understand semi-enclosed coastal carbonate chemistry, this analysis contributes to the growing body of knowledge on estuarine carbonate chemistry, but also adds specifically to understanding these dynamics within LIEs.

2.3. Materials and Methods

2.3.1. Study Site

The AHL, Carlsbad, CA, comprises three interconnected lagoons, commonly referred to as the outer (connected to the ocean), middle, and inner basins. The original wetland was converted into the present lagoon structure in 1954 by the Encina Power Station (EPS) and is maintained in its present form by semi-annual dredging. The AHL consists of >75% open water with the remainder being marsh and mudflats (Beller et al., 2014). Water depths range from very shallow (< 1 m) up to approximately 14 m in certain areas, with an average depth of 8 m (Elwany et al., 2005). The ocean, connected by an inlet on the western side of the outer basin, dominates physical forcing in all three basins, with tidal lags of up to 4 hours at the head of the lagoon where Agua Hedionda Creek enters (Jenkins and Wasyl, 2006). The inner

basin receives episodic freshwater input from Agua Hedionda Creek, predominantly in winter and spring during rain events. During the rest of the year the creek is dry, and the lagoon is purely tidal.

Located in an urbanized area, the AHL is a highly utilized and popular destination for the Carlsbad community and tourists; and provides a thriving ecosystem for diverse species of plants and animals. The two primary industrial features include the EPS and the Carlsbad Desalination Plant, both of which rely on water intake from the outer basin for once-through cooling of the power plant boilers and as desalination source water. The EPS was decommissioned Jan. 2019 but may have operated intermittently during the course of this study, drawing water from the outer lagoon. The desalination plant diverts from the EPS intake and its byproduct (brine) outflow is released through the EPS discharge channel into a small basin connected directly to the ocean, and adjacent to the outer basin (Figure 2.1). Total intake volume of the EPS and desalination facilities is variable and at peak periods may represent a significant fraction of the daily tidal prism (Elwany et al., 2005; City of Carlsbad, 2005). Other features of the AHL include agriculture (primarily strawberry fields bordering the inner basin), the Hubbs Marine Fish Hatchery, and the Carlsbad Aquafarm (CAF) - a sustainable mussel and oyster farm, which operates in the outer basin. Both the fish hatchery and aquafarm (which grows calcifying organisms) rely on adequate lagoon flushing by the ambient ocean in order to maintain oxygen, pH and calcium carbonate saturation state (Ω) above thresholds critical to growth. The CAF was one of the sites along the Pacific West Coast provided with the automated instrument (described above) through NOAA's Integrated Ocean Observing System (IOOS) program for real-time monitoring of the CO_2 system by local stakeholders and shellfish growers. In collaboration with the IOOS regional associations (NANOOS, AOOS, CeNCOOS, and SCCOOS), the common goal of the instrument was to provide real-time information on the CO_2 content of the waters along the coastal ocean and its impact on carbonate organisms at the aquafarm intake.

2.3.2. Sampling

Continuous pCO_2 and DIC measurements were carried out using the automated instrument supplied by OSU. The instrument's water intake line was positioned near the CAF facility docks (Figure 2.1) approximately 1 m below the surface. The lagoon water was pumped through about 25 m of PVC

piping to the instrument, which was housed in a small lab at the CAF. The incoming water is first filtered through a nylon screen T-strainer to remove large debris from the water, which then passes through a line containing a Honeywell 4905 conductivity probe and a Honeywell Durafet sensor to obtain salinity, temperature, and pH measurements. Water then enters an enclosed headspace showerhead equilibrator, which contains a bubbling tube to facilitate equilibration of the CO_2 between the headspace and water (Fairchild and Hales, 2021, Hales et al., 2004). The CO_2 gas is circulated to a LI-820A non-dispersive infrared (NDIR) detector to measure the mole fraction of the CO_2 (xCO_2) gas. At hourly intervals, the instrument switches to DIC mode and the sample water flows through a separate DIC sample line where it passes through a stainless-steel tangential flow filter to remove micron size particles from the sample water. The filtered sample water is then acidified with 10% hydrochloric acid and is passed through a mixing coil. CO_2 is extracted in a hydrophobic gas permeable membrane contactor (Liqui-Cel, G543), where the evolved CO_2 gas stream is dried and directed to the NDIR detector to determine the xCO_2 (Bandstra et al., 2006). Additional CO_2 system calculations for seawater A_T and Ω for aragonite and calcite are performed within the LabView program which operates through the instrument's computer. The sample frequency and data storage were specified at 15 sec intervals for in situ and pCO_2 data, and hourly intervals for DIC and calculated parameters. This study reflects data collected during a 365 day period of minimal instrument interruption from Dec 6, 2017 to Dec 5, 2018.

2.3.3. Instrument Calibration

The instrument's automated calibration sequence using CO_2 gas and DIC liquid standards occurs every 6 hours. The set of gas standards were purchased from Scott-Marin at concentrations of 200, 800, and 1500 µatm stored in gas cylinders. The set of DIC liquid standards contained a solution mixture of ultrapure water (>18 MΩ resistivity), $NaHCO_3$, oven dried Na_2CO_3 and 0.1 M HCl. The standards were gravimetrically prepared at the Scripps Institution of Oceanography (SIO) in concentrations of 1900, 2100, and 2300 µmol kg^{-1} every 12-14 days and stored in custom made gas impermeable Mylar bags (IMPAK P75C0919). As further described in (Fairchild and Hales, 2021), during a gas calibration sequence, a linear regression is performed in real-time to verify the accuracy of the NDIR and apply a

correction to the respective pCO_2 data to account for any offsets in the raw xCO_2 measurements. It is also during the gas standard sequence that an atmospheric CO_2 measurement is made from a separate line that extends outside (Figure 2.2A). The liquid standard sequence occurs directly after the gas standards and also produces a linear regression in real-time. While the gas standard regressions typically achieved high linearity with $R^2 = 0.999$ or better, the liquid standards experienced $R^2 \leq 0.999$. In cases where linearity was lower in the liquid standard regression, it was identified that when the liquid standard bags became too low, air bubbles were able to enter the line. To address this issue, a monthly averaged liquid standard and gas standard calibration was applied to the raw xCO_2 detector data in post processing to achieve corrected DIC data.

Bottle samples were collected monthly from the main sample water line of the instrument into 250 mL borosilicate bottles (3x rinsed and filled) for laboratory analyses on the benchtop density meter (Mettler-Toledo DM45). The recorded instrument salinity and density meter salinity were compared and any difference between the two was applied via remote desktop access where the adjusted data were then automatically stored in an output file. Salinity corrections were only applied if the check sample salinity was off by more than ±0.05. Bottle samples were also collected and poisoned with mercuric chloride for DIC and pH validation. During this study, a total of 4 bottle samples were collected and analyzed on the benchtop spectrophotometric pH system and the DIC analyzer which were compared against certified reference materials (CRMs). A pH offset of -0.18 was applied based on an April 2018 bottle sample comparison. Samples analyzed at the end of 2018 determined an insignificant drift in pH (< 0.005) and no additional pH offsets were applied. DIC laboratory analysis of three bottle samples did reveal an offset in the instrument DIC of 29 ± 16 µmol kg^{-1} (n = 3), which was added to the final DIC dataset to account for the difference. The initial instrument pCO_2 measurements were determined to be compromised due to an air leak and the final pCO_2 dataset analyzed in this study was derived in CO2SYS from QC'd DIC and pH data. The additional calculated parameters including A_T and Ω_{arag} were recalculated in CO2SYS using corrected pH and corrected DIC.

2.3.4. Data Processing

Data from the flow-through instrument pCO_2, pH, salinity, and temperature were interpolated to hourly (the frequency of DIC data) and, combined with other publicly-available data including wind speed and rain, both obtained from the NOAA climate database for the weather station at McClellan-Palomar airport in Carlsbad, CA approximately four miles from the AHL (https://www.ncdc.noaa.gov/cdo-web/datasets/LCD/stations/WBAN:03177/detail). All data were interpolated onto a common 1-hour time stamp.

All data were processed using a 30-d or 24-hr low pass filter (LPF, MATLAB *filtfilt* zero phase filter) to isolate the seasonal cycle in both temperature and DIC (Figure 2.2). The high frequency time series undoubtedly contains additional information, yet we chose to focus this analysis on the LPF data because: 1) mixing in tidal systems becomes increasingly difficult to parameterize as the model approaches tidal timescales; and data at these timescales (e.g. flow rates, bathymetry, etc.) were not available, and 2) some of the data were determined to be compromised in terms of noise and the LPF is capable of eliminating this. In regard to the latter, instrument salinity exhibited pronounced noise during the first 4-months of the time series due to an electrical ground fault and step changes that may have been due to fouling. The LPF averages over these errors but consequently removes real signals associated with rain events. Without high quality salinity data, it would be impossible to constrain a high-resolution hydrodynamic model of this system. In addition to salinity, diel temperature amplitude measured by the instrument was unduly high. The source of this problem was a delivery line from the lagoon to the instrument, extended across the roof of a building where the line underwent excessive heating and cooling due to its contact with the atmosphere. Based on in situ measurements from SeapHOx sensors in the lagoon (Shipley, 2022) we were able to determine that the LPF instrument temperature agrees with average lagoon temperature, making the LPF temperature a viable approximation of the lagoon temperature. Correcting the hourly instrument data to reflect in situ temperature is possible, given a continuous measurement of in situ temperature. A validated in situ temperature was not available

throughout the full span of the 365 d time series presented here, and though beyond the scope of this analysis, such data, if available, may provide additional information for further analysis of this dataset.

2.3.5. Mixing Model

To model the annual CO_2 cycle, based on the LPF time series, it is necessary to first approximate the average rate of exchange between the lagoon and the ocean. In order to accomplish this, we focus on a one-month period during Dec 2018 where two significant rain events occurred while the salinity measurement was functional and accurate. Rain events also took place during the previous winter of 2017/2018 (Figure 2.2C), but, as noted above, this period also coincided with noisy salinity data that would not facilitate a mixing model.

During Dec 2018, mixing is approximated using the tidal prism equation (Monsen et al., 2002)

$$T_f = \frac{V_{outer} \times T_{period}}{(1-R)V_{prism}} \quad (2.1)$$

Where T_f is flushing time, V_{outer} is the average volume of the outer lagoon, T_{period} is the tidal period (set to 24hr here as this is the largest component even though tides are mixed semidiurnal), V_{prism} is the tidal prism of the outer lagoon and R is the return flow factor that accounts for several processes, some poorly constrained, including inefficient mixing and intake volumes of the EPS and desalination plant. V_{prism} is calculated as the mean daily tidal range (0.87 m) multiplied by the mean area of the outer lagoon (2×10^5 m^2). The return flow factor is the average of flood and ebb return factors: $R = (R_F + R_E)/2$, that are determined using a 4-box model including three boxes representing the lagoon and one for the ocean (Figure 2.3). In the 4-box model, Equation 2a and 2b represent the outer lagoon (superscript 1) and are used to calculate mixing between it, the adjacent ocean (superscript 0) and the middle lagoon (superscript 2) during the flood (Equation 2.2a) and ebb tide (Equation 2.2b).

$$S_t^1 = \frac{S_{t-1}^1 V_{t-1}^1 + dV_t^1(1-R_F)S_{t-1}^0 + dV_t^1 R_F S_{t-1}^1 - dV_t^2 S_{t-1}^1}{V_{t-1}^1 + dV_t^1 - dV_t^1 + V_r} \quad (2.2a)$$

$$S_t^1 = \frac{S_{t-1}^1 V_{t-1}^1 - dV_t^1 S_{t-1}^1 + dV_t^2(1-R_E)S_{t-1}^2 + dV_t^2 R_E S_{t-1}^1}{V_{t-1}^1 - dV_t^1 + dV_t^2 + V_r} \quad (2.2b)$$

Similar equations (not shown) are used for the middle and inner lagoons. For Equation 2.2a,b, superscripts represent box number, t is time step and dV is calculated from change in tide height multiplied by the area of the respective box. Return flow factors are only considered for the outer lagoon (i.e. for the middle and inner lagoon boxes $R_F = R_E = 0$). We found that tuning additional return flow factors for boxes 2 and 3 did not provide improvement and furthermore, the dataset being limited to the outer lagoon provides little constraint on adjacent lagoon return flow parameterizations.

Though it is not a gauged stream, we believe, based on empirical observations (e.g. hypersaline summer conditions in the inner basin, lack of visible creek flow during summertime visits) that freshwater input from the Agua Hedionda Creek is exclusively associated with rain events and therefore, V_r (runoff) is computed from hourly rainfall data with freshwater input otherwise set to zero. Rainfall is multiplied by catchment area and given a delay time of 1 day (established by matching modeled results to the phase of the freshwater spikes in observed salinity) to allow for runoff. Since the effective catchment area may depend on factors such as storm patchiness and soil permeability, V_r is treated as a tunable parameter (through CF below) along with R_F and R_E. The total watershed of the Agua Hedionda Creek is 76 km^2, representing approximately 80× the area of the Agua Hedionda Lagoon and ~14% of the greater Carlsbad Hydrologic Unit which is divided among four separate lagoons (City of Carlsbad, 2021). The effective catchment area was allowed to vary as a multiple of the area of the AHL using,

$$A_{catchment} = CF(A_{outer} + A_{middle} + A_{inner}) \tag{2.3}$$

where CF is the catchment factor, which must represent less than the 80× watershed/lagoon area.

Although the simple 4-box mixing model based on Equation 2.2 and presented in Figure 2.4 does not adequately capture tidal range in salinity, the underlying mixing trend representing the flushing time is the most important result for operating a seasonal model of the one-yr time series of LPF data. In tuning the mixing model, we used a 24hr LPF of salinity observed in the outer lagoon during a 1-month period where several rain events occurred (Nov 24 - Dec 24); extending just beyond the 365 d DIC time

series. During this period, the CO_2 instrument experienced a failure, but the salinity sensor continued to operate, capturing valuable information on the physical mixing of the lagoon. The three adjustable model parameters: CF, R_F, and R_E were tuned using the MATLAB function "fmincon" (interior-point method), resulting in values of CF = 21, R_F= 0.0, and R_E = 0.95 with a resulting RMSE of 0.14 in salinity (Figure 2.4). The multiplier for runoff (CF) represents an area 21× greater than the lagoon itself, which seems quite reasonable given a watershed area of 80×. The flood return flow factor of 0 indicates that the outgoing plume from the lagoon is swept away from the mouth by the open ocean before the tide comes back in. This result also seems appropriate as the inlet of the outer lagoon is directly connected to the ocean where an alongshore flow often persists (Nam and Send, 2011). The very high ebb tide return flow factor of 0.95 is not surprising, as the much smaller middle basin receives all of the outer basin flood tide (Figure 2.1). The difference between a zero flood return flow factor, and non-zero ebb factor is also consistent with a well-mixed box model potentially being more representative during the flood tide, consistent with flood tides typically exhibiting more vertical mixing and less stratification in many estuarine systems (e.g., Simpson et al., 1990; Geyer and MacCready, 2014)

Based on the results of the 30-d 4-box mixing model, an average R = 0.48 was used in Equation 1.1 to compute a mean flushing time of 7.3 d. The flushing time determined in this way is nearly twice what one would estimate based purely on the tidal prism. For example, the average 24-hr tidal range throughout the time series is 1.6 m. Combining this value with the area of the outer basin and the average volume of the outer basin (Table 2.1) gives a flushing time of only 3.8 d. Similar approaches based strictly on tidal prism, but accounting for temporal variability in tidal stage, estimate flushing times across the different boxes ranging from 1-5 days but with roughly the same average of ~3 d (Elwany et al., 2005). As discussed by Monsen et al. (2002) it is not uncommon for flushing time approximated by basin geometry to differ from that derived from actual measurements of bulk properties such as salinity (or other closely related concepts such as residence time and age) by a factor of two or more. Moreover, recent studies utilizing high resolution numerical models have shown that flushing time estimates can vary dramatically depending upon the method (Lemagie and Lerczak, 2015) and that simple geometric

flushing time estimates typically underpredict true residence time due to incomplete vertical mixing and return flows (MacCready et al., 2020). Furthermore, evidence suggests that flushing times determined from bulk properties during rain events (as done in Figure 2.3) may underestimate average flushing time (Alber and Sheldon, 1999).

Exchange flow calculations from velocity measurements conducted during Spring 2016 (averaging 0.1 m s^{-1}), combined with the dimensions of the full lagoon (Table 2.1) and an approximate cross sectional area of 36 - 54 m^2 at the mouth, suggest T_f in the range of 6.3 - 9.5 d. Thus, flushing time determined from salinity observations during a rain event in 2018 (Figure 2.3) is in excellent agreement with that determined from exchange flow during a longer period, absent rain. Combining the two observation-based estimates, we selected the range T_f = 6 - 8 d for use in the biogeochemical model, with 7d as the central vale used to report averages. In summary, transport could be characterized in a number of different ways for this particular time series, but, based on observations of salinity and velocity, we suspect that our estimate represents a more accurate value than that obtained based on geometry alone (Lemagie and Lerczak, 2015; MacCready et al., 2021).

2.3.6. Biogeochemical Model

In the biogeochemical model, an hourly mass balance is estimated from the 30-d LPF time series using

$$\frac{dDIC}{dt}h = F_{adv} + F_{gas} + NEM \quad (2.4)$$

where F_{adv} is the advective flux, F_{gas} is flux due to gas exchange with the atmosphere, NEM is the net ecosystem metabolism, and the term on the left is the finite difference in observed DIC for each time step multiplied by water depth (h). Due to the interpolation interval of 1 hr (see above), all of the terms used in Equation 4 are on an hourly time step even though the observations and advection terms have been passed through a low pass digital filter. Because the mass balance is framed in carbon units from the perspective

of bulk seawater composition a gain (loss) of carbon is reflected as positive (negative) such that ingassing is positive, outgassing is negative, net heterotrophic NEM is positive and net autotrophic NEM is negative. F_{gas} is calculated from Wanninkhof, 2014,

$$F_{gas} = 7.7 \times 10^{-4} \times U^2 \times \Delta pCO_2/(365 \times 24) \quad (2.5)$$

where U is hourly wind speed (m s^{-1}). The ΔpCO_2 is the difference between the measured atmospheric pCO_2 and pCO_2 derived from pH and DIC measurements.

Advective flux, $F_{adv,}$ is calculated from the gradient between the lagoon and ocean using

$$F_{adv} = Q \times (DIC_{lagoon} - DIC_{ocean}) \quad (2.6)$$

where the average flow rate, ($Q = 7.7 \times 10^3$ m^3 hr^{-1}) is the flushing time determined above (T_f = 7d) combined with the average volume of the outer lagoon:

$$Q = \frac{V_{outer}}{T_f} \quad (2.7)$$

DIC_{lagoon} is a dynamic value, estimated from the instrument in the outer lagoon and the ocean endmember, DIC_{ocean}, is taken as a constant 2019 ± 13 µmol kg^{-1} based on observations previously reported for the surf zone at the nearby Scripps Pier (Takeshita et al., 2015). Based on the absence of a distinguishable annual cycle in the LPF A_T, advection of A_T is not parameterized in the biogeochemical model. The mean A_T of the instrument in the lagoon (2232 from the LPF data) falls in-between two previously published values in the nearby coastal ocean (2240 ± 7 µmol kg^{-1}; Takeshita et al., 2015) and 2223 ± 11 µmol kg^{-1}; Bockmon et al., 2013).

Rearranging the mass balance,

$$NEM = \frac{dDIC}{dt}h - F_{adv} - F_{gas} \quad (2.8)$$

To approximate uncertainty, the error for each term on the RHS of Equation 2.8 was estimated and propagated by re-calculation of the NEM time series. For the observational term (dDIC/dt) an error of ± 10 µmol kg^{-1} was introduced. The gas exchange error was based on a 25% change in gas transfer velocity. Advection error was estimated from a combined error of T_F ± 1 day and DIC_{ocean} of ± 13.

2.3.7. Driver Decomposition

The results from the biogeochemical model are used to assess the change in observed parameters (Figure 2.2) due to each "driver": temperature, advection, gas exchange, and NEM. The effect of each driver throughout the year is assessed by holding all other variables constant while allowing one to vary. Williams et. al. (2018) applied this approach using the equations (with pH as the example):

$$\Delta pH_t^{temp} = pH(TA_{t0}, DIC_{t0}, S_{t0}, T_t) - pH_{t0} \quad (2.9)$$

$$\Delta pH_t^{adv} = pH\left(TA_{t0}, DIC_t^{adv}, S_{t0}, T_{t0}\right) - pH_{t0} \quad (2.10)$$

$$\Delta pH_t^{gas} = pH\left(TA_{t0}, DIC_t^{gas}, S_{t0}, T_{t0}\right) - pH_{t0} \quad (2.11)$$

$$\Delta pH_t^{NEM} = pH(TA_{t0}, DIC_t^{NEM}, S_{t0}, T_{t0}) - pH_{t0} \quad (2.12)$$

Where the driver in each equation is represented as an array of time, t, while all other terms are scalars equal to the first point in the time series, t0. The integrated effect of advection, gas exchange, and NEM on DIC (DIC_t^{adv}, DIC_t^{gas}, and DIC_t^{NEM}) have been determined previously in the mass balance. Treating the time series as a closed system and using the driver terms as shown in Equations 2.9-2.12 works reasonably well when a given DIC driver exhibits a seasonal cycle resulting in little net change annually and varies on the same order as the observed DIC, in this case ~130 µmol kg^{-1} (ca. 2100 to 1970, Figure 2.2B). In a system such as the AHL, where large *uni-directional* terms (i.e. advection and NEM) balance

a much smaller observed annual signal, the decomposition calculation cannot be treated as a closed system as in Williams et al. (2018). This would effectively allow Equations 2.10 and 2.12 to freely drive DIC outside of the observed range, which is problematic due to the nonlinear nature of the CO_2 system. For example, converting integrated F_{adv} into an accumulated annual change in DIC results in a DIC decrease of nearly 2000 μmol kg^{-1} which would reduce the initial DIC_{t0} of 2048 μmol kg^{-1} to a near-zero value; whereas the actual observed DIC never falls below 1970 μmol kg^{-1}. Partial derivatives (aka Revelle Factors, Egleston et al., 2010; Frankignoulle, 1994) of the CO_2 system are far different at near zero vs. the observed range in this work (DIC = 2100 – 1970) resulting in unrealistic results when using Equations 2.10 and 2.12. A more realistic approach to driver decomposition in a system such as the AHL requires linearizing Equations 2.10 and 2.12 from partial derivatives representative of the local temperature, salinity, alkalinity and observed range of DIC. Here, the linearization is performed over a 100 μmol kg^{-1} range of DIC (2000 – 2100) at temperature and salinity at time = 0 to obtain

$$\frac{\partial pH}{\partial DIC} = 0.0023; \quad \frac{\partial pCO_2}{\partial DIC} = 3.1; \quad \frac{\partial \Omega_{arag}}{\partial DIC} = 0.0094;$$

and equations 2.10 and 2.12 become

$$\Delta pH_t^{adv} = \frac{\partial pH}{\partial DIC} DIC_t^{adv} - pH_{t0} \tag{2.13}$$

$$\Delta pH_t^{NEM} = \frac{\partial pH}{\partial DIC} DIC_t^{NEM} - pH_{t0} \tag{2.14}$$

2.4. Results

The measured and derived CO_2 parameters from January to December 2018 are shown in Figure 2.2 panels A-F. Each panel shows LPF processed data with the exception of atmospheric pCO_2 in panel A. The LPF pCO_2 ranges from ~ 400 μatm to 800 μatm with a maximum in the spring and a minimum in the summer (Figure 2.2A). The pH ranges from 7.7 to 8.1 annually, showing an inverse correlation with pCO_2 (Figure 2.2D). The annual cycle of both properties is convoluted due to the competing effects of transport, NEM and temperature. The atmospheric CO_2 signal fluctuates from 400 to 500 μatm over the

year and does not surpass the AHL pCO_2, except during very short-lived spikes where a local atmospheric plume may interact with the system's intake port. DIC peaks in early spring to a maximum of 2100 μmol kg^{-1} and reaches a minimum of ~1975 μmol kg^{-1} by summer, resulting in an annual amplitude of ~125 μmol kg^{-1}. Salinity (Figure 2.2C) and A_T (Figure 2.2E), remain relatively stable over the annual cycle, except during major rain events; in particular during January and December. During a pronounced rain, salinity may decrease to as low as 30. Saturation state Ω_{arag} (Figure 2.2F) ranges between roughly 2 - 3, with short term excursions that may briefly approach 1.5 and >3. An $\Omega_{arag} < 1$ is indicative of undersaturated waters and is considered unfavorable to calcifying organisms (Harris et al., 2013), and while the AHL surface waters do not go below this threshold, there are periods, especially during the winter months where Ω_{arag} briefly reaches levels close to undersaturation.

Areal flux and the associated depth + time integrated changes in each driver are shown in Figure 2.5 A and B, respectively and reported in Table 2.3. Although the observed DIC (solid black line) is close to balanced over the 1 yr period, the most significant drivers are far from balanced (Figure 2.5B). The negative flux due to gas exchange represents a continuous source of CO_2 to the atmosphere throughout the year (on average 2.4 mmol C m^{-2} d^{-1}, Table 2.3), the advective flux reverses direction for nearly 3 months in late summer acting as a net sink, presumably due to a state of net autotrophy in the lagoon. Similar to the gas flux, the characteristics of advective flux are also evident in Figure 2.2B, where DIC of the lagoon is higher than the ocean endmember for 10 months of the year but lower during the period of the reversal. Because F_{adv} is the largest calculated term in Equation 2.4 (Figure 2.5) the NEM balance (Equation 2.8) is necessarily a reflection of the F_{adv} input. The result is a mass balance where NEM exhibits net heterotrophy during the 9 months of advective export to the ocean and 3 months of net autotrophy during the summer reversal, leading to an annualized NEM of 34 mmol C m^{-2} d^{-1} (Table 2.3).

.

Following its peak in March, the observed DIC begins a 6 month decrease (Figure 2.2B, Figure 4B), corresponding to a change in sign in the solid black line in Figure 2.5A. This decrease might be separated into two periods, the first consisting of a gradual drop from March to late May followed by a

second period of rapid decrease from June to Aug (Figure 2.5B). The first period corresponds to the highest rates of gas exchange (Figure 2.5A) under the largest gradients in both pCO_2 (Figure 2.2A) and DIC (Figure 2.2B). Based on the mass balance, the lagoon remains net heterotrophic during the course of the first period defined above. Assuming for the moment that F_{adv} is accurate, beginning in late May, NEM rapidly moves from net respiration to net production, reaching a net autotrophic state in late June (Figure 2.5A). When the observed DIC changes inflect again in early August (Figure 2.5A), the reversal leads the change in trophic state by only 1 month, compared to a 3-month lead time during the first reversal.

The decomposition results (Figure 2.6A-C) represent the accumulated effect on pH, pCO_2, and Ω_{arag} throughout the year due to temperature, advection, gas exchange, and NEM. Because (mathematically in our model) NEM is the balance of the other processes, and advection is by far the greatest driver, NEM mirrors advection in all cases. Advection and NEM drove opposing accumulated changes of roughly ± 4 in pH, ± 5000 in pCO_2 and ± 15 in Ω_{arag}, representing a roughly 10-fold greater effect than gas exchange and temperature (compare left vs. right axis ranges). The advective export of DIC from the lagoon (Figure 2.5B) results in a very large forcing to drive pH and Ω higher and pCO_2 lower (Figure 2.6), which must be balanced by equally high respiration through the NEM.

2.5. Discussion

Similar to most of the open ocean, the system described in this study experiences an annual CO_2 cycle. However, unlike the ocean where temperature is often the dominant driver of the CO2 system (Takahashi et al., 2002), the annual cycle of CO_2 in the AHL appears (based on our model) to be almost entirely influenced by seasonality in advective flux and NEM (Figure 2.6). Temperature drives a seasonal cycle in every case but this signal is masked by the overlapping and much larger reversal in advection and NEM noted above. From the perspective of organisms sensitive to Ω, pH, or pCO_2, it is clear from Figure 2.6 that these parameters are primarily influenced by flushing and metabolic rate such that any perturbation to the advection (flushing of the lagoon) or respiration rate (organic and nutrient loads) may

result in dramatic changes in these parameters of the CO_2 system. Thus, stakeholders (shellfish growers, for example) should be aware of changes that might impact flushing time, in particular.

Based on the estimated fluxes and their effects on DIC concentration (Figure 2.5B), in a mass balance of the AHL, the magnitude of advection will ultimately determine the estimate of NEM. Over the course of the one-year time series, the integrated NEM was 42 mmol C m^{-2} d^{-1}. As a simple arithmetic check on this number one can take a steady-state approximation where dDIC/dt = 0 and, ignoring F_{gas}, arrive at the simplified approximation:

$$NEM = \frac{(DIC_{lagoon} - DIC_{ocean})}{T_{res}} h \quad (2.15)$$

It is evident that, from the average lateral DIC anomaly between the ocean and the lagoon (29 mmol m^{-3}), the average depth of 8 m and average flushing time of 7 days, the resulting average NEM (33 mmol C m^{-2} d^{-1}) is essentially identical to that obtained by a more rigorous balancing of terms in Equation 2.8. Nevertheless, it is instructive to use a temporally evolving mass balance rather than a steady state simplification because it enables an examination of seasonality and driver decompositions as presented here. Furthermore, it is only possible to accurately assess the mean gradient (Figure 2.2B) after collecting a near continuous annual time series, as sporadic point sampling throughout the year would lead to significant misrepresentation of a gradient that might be used in a steady state approximation.

A NEM of 34 mmol C m^{-2} d^{-1} falls slightly below the average of 55 mmol C m^{-2} d^{-1} (range of -21 to 180) reported in the compilation of US estuaries assembled by Caffrey (2004). Although the name Agua Hedionda, or "foul-smelling water", suggests a high rate of respiration, the heterotrophic rate is actually on the lower end of the range reported by Caffrey across the 42 NERRs sites. This is explained by the fact that, when the lagoon was named, it was not connected to the ocean. The opening of AHL in 1954 radically altered the flushing leading to a system with metabolic rates similar to other tidal estuaries. For comparison to other local data, in a recent study, under similar conditions in the AHL but over short periods we estimated NEM in the range -20 to 20 mmol C m^{-2} d^{-1} (Shipley et al., 2022). Interestingly, the Shipley et. al. (2022) NEM estimates are based on the analysis of daily amplitudes from a different

instrument using an approach that is independent of flushing time. Due to the differences in observational data and approach to NEM computation, The Shipley et al. (2022) NEM values could be considered as mostly independent from the model approach used in this study. Of particular importance is the one month of corresponding data between the analysis of Shipley et. al., 2022 and this work. During the month of Nov 2018, the in situ sensor used by Shipley et al., (2022) overlapped in time and was located within ~100 m of the instrument used in this study. For Nov 2018, the NEM derived from daily amplitude of the in situ sensor was ~20 mmol C m^{-2} d^{-1}, while the LPF-based mass balance used in this study returned a value of 25 mmol C m^{-2} d^{-1}. This level of agreement is quite encouraging, given the different approaches used between the two studies.

Since the outer lagoon is the only part of the AHL connected directly to the ocean, and the biogeochemical model estimates advection based on measurements in the outer lagoon, the advective flux reported in Table 2.3 should reflect the export of the entire AHL. The most noteworthy comparison to this study is the work of Paulsen et al. (2017) in the nearby San Dieguito Lagoon (SDL). The SDL provides an excellent comparison because it shares the neighboring watershed to the AHL and, thus, a highly similar climate, ecosystem and geomorphology. Using a classic approach of point sampling during selected periods of high/low tide, Paulsen et al. (2017) developed an estimate of the annual carbon export for the SDL. In their work, the combined inorganic and organic (DIC + TOC) export is estimated to be 10 to 25 × 10^6 mol C yr^{-1}. As pointed out by Paulsen et al., the inorganic to organic composition of carbon export is sensitive to runoff and frequency of storm events but, on average, total carbon export consisted of ~80% DIC, suggesting a DIC export from the SDL of ~8 to 20 × 10^6 mol C yr^{-1} or roughly 3 to 8x that estimated for the AHL in this study. It stands to reason that the much larger natural watershed area of the SDL compared to the AHL (more than 10×) should lead to a greater export flux. On the other hand, the vast majority of river flow in all of San Diego County is captured by reclamation, leading to tidal lagoons with little to zero river input during much of the year and therefore making natural watershed area less important than a more immediate or “effective” catchment area as defined above in the mixing model

used here. In short, human driven changes in land use may help to explain how a >10× difference in natural watershed may translate into a 3-8× difference in export between the SDL and AHL.

One of the most counterintuitive properties of coastal systems is the distinction between pCO_2 saturation and trophic status (net autotrophic vs heterotrophic). Many coastal embayments, lagoons, and estuaries exist in a net heterotrophic state that help to sustain a pCO_2 that is higher than the atmosphere. However, since NEM (not pCO_2) defines trophic state, it is insufficient and incorrect to judge trophic status based on pCO_2 (or similarly O_2) alone. For example, in the AHL, pCO_2 is supersaturated with respect to the atmosphere acting as a consistent source of CO_2 throughout the year 2018 (Figure 2.2A, Figure 2.5A), yet, the system is net autotrophic for two months of the year (July-Aug, Figure 2.5A). Interesting in its own right is a comparison of the gas exchange flux between 2018 and 2020 (Figure 2.7). As discussed by Shipley et al. (2022), a red tide in early 2020 resulted in an extreme event that drove the AHL into a brief state of hypoxia. During a period of only a few weeks in May 2020, the outer lagoon reached peak heterotrophic rates of 140 mmol C m^{-2} d^{-1} and off-gassed the equivalent of >50% of the full year of CO_2 flux observed in 2018. Interestingly, the peak NEM rates observed in 2020 during the hypoxic event were only moderately higher than the peak rates observed in 2018 (~120 mmol C m^{-2} d^{-1} during March 2018, Figure 2.5A). This again highlights the importance of distinguishing between pCO_2 flux and trophic state. Based on nearby data at the Scripps Pier (Clements et al., 2020), the widespread nature of the 2020 red tide likely led to a high DIC in the adjacent ocean, which would result in diminished advective export, driving pCO_2 very high in the lagoon without the requirement for a massive jump in NEM. In summary, we hope that the simple comparison in Figure 2.7 provides some insight on the potential for shallow coastal environments to exhibit abrupt changes. This observation also highlights the need for improved spatiotemporal observations in estuaries to better assess their contributions to the global carbon budget.

2.6. Conclusions

In the work, we have demonstrated the temporal variability of carbonate species and attempted to quantify the annual inorganic carbon budget of the AHL. In this first-of-its kind attempt to quantify

carbon fluxes in this lagoon, we identified the importance of collecting a temporally-resolved dataset along with various challenges associated with interpreting data in a highly dynamic environment such as the AHL. While the average results of our simple biogeochemical model are in line with expectations based on similar lagoon systems, the rather large estimates of uncertainty associated with the reported annual budget reflect room for improvement in observing strategy.

The model used in this study is part mechanistic and part inverse. Physical processes (mixing, gas flux) have been parameterized mechanistically while the biological component (NEM) is determined as the balance of these physical processes along with observations. A full mechanistic model of the system could provide additional insight. For example, in forecasting AHL conditions under a new scenario such as enhanced circulation associated with the desalination plant and dredging, NEM might be assumed to follow the average or seasonal pattern determined in this study, combined with a new flushing time. This approach would only provide satisfactory estimates of lagoon conditions if metabolic rates truly remain unchanged by flow. In the case where flow rates affect metabolic rates (e.g. by modulating nutrient and organic matter inputs), parameterization of NEM from variables such as nutrient and organic matter concentration, irradiance, and chlorophyll may prove useful. Similarly, a more complex treatment of physics through a hydrodynamic model coupled with a DIC mass balance could provide a more realistic description of the lagoon at the shorter time scales that were intentionally removed by the LPF in our analysis. Based on the demonstrated importance of advection, perhaps the most meaningful improvement to the model developed in this study would involve a better constraint on the temporal changes in DIC in the adjacent ocean by additional SeapHOx sensor(s) and a more comprehensive set of total alkalinity data. In addition, the important role of organic carbon should be addressed in the planning of any future study.

2.7. Acknowledgements

The authors would like to thank Stephanie Smith provided essential technical assistance to maintain the instrument in the field. We thank Thomas Grimm and the Carlsbad Aquafarm for providing space and support for the automated analyzer. We also thank Clarissa Anderson and others at SCCOOS for supporting observations at the AHL.

Chapter 2, in full, is being prepared for submission as: Shipley, K., Martz, T., Hales, B., Giddings, S., Andersson, A. (2022) Physical and Biological Controls on the Seasonal CO_2 Cycle in the Agua Hedionda Lagoon, Carlsbad, CA. The dissertation author was the primary investigator and first author of this paper.

2.8. Tables and Figures

Table 2.1. Inputs to the 4-box mixing model. Areas and volumes at MLLW taken from Elwany et al., 2005.

Input	Value
Area outer lagoon	2.0×10^5 m^2
Area middle lagoon	1.0×10^5 m^2
Area inner lagoon	6.1×10^5 m^2
Volume outer lagoon	1.2×10^6 m^3
Volume middle lagoon	4.0×10^5 m^3
Volume inner lagoon	1.3×10^6 m^3
Tide height	hourly tide height
Rain	hourly cm hr^{-1}

Table 2.2. Inputs to the 1-box biogeochemical model, in addition to other terms for the outer lagoon noted above in Table 2.1.

Input	Value
CF	21
RF	0.0
RE	0.95
pCO_2	meas. variable (μatm)
DIC_{lagoon}	meas. variable ($\mu mol\ kg^{-1}$)
DIC_{ocean}	2019 $\mu mol\ kg^{-1}$

Table 2.3. Results of the 2018 mass balance. Negative values represent a loss from the lagoon. The range indicated by ± represents the propagated errors from the uncertainty estimates used in Equation 2.8. Gas exchange and NEM flux is normalized to the area of the outer lagoon.

Process	**Flux** **mmol C m^{-2} d^{-1}**	**Transport** **$\times 10^6$ mol C yr^{-1}**
Advection (F_{Adv})	N/A	-2.4 ± 1.6
Gas Exchange (F_{gas})	-2.3 ± 0.6	-0.17 ± 0.04
Net Ecosystem Metabolism (F_{NEM})	34 ± 22.5	2.5 ± 1.7

Figure 2.1. Map of the Agua Hedionda Lagoon showing the instrument location (red X) and additional features of interest including the Desalination plant (DP), Encina power station (EPS), the Carlsbad Aquafarm (CAF), Hubbs-SeaWorld fish hatchery (HFH), Strawberry fields (SF), and recreational sports and boating activities (RS). Image from Google Earth.

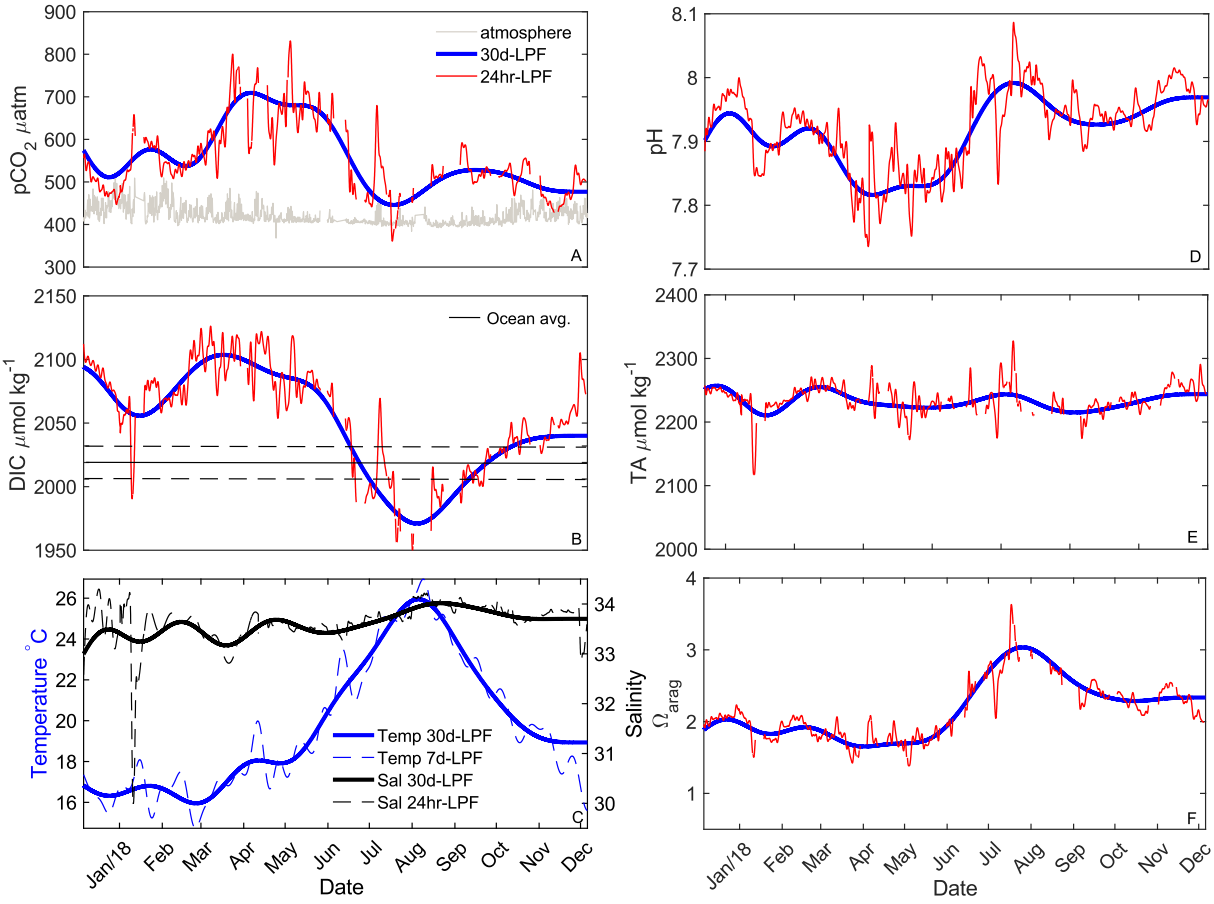

Figure 2.2. Measured CO_2 parameters for 2018 (A-F) from the shore station system. The data shown are low pass filtered at 24 hr (7-day for Temp) and 30-days for each parameter. In panel B, the Ocean average at 2019 (solid line) and the 1σ sd of ± 13 µmol kg^{-1} (dashed lines).

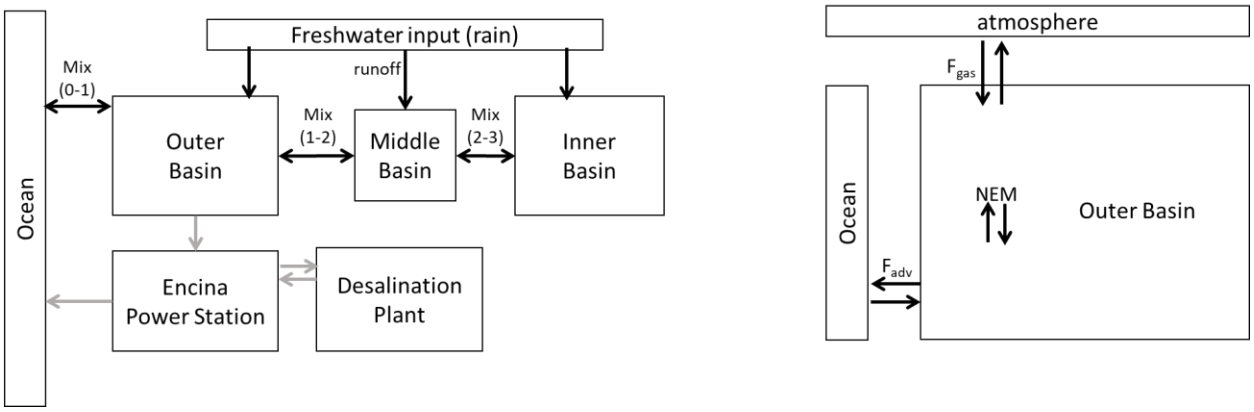

Figure 2.3. Mixing model (left) used to determine flushing time based on salinity observations during Nov 2018. Exchange between the ocean and three basins of the lagoon is driven by tidal mixing and basin geometry. Freshwater input is parameterized based on rain and effective catchment area. Flow represented by grey arrows was not parameterized, but its effect is included in observed data that are used to constrain the model (see text). Biogeochemical model (right) used to estimate NEM based on dissolved inorganic carbon data. NEM is the balance of observed changes, gas flux and advection.

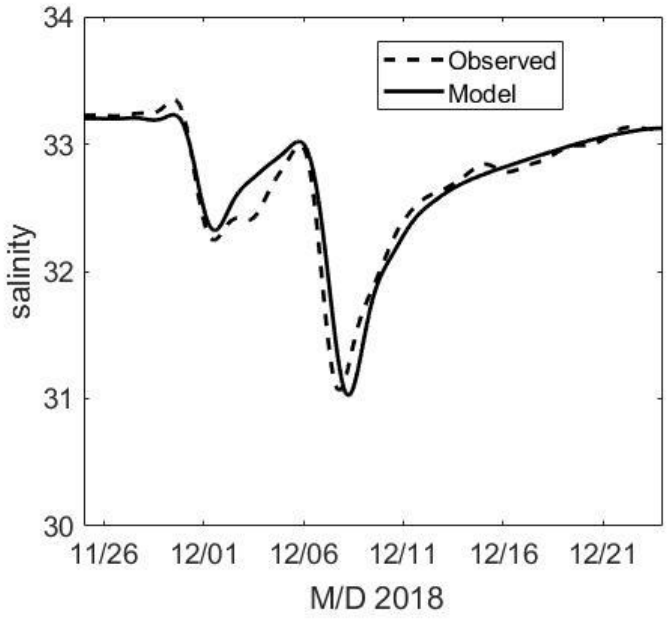

Figure 2.4. Results of the 4-box mixing model compared to salinity observed in the outer lagoon during two major rain events in Dec 2018. Mixing parameters are tuned based on the 24-hr LPF data.

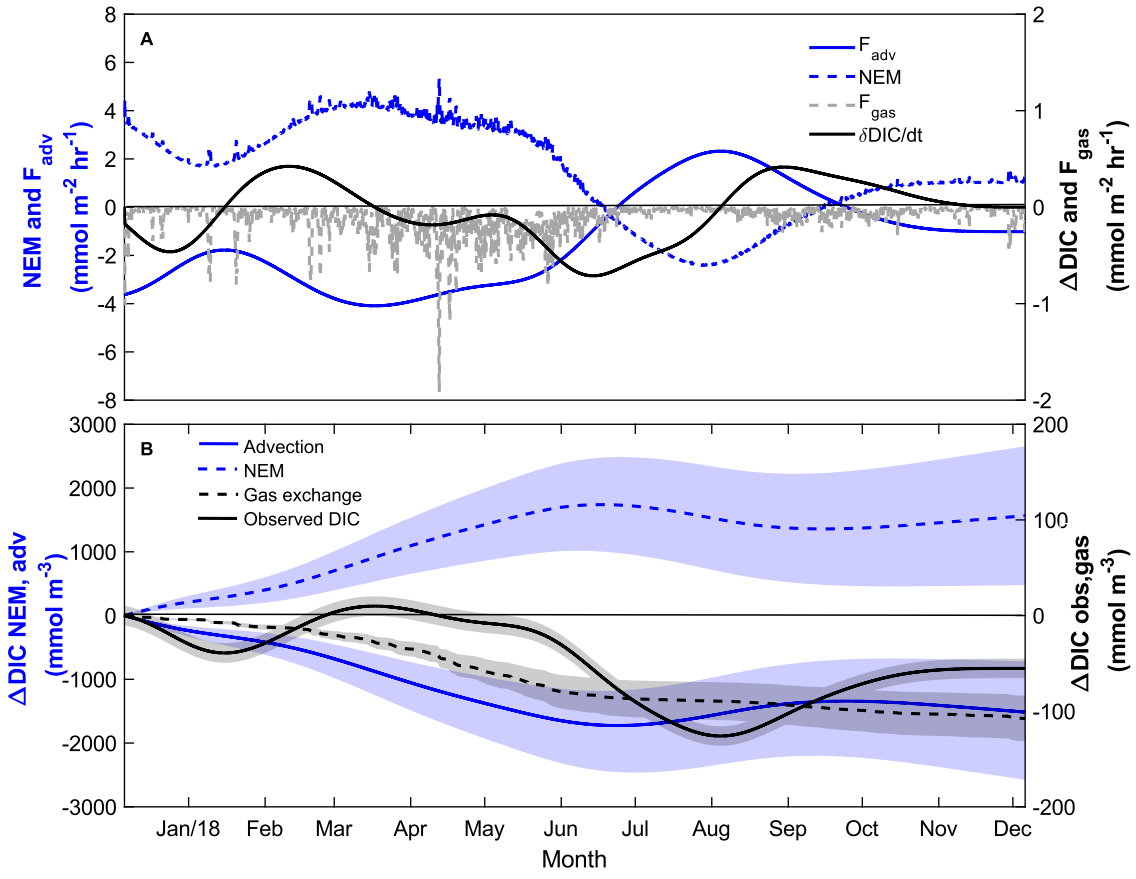

Figure 2.5. (A) Areal flux from mass balance (Equation 2.8) and (B) the time and depth integrated changes.

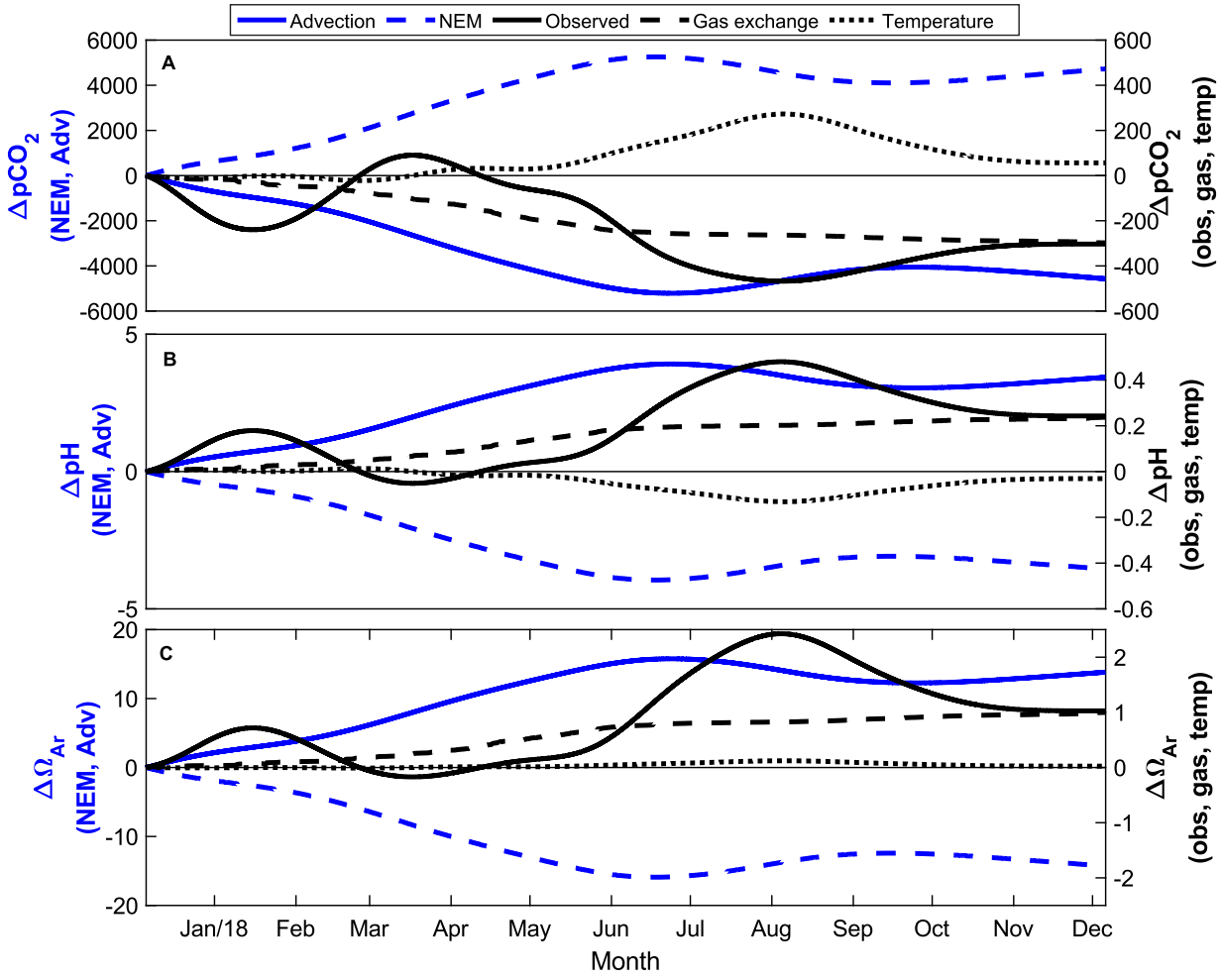

Figure 2.6. Driver decomposition for pCO_2 (A), pH (B), and Ω_{Arag} (C). Blue lines correspond to the left y-axis and black lines to the right y-axis.

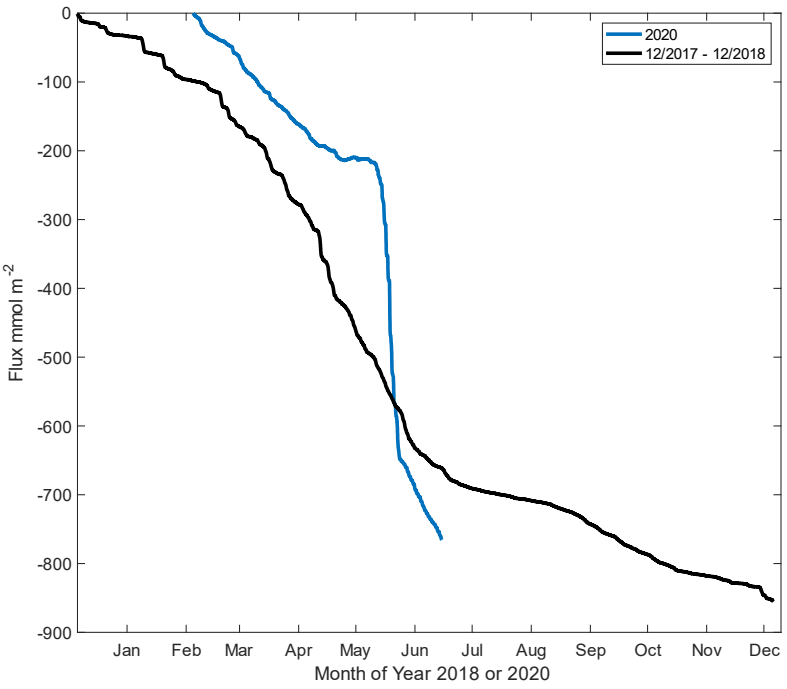

Figure 2.7. Accumulated CO_2 air-sea flux during the 365-d period of 2017/2018 and a 4 mo period of 2020 (2020 data from Shipley et al., 2022).

2.8. References

Bandstra L, Hales B, Takahashi T. 2006. High-frequency measurements of total CO2: Method development and first oceanographic observations. *Marine Chemistry* **100**(1–2): 24–38. doi: 10.1016/j.marchem.2005.10.009

Barton A, Hales B, Waldbusser GG, Langdon C, Feely RA. 2012. The Pacific oyster, Crassostrea gigas, shows negative correlation to naturally elevated carbon dioxide levels: Implications for near-term ocean acidification effects. *Limnology and Oceanography* **57**(3): 698–710. doi: 10.4319/lo.2012.57.3.0698

Barton A, Waldbusser GG, Feely RA, Weisberg SB, Newton JA, Hales B, Cudd S, Eudeline B, Langdon CJ, Jefferds I, King T, Suhrbier A, McLaughlin K. 2015. Impacts of coastal acidification on the Pacific Northwest shellfish industry and adaptation strategies implemented in response. *Oceanography* **28**(2): 146–159. doi: 10.5670/oceanog.2015.38

Bauer JE, Cai W-J, Raymond PA, Bianchi TS, Hopkinson CS, Regnier PAG. 2013. The changing carbon cycle of the coastal ocean. *Nature* **504**(7478): 61–70. doi: 10.1038/nature12857

Beller E, Baumgarten S, Grossinger R, Longcore T, Stein E, Dark S, Dusterhoff S. 2014. Northern San Diego County lagoons historical ecology investigation. San Francisco Estuary Institute Publication #722. Available at https://www.sfei.org/documents/northern-san-diego-county-lagoons-historical-ecology-investigation.

Bockmon EE, Frieder CA, Navarro MO, White-Kershek LA, Dickson AG. 2013. Technical Note: Controlled experimental aquarium system for multi-stressor investigation of carbonate chemistry, oxygen saturation, and temperature. *Biogeosciences* **10**(9): 5967–5975. doi: 10.5194/bg-10-5967-2013

Cai W-J. 2011. Estuarine and coastal ocean carbon paradox: CO2 sinks or sites of terrestrial carbon incineration? *Annual review of marine science* **3**: 123–45. doi: 10.1146/annurev-marine-120709-142723

Cai WJ, Feely RA, Testa JM, Li M, Evans W, Alin SR, Xu YY, Pelletier G, Ahmed A, Greeley DJ, Newton JA, Bednarscaronek N. 2021. Natural and Anthropogenic Drivers of Acidification in Large Estuaries. *https://doi.org/101146/annurev-marine-010419-011004* **13**: 23–55. Annual Reviews. doi: 10.1146/annurev-marine-010419-011004

City of Carlsbad. 2005. Final Environmental Impact Report: Precise Development Plan and Desalination Plant. SCH#2004041081. Prepared by Dudek & Associates, Inc.

City of Carlsbad (2022). Carlsbad WMA Water Quality Improvement Plan FY21 Annual Report. https://projectcleanwater.org/download/carlsbad-wqip-2020-2021-annual-report/

Clements, S.C., Takeshita Y., Dickson A., Martz T., and Smith J.E. 2020, Scripps Ocean Acidification Real-time (SOAR) Dataset, Scripps Institution of Oceanography, La Jolla, CA.

Doney S, Balch W, Fabry V, Feely R. 2009. Ocean Acidification: A Critical Emerging Problem for the Ocean Sciences. *Oceanography* **22**(4): 16–25. doi: 10.5670/oceanog.2009.93

Egleston ES, Sabine CL, Morel FMM. 2010. Revelle revisited: Buffer factors that quantify the response of ocean chemistry to changes in DIC and alkalinity. *Global Biogeochemical Cycles* **24**(1). doi: 10.1029/2008GB003407

Elwany H, Flick R, White M. 2005. Agua Hedionda Lagoon hydrodynamic studies.

Evans W, Hales B, Strutton PG. 2011. Seasonal cycle of surface ocean pCO2 on the Oregon shelf. *Journal of Geophysical Research: Oceans* **116**(5): 1–11. doi: 10.1029/2010JC006625

Fairchild W, Hales B. 2021. High-Resolution Carbonate System Dynamics of Netarts Bay, OR From 2014 to 2019. *Frontiers in Marine Science* **7**. Frontiers Media S.A. doi: 10.3389/fmars.2020.590236

Feely RA, Alin SR, Newton J, Sabine CL, Warner M, Devol A, Krembs C, Maloy C. 2010. The combined effects of ocean acidification, mixing, and respiration on pH and carbonate saturation in an urbanized estuary. *Estuarine, Coastal and Shelf Science* **88**(4): 442–449. Elsevier Ltd. doi: 10.1016/j.ecss.2010.05.004

Feely RA, Sabine CL, Hernandez-ayon JM, Ianson D, Hales B. 2008. Evidence for Upwelling of Corrosive Continental "Acidified"water onto the continental Shelf. *Science* **1490**(2008): 1–4. doi: 10.1126/science.1155676

Frankignoulle M. 1994. A complete set of buffer factors for acid/base CO2 system in seawater. Journal of Marine Systems.

Gruber N, Hauri C, Lachkar Z, Loher D, Frolicher TL, Plattner G-K. 2012. Rapid Progression of Ocean Acidification in the California Current System. *Science* **337**(6091): 220–223. doi: 10.1126/science.1216773

Hales B, Chipman DW, Takahashi TT. 2004. High-frequency measurement of partial pressure and total concentration of carbon dioxide in seawater using microporous hydrophobic membrane contactors. *Limnology and Oceanography: Methods* **2**: 356–364. doi: 10.4319/lom.2004.2.356

Hales B, Takahashi T, Bandstra L. 2005. Atmospheric CO2 uptake by a coastal upwelling system. *Global Biogeochemical Cycles* **19**(1): 1–11. doi: 10.1029/2004GB002295

Harris KE, DeGrandpre MD, Hales B. 2013. Aragonite saturation state dynamics in a coastal upwelling zone. *Geophysical Research Letters* **40**(11): 2720–2725. doi: 10.1002/grl.50460

Hauri C, Gruber N, Plattner G-K, Alin S, Feely R, Hales B, Wheeler P. 2009. Ocean Acidification in the California Current System. *Oceanography* **22**(4): 60–71. doi: 10.5670/oceanog.2009.97

Howarth R, Chan F, Conley DJ, Garnier J, Doney SC, Marino R, Billen G. 2011. Coupled biogeochemical cycles: Eutrophication and hypoxia in temperate estuaries and coastal marine ecosystems. *Frontiers in Ecology and the Environment* **9**(1): 18–26. doi: 10.1890/100008

Jenkins S, Wasyl J. 2006. Coastal process effects of reduced intake flows at Agua Hedionda Lagoon.

Kessouri F, McWilliams JC, Bianchi D, Sutula M, Renault L, Deutsch C, Feely RA, McLaughlin K, Ho M, Howard EM, Bednaršek N, Damien P, Molemaker J, Weisberg SB. 2021. Coastal eutrophication

drives acidification, oxygen loss, and ecosystem change in a major oceanic upwelling system. *Proceedings of the National Academy of Sciences of the United States of America* **118**(21): 1–8. doi: 10.1073/pnas.2018856118

Largier JL, Hollibaugh JT, Smith S V. 1997. Seasonally Hypersaline Estuaries in Mediterranean-climate Regions. Estuarine, Coastal and Shelf Science.

Largier J. 2010. Low-inflow estuaries: hypersaline, inverse, and thermal scenarios. *Contemporary Issues in Estuarine Physics*: 247–272.

Lemagie EP, Lerczak JA. 2015. A Comparison of Bulk Estuarine Turnover Timescales to Particle Tracking Timescales Using a Model of the Yaquina Bay Estuary. *Estuaries and Coasts* **38**(5): 1797–1814. Springer New York LLC. doi: 10.1007/s12237-014-9915-1

MacCready P, McCabe RM, Siedlecki SA, Lorenz M, Giddings SN, Bos J, Albertson S, Banas NS, Garnier S. 2021. Estuarine Circulation, Mixing, and Residence Times in the Salish Sea. *Journal of Geophysical Research: Oceans* **126**(2). Blackwell Publishing Ltd. doi: 10.1029/2020JC016738

Monsen NM, Cloern JE, Lucas L V. 2002. A comment on the use of flushing time, residence time, and age as transport time scales. *Notes: Limnology and Oceanography* **47**(5): 1545–1553.

Nam S, Send U. 2011. Direct evidence of deep water intrusions onto the continental shelf via surging internal tides. *Journal of Geophysical Research: Oceans* **116**(5). Blackwell Publishing Ltd. doi: 10.1029/2010JC006692

NOAA Office for Coastal Management. 2017. The National Estuarine Research Reserve System: Strategic Plan 2017-2022. Available at https://coast.noaa.gov/data/docs/nerrs/StrategicPlan.pdf.

Paulsen, M.-L.; Andersson, A. J.; Aluwihare, L.; Cyronak, T.; D'Angelo, S.; Davidson, C.; Elwany, H.; Giddings, S. N.; Page, H. N.; Porrachia, M.; Schroeter, S., Temporal Changes in Seawater Carbonate Chemistry and Carbon Export from a Southern California Estuary. Estuaries and Coasts 2018, 41 (4), 1050-1068.

Ramesh R, Chen Z, Cummins V, Day J, D'Elia C, Dennison B, Forbes DL, Glaeser B, Glaser M, Glavovic B, Kremer H, Lange M, Larsen JN, Le Tissier M, Newton A, Pelling M, Purvaja R, Wolanski E. 2015. Land-Ocean Interactions in the Coastal Zone: Past, present & future. *Anthropocene* **12**(2015): 85–98. Elsevier B.V. doi: 10.1016/j.ancene.2016.01.005

Shipley K. 2022. Biogeochemical observations and baseline CO2 conditions in the Agua Hedionda Lagoon. University of California San Diego.

Takahashi, T.; Sutherland, S. C.; Sweeney, C.; Poisson, A.; Metzl, N.; Tilbrook, B.; Bates, N.; Wanninkhof, R.; Feely, R. A.; Sabine, C.; Olafsson, J.; Nojiri, Y., Global sea-air CO2 flux based on climatological surface ocean pCO2, and seasonal biological and temperature effects. Deep-Sea Res., Part II 2002, 49 (9-10), 1601-1622.

Takeshita, Y., Frieder, C. A., Martz, T. R., Ballard, J. R., Feely, R. A., Kram, S., Nam, S., Navarro, M. O., Price, N. N., & Smith, J. E. (2015). Including high-frequency variability in coastal ocean acidification projections. *Biogeosciences*, **12**(19), 5853–5870. https://doi.org/10.5194/bg-12-5853-2015

Tilbrook B, Jewett EB, DeGrandpre MD, Hernandez-Ayon JM, Feely RA, Gledhill DK, Hansson L, Isensee K, Kurz ML, Newton JA, Siedlecki SA, Chai F, Dupont S, Graco M, Calvo E, Greeley D, Kapsenberg L, Lebrec M, Pelejero C, et al. 2019. An enhanced ocean acidification observing network: From people to technology to data synthesis and information exchange. *Frontiers in Marine Science* **6**: 1–21. doi: 10.3389/fmars.2019.00337

Waldbusser GG, Salisbury JE. 2014. Ocean Acidification in the Coastal Zone from an Organism's Perspective: Multiple System Parameters, Frequency Domains, and Habitats. *Annual Review of Marine Science* **6**(1): 221–247. doi: 10.1146/annurev-marine-121211-172238

Wang ZA, Kroeger KD, Ganju NK, Gonneea ME, Chu SN. 2016. Intertidal salt marshes as an important source of inorganic carbon to the coastal ocean. *Limnology and Oceanography* **61**(5): 1916–1931. doi: 10.1002/lno.10347

Williams NL, Juranek LW, Feely RA, Russell JL, Johnson KS, Hales B. 2018. Assessment of the Carbonate Chemistry Seasonal Cycles in the Southern Ocean From Persistent Observational Platforms. *Journal of Geophysical Research: Oceans* **123**(7): 4833–4852. doi: 10.1029/2017JC012917

Windham-Myers L, Cai W-J, Alin SR, Andersson A, Crosswell J, Dunton KH, Hernandez-Ayon JM, Herrmann M, Hinson AL, Hopkinson CS, Howard J, Hu X, Knox SH, Kroeger K, Lagomasino D, Megonigal P, Najjar RG, Paulsen M-L, Peteet D, et al. 2018. Tidal wetlands and estuaries. Second state of the carbon cycle report (SOCCR2): A sustained assessment report. doi: 10.7930/soccr2.2018.ch15

Chapter 3. Metabolic Rates in the Agua Hedionda Lagoon during the 2020 Southern California Red Tide Event

3.1. Abstract

A standing SCCOOS time series from autonomous sensors (pH, dissolved oxygen (DO), salinity, temperature) in the Agua Hedionda Lagoon, Carlsbad, CA (AHL) captured the effects of a massive red tide occurring along the Southern & Baja California coast during the spring of 2020. Biogeochemical data (pH and DO) were examined using an open-source model designed to filter out the influence of tides and estimate net ecosystem metabolism (NEM). Contemporaneous pH and DO observations allowed simultaneous, independent evaluations of production, respiration and NEM. Under normal conditions, the AHL tends toward net heterotrophy, averaging 10 mmol C m^{-2} d^{-1}. During a 2-month period, centered around the peak of the event, trophic status in the lagoon shifted multiple times between net heterotrophic and net autotrophic, with a pronounced period of anoxia. Fueled by the intense local bloom, at its peak, respiration reached rates of 140 mmol C $m^{-2}d^{-1}$. We found that the co-location of pH and oxygen sensors affords independent assessment of metabolic rates, which often agree, as expected under baseline (oxic) conditions, but diverge during an extreme event. This observation allowed us to identify non-Redfieldian behavior and speculate on the source of anoxic reactions.

3.2. Introduction

Estuarine environments are uniquely diverse ecosystems located at the land-river-ocean interface. While these systems exhibit great biogeochemical heterogeneity (Bauer et al., 2013; Paulsen et al., 2018), coastal ocean systems are affected by many of the same sets of local drivers, including the adjacent ocean and surrounding landscape through runoff and river discharge (Paerl et al., 2006; Howarth et al., 2011; Windham-Myers et al., 2018). In comparison to offshore ecosystems, near-shore ecosystems are more often subjected to anthropogenic stressors, which makes understanding the metabolic state of these systems of great importance (Hewitt et al., 2005). Foremost, the balance between production and respiration is necessary for estimating net ecosystem metabolism (NEM), which defines whether a system

is heterotrophic or autotrophic (Caffrey, 2003). Many estuarine systems experience both trophic states in a single day, some shift between states on a seasonal basis, and the vast majority appear to exhibit net heterotrophy, on average, presumably due to organic loading from land runoff (Smith and Hollibaugh, 1993; Hopkinson and Vallino, 1995; Gattuso et al., 1998; Caffrey, 2004). DO is the most common measurement used to assess trophic conditions, as the value provides immediate information about the various thresholds (e.g., hypoxia, anoxia). DO is also the variable most widely used to establish NEM rates for coastal ocean systems (Breitburg et al., 2008). Both oxic status and NEM rates are fundamental to understanding ecosystem health and, specifically, deleterious effects of eutrophication and red tides (Conley et al., 2009).

Though not fully predictable, red tides can develop whenever conditions favor a strong phytoplankton bloom and tend to correspond to both natural processes such as upwelling and human sources such as nutrient and wastewater runoff from land (Horner et al., 1997). A particularly intense red tide event occurred from the end of March 2020 through June 2020 off the southern California coast. Based on satellite data, the bloom extended from Baja California to Los Angeles; with peak Chl-a concentrations (sampled manually at the Scripps Pier) reaching 867 mg m^{-3} on April 27, 2020 (Kahru et al., 2021). This event was driven by the bioluminescent phytoplankton *Lingulodinium polyedra*, a predominantly non-toxic species in the Southern California region, but known to cause discoloration and post-bloom oxygen depletion (Horner et al., 1997; Armstrong and Kudela, 2006). During the peak of the bloom at the Scripps Pier, *L. Polyedra* counts were 9,170 cells mL^{-1} (Kahru et al., 2021). Non-toxic red tide events can be dangerous to aquatic species, often resulting in adverse impacts to ecosystem health by creating anoxic conditions that lead to fish kills (Anderson et al., 2012).

The primary objective of this study was to analyze biogeochemical observations from two different periods at the Agua Hedionda Lagoon (AHL), Carlsbad, California: a “normal” period in 2018 serving as the baseline condition against which we compare the extreme conditions observed during 2020, when a heavy storm preceded a red tide event. The datasets used in this work derive from a Southern California Coastal Ocean Observing System (SCCOOS) monitoring site that was originally installed for

the purpose of providing near real time water quality information to an aquaculture facility. Due to a continuous presence in the lagoon, the sensor-based time series captured an event that would have otherwise been missed due to the transient nature of the bloom and the considerable time required (typically months) to plan, mobilize, and deploy in situ assets. As an opportunistic study of an acidification/hypoxic event (at the height of a global pandemic), the data are naturally limited to assets in the water at the time of the bloom. Because the ancillary measurements (e.g. concentrations of various sulfur and nitrogen species) that would normally be employed in a planned study of hypoxia/anoxia are not available, the work we present here is limited to an assessment of biogeochemical rates that can be derived from pH and Oxygen data. To achieve this, a weighted regression model (WRM) was used to filter out the tidal influence on DO and dissolved inorganic carbon (DIC) in order to obtain the biological signal, expressed here as the metabolic rate of production, respiration, and the net (production – respiration). Following this, we offer a purely speculative discussion of the chemical pathways that could be invoked to explain the observed dynamics in oxygen and pH; however, we must stress that the limited data prevent a definitive statement about the dominant hypoxic/anoxic reactions present during the study.

3.3. Materials and Methods

3.3.1. Study Site

The AHL, located in Carlsbad, CA, is comprised of three interconnected basins, including an outer (26.7×10^4 m^2), middle (10.9×10^4 m^2), and inner basin (1.2×10^6 m^2) (Figure 3.1) (Elwany et al., 2005). The ocean, connected by an inlet in the western side of the outer basin, dominates physical forcing in all three basins, with tidal lags of up to 4 hours at the creek (Jenkins and Wasyl, 2006). The original wetland was converted into the present lagoon structure in 1954 by the Encina Power Station and is maintained in its present form by semi-annual dredging. The AHL consists of >75% open water with the remainder being marsh and mud flats (Beller et al., 2014). Water depths at the lagoon range from very shallow (i.e. < 1 m) up to approximately 14 m in certain areas, with an average depth of 8 m (Elwany et al., 2005). The inner basin receives freshwater input from Agua Hedionda Creek during rain events which

occur primarily in winter and spring. During the rest of the year, the creek runs dry and the lagoon is purely tidal.

The AHL is highly utilized and a popular destination for the Carlsbad community and tourists and provides a thriving ecosystem for many diverse species of plants and animals. The locations of the various businesses within and surrounding the lagoon are also shown in Figure 3.1. The two primary industrial features include the Encina Power Station (fully decommissioned by Jan/2019) and the Carlsbad Desalination Plant, both of which rely on water intake from the outer basin for once-through cooling of the power plant and as desalination source water. During peak operation, the power plant intake, located in the outer basin, could divert greater than 90% of the tidal prism over a tidal cycle; on average, around 50% of the tidal prism was diverted (Elwany et al., 2005). The desalination plant, which began operating in 2016, continues to divert water from the outer basin in order to generate freshwater at a rate of 2.3×10^8 L d^{-1}, which would account for around 20% of the tidal prism being diverted on a daily basis. Other features of the AHL include agriculture (primarily strawberry fields bordering the inner basin), the Hubbs Marine Fish Hatchery, and the Carlsbad Aquafarm (CAF)—a sustainable mussel and oyster farm, which operates in the outer basin. Both the fish hatchery and aquafarm (which grows calcifying organisms sensitive to pH) rely on adequate flushing of the lagoon by the ambient ocean in order to maintain oxygen and calcium carbonate saturation levels above thresholds critical to growth. The primary tool used to accomplish the desired state of the ecosystem in AHL is dredging, which began in 1954 for the power station and transformed the lagoon from a backwater slough into an ocean-connected tidal lagoon.

3.3.2. Sampling

Continuous biogeochemical observations were made from a mooring deployed in the outer basin of the AHL (Figure 3.2). The 2018 mooring was deployed for 69 days, from 11/02/2018 – 01/10/2019. In 2020, the mooring was deployed for 145 days, 01/22/2020 – 06/15/2020. Sensors deployed on the mooring include a SeapHOx (Bresnahan et al., 2014) at a fixed height of 1 m above bottom to measure pH (Honeywell Durafet), DO (Aanderaa optode), temperature and salinity (Sea-Bird SBE-37) and

pressure (Honeywell M5200 series). An additional oxygen-temperature logger (PME miniDOT) was deployed near the surface, but due to lack of anti-fouling protection, the data were determined to be compromised and not used in the analysis. Each sensor was set to record measurements at 30-minute intervals. A surface buoy houses a cellular modem and controller connected directly to the SeapHOx, allowing hourly, real-time data access (Bresnahan et al., 2020). The data are quality controlled and made publicly available by the Southern California Coastal Ocean Observing System (SCCOOS) through an online database (ERDDAP): see https://sccoos.org/ocean-acidification/ and https://erddap.sccoos.org/erddap/tabledap/pH-AHL.html. The mooring was deployed near the CAF mussel and oyster cages (see Figure 3.1) for accessibility and relatively gentle flow (to minimize mooring drag due to tidal current).

3.3.3. Data Processing

Raw, 30-minute data stored onboard were re-processed and quality controlled following recovery of the mooring. Raw oxygen data were salinity corrected, following the manufacturer manual, using data from the SBE-37. pH validation samples were taken during the recovery of the mooring at the beginning of 2019 but were not possible in 2020 due to restrictions associated with the pandemic. For a bottle validation sample, a Niskin was filled near the sensor and then subsampled into a 250 ml borosilicate bottle and poisoned with mercuric chloride ($HgCl_2$). The sample was later analyzed for pH using a benchtop spectrophotometric pH system. A pH correction was applied to the 2018 dataset following Bresnahan et al. (2014). Because the pandemic did not allow for validation samples during the 2020 deployment, the pH sensor offset determined in 2019 was carried forward for 2020 (the same Durafet pH sensor was used in the SeapHOx). Based on our previous experience, we estimate the accuracy of the time series to be 0.05 pH, and in line with the manufacturer's stated accuracy for oxygen (±2 mmol m^{-3}) and salinity (±0.003). As discussed previously (Takeshita et al., 2014; Kapsenberg et al., 2017; Shangguan et al., 2022) the ability of a Durafet pH sensor to accurately resolve short-term (e.g. hourly, diel) changes is > 10× the stated accuracy because, once deployed and conditioned, the sensors have been shown to remain highly stable and exhibit ideal Nernstian behavior. Based on the sensor resolution of

~0.0005 pH, a conditioned sensor can reliably observe relative changes in pH on the order of 0.001, making this a highly capable sensor for capturing the amplitude of diel pH cycles, which range from 0.6 to 0.006 in this study.

CO_2 system calculations were performed using CO2SYS for MATLAB (van Heuven et al., 2011), using equilibrium constants as recommended by (Dickson and Millero, 1987). Phosphate and silicate as inputs to CO2SYS were set to zero because, although they were not measured in this study, a brief campaign in 2016 observed concentrations in these nutrients at levels (maximum observed: Phosphate = .35 µmol L^{-1}; Silicate = 6.7 µmol L^{-1}) that are near-negligible in their effect on pH (~0.001 pH unit). In our analysis, the partial pressure of carbon dioxide (pCO_2) and dissolved inorganic carbon (DIC) were calculated from SeapHOx temperature, salinity, and pH (total proton scale) combined with Total Alkalinity (A_T), estimated from salinity. A local A_T-S relationship was established from data recorded during a runoff event in 2018 where five paired pH and DIC measurements were used to establish the relationship: A_T (µmol kg^{-1}) = 29.2×S+1238 (RMSE = 6.3, R^2 = .98, n = 5) (Shipley 2022). Based on this, an error of 10 µmol kg^{-1} in A_T was used in the sensitivity analysis below. In converting pH to DIC, we have treated A_T as a property conservative with salinity because the canonical factor of ΔA_T:ΔDIC = 0.16 associated with Redfieldian stoichiometry is small relative to the pH signals observed and errors introduced by estimated A_T from S. In order to account for gas exchange, the hourly CO_2 flux (outgassing = negative, ingassing = positive) was calculated using Eq. 3.1 (Wanninkhof, 2014),

$$F = 7.7 \times 10^{-4} \times U^2 \times \Delta pCO_2/(365 \times 24) \quad (3.1)$$

where hourly wind speed (U) was available through the NOAA climate database, measured at the McClellan-Palomar airport in Carlsbad, CA approximately four miles from the AHL (https://www.ncdc.noaa.gov/cdo-web/datasets/LCD/stations/WBAN:03177/detail). The ΔpCO_2 is the difference between the measured atmospheric pCO_2 (2018) and an average atmospheric pCO_2 of 411 µatm for 2020 and pCO_2 calculated from pH and A_T(S) in CO2SYS. The sensitivity to atmospheric pCO_2

is very small compared to the uncertainty due to pH. A 0.05 pH error translates to a 60 µatm change in pCO_2, making the error in the ΔpCO_2 term completely dominated by errors in the pH sensor. Any error within a few µatm in our knowledge of atmospheric pCO_2 is not significant for the output of the WRM (see below). For the model (next section) the cumulative sum of the flux (F), in µmol kg^{-1} hr^{-1}, is calculated over the time period of each dataset and then subtracted from the derived DIC in µmol kg^{-1} to obtain a DIC value that is corrected for gas exchange. A comprehensive analysis of the errors in gas exchange estimates was not performed as it was determined that this term is a relatively small factor in the WRM's estimate of rates.

3.3.4. Weighted Regression Model

The weighted regression model (WRM) developed for riverine systems by Robert Hirsch (USGS) and modified for tidal systems by Marcus Beck (Tampa Bay Estuary Program) was used to filter out variability in DO and DIC due to tidal effects (Hirsch et al., 2010; Beck et al., 2015). The model code (written in R) was accessed on 05/20/2020 through the Github repository (https://github.com/fawda123/WtRegDO). Briefly, the WRM includes a series of functions that remove tidal influence (detide), estimate NEM, and evaluate metrics associated with performance criteria. The detiding function (Eq. 3.2) is a multiple linear regression of observed properties (DO or DIC) in time (t) and tidal height (H).

$$DO_{obs} = \beta_0 + \beta_1 t + \beta_2 H \quad (3.2a)$$

$$DIC_{obs} = \beta_3 + \beta_4 t + \beta_5 H \quad (3.2b)$$

See below for determination of β. The detided output is used to estimate daily NEM independently for DO (Caffrey, 2003) and DIC using Equations 3.3 and 3.4, respectively.

$$NEM_{DO} = P_{g\,(DO)} + R_{t(DO)} + F_{O2} \quad (3.3)$$

$$NEM_{DIC} = P_{g(DIC)} + R_{t(DIC)} + F_{CO2} \quad (3.4)$$

Total respiration (R_t), is calculated as the average nighttime rate of change for DO or DIC during night hours, multiplied by 24. Gross production (P_g) represents the bulk biologically driven change in DO or DIC during the day. The F term represents air-sea gas exchange. O_2 gas exchange is handled within the WRM as originally written by Beck et al., (2015). The O_2 gas flux is computed from the difference between the DO at saturation (calculated as a function of temperature and salinity) and the observed value, multiplied by a volumetric reaeration coefficient, k_a (Beck et al., 2015).

Because the original version of the model was developed for DO only, several minor modifications were necessary in order to process the DIC time series. The primary change was to simply omit the gas exchange portion of the code during a DIC run and feed the model with the CO_2 gas exchange–corrected DIC, applied outside of the model (see above). Some additional unit changes were made to the model for the purpose of running DIC, including conversion of initial input of DIC to mmol m^{-3} and several DO-specific unit conversions were omitted. To compare the two NEM values, NEM_{DO} was converted to carbon units using the canonical Redfield ratio of -106 C:138 O_2. Using this convention, P_g in C units is negative and a negative NEM represents net autotrophy; and R_t in C units is positive, corresponding to net heterotrophy.

The WRM applies adjustable half-window width settings (day, hour of day, tide height) to tune the model by adjusting each of the β variables as a function of time. The window widths are applied to time series data to achieve gradual weighting from the center of the window over a specified range where values that fall outside of this range are given a weight of zero. Beck et al. (2015) extensively tested the WRM by using it to extract NEM from a simulated control case with various random and systematic sources of error. For a thorough discussion of these results including uncertainty analysis and comparison of NEM derived from detided vs unfiltered time series, please refer to Beck et al. (2015).

3.4. Results

3.4.1. Model Tuning

In tuning the WRM, we followed the approach as prescribed by Beck et al., which involved using a span of five different widths for each of the three half-window width settings (day, hour, and tidal height) resulting in a total of 125 unique combinations of window width settings (we used the exact same 125 combinations outlined in Beck et al., pg 739). The tuned model is then considered to be the case out of the 125 which results in the optimal set of performance metrics provided in the summary statistics function of the model and outlined as follows. The first metric includes the correlations for DO_{obs}, P_g, and R_t, which should decrease after filtering. Standard deviation for P_g and R_t is the second metric, which should also show a maximum decrease in the filtered output. The final metric is the percent of anomalous results, which is defined as the percentage of points in the timeseries with a negative P_g or positive R_t (for DO units). This percentage should be maximally reduced and ideally would be zero after detiding. The goal in tuning the model was to find the combination of weights where all three criteria were met. It was not possible to find maximal reductions for each of the three metrics for any given combination of weight settings; therefore, a combination in which all three metrics were reduced in comparison to the unfiltered data was considered the optimal result for the 2018 and 2020 datasets (Table 3.1). There is one additional metric described in Beck (2015) using the annual mean for P_g and R_t, which was not applied to the AHL datasets due to the shorter timeseries used. A sensitivity test was performed to determine potential error in the WRM NEM output by introducing the associated sensor errors of 0.05 unit for pH and 2 mmol m^{-3} for DO. This resulted in no change for NEM_{DO} and a 0.2% error for NEM_{DIC}. An additional test for A_T was performed where an error of 10 µmol kg^{-1} was introduced, this also yielded a 0.2% error in NEM_{DIC}. The insensitivity of the WRM to systematic errors (representing sensor accuracy error) is not surprising, as the model depends on short term changes in pH and DO, both of which are retained quite accurately even when pH and DO sensors may be slightly out of calibration.

3.4.2. Field Observations

In Figure 3.3 we compare baseline conditions of 2018 (panels A-E) to the anomalous red tide conditions observed during 2020 (panels F-J). The two-month period from Nov-Dec 2018 was selected

because it covers both dry and wet (rain) conditions. Temperature during both 2018 and 2020 ranged between 14°C and 20°C, although, due to the difference in time of year observed, the lagoon was cooling and heating during the 2018 and 2020 datasets, respectively. In the absence of rain, salinity remains very close to 33.8 PSU during both years. Depending on duration and intensity, rain events can drive salinity down by several units, such as during a strong storm in 2020 when salinity briefly fell below 30. Following a rain event, salinity fully recovers in roughly one week, reflecting the average residence time of the entire AHL. During long periods without rain, the inner reaches of the lagoon trend toward slightly hypersaline relative to the surrounding ocean salinity of 33.6 (i.e., behaving as an inverse estuary). Average pressure (Figure 3.3, C, H) reflects a difference of several meters between deployment locations in 2018 and 2020, with the latter deployment at a shallower depth of ~5m. It appears that in 2020 the pressure sensor became obstructed in mid-March around the time of a rain event but resumed regular operation by April 1. The rainfall in 2020 was more intense than that observed in 2018, with measured rainfall rates occasionally reaching close to 1 cm hr^{-1} (Figure 3.3, B and G).

Biogeochemical observations (Figure 3.3 D, E, I, J) show nominal conditions of pH and DO in late 2018 (D, E) and early 2020 (I, J) where pH ranges between 7.9 and 8.1 and DO ranges from 212 to 262.5 mmol m^{-3} with O_2 % saturation ranging from 87 to 110. These ranges typify the lagoon as slightly lower in both pH and DO than the adjacent surface ocean (Shipley 2022), as expected in a nearly balanced but, on average, net heterotrophic system. Following intense rain events in March and April 2020, the observed range of both pH and DO increase dramatically with pH reaching a maximum of 8.5 and a minimum of 6.9 in May. In connection with these extreme pH conditions, DO climbed as high as 517 mmol m^{-3}, which corresponds to a % saturation of about 225 and fell to zero (anoxic) on several days (Figure 3.3).

3.4.2. Model Output

In Figure 3.4, panels A-D show the 2018 and 2020 estimated rates for P_g, R_t, and NEM. Panels A and C show DO output for each period, and B and D show the DIC results. The average values for each rate are listed in Table 3.2 (with 2020 divided into phases as discussed below), where 2018 DO and DIC

averages for P_g (-150 and -144) and R_t (156 and 158) are quite similar although, NEM_{DIC} is almost double the average of NEM_{DO} during that time. The 2020 plots in C and D show a much larger range due to the red tide event. Comparing Phase-I 2020 conditions to 2018, P_g and R_t are somewhat smaller in magnitude in Phase I and NEM for Phase-I appears to be in a net autotrophic state.

The 2018 model output for DO and DIC is shown in Figure 3.5. As seen in panel A and B, detiding removes both high and low spikes associated with tidal mixing, resulting in an overall reduction in diel amplitude, sometimes of greater than 50%. It is noteworthy that the detiding step does not remove variability on timescales longer than 24 hours. Implications of this preservation of low-frequency variability are addressed in the discussion. NEM for DO and DIC generally run at a positive value with day-to-day changes (Figure 3.5C), which reflect conditions typical of a coastal lagoon where factors such as precipitation, sunlight, and spring and neap tide introduce variability. All daily NEM estimates fall within reasonable bounds, making it difficult to assign outliers resulting from model noise (e.g., insufficient removal of tides). However, it is warranted to question the validity of spikes or abrupt shifts of NEM between adjacent days. Accordingly, to address noise in model NEM, a 6-day low-pass filter (LPF) was used to generate a smoothed time series (Figure 3.5C and Figure 3.6C). The NEM LPF is also helpful in defining the four phases discussed below for the 2020 data. On average, NEM_{DO} in Nov-Dec 2018 was 6.75 ± 9 mmol C m^{-2} d^{-1} and NEM_{DIC} was 14 ± 11 mmol C m^{-2} d^{-1}. Although the NEM_{DIC} average is twice that of NEM_{DO}, the two-month mean (or integrated daily) NEM is not statistically different between NEM_{DO} and NEM_{DIC} and the daily and low-pass filtered (LPF) time series are in good agreement (Figure 3.5C).

The early portion of the 2020 time series (Figure 3.6, Phase-I) is quite similar to the "baseline" conditions observed during 2018 with a net autotrophic Phase-I NEM_{DO} average of -6.6 ± 9.6 and an NEM_{DIC} average of -8 ± 16.1 mmol C m^{-2} d^{-1}. Somewhat problematic is that variability in daily NEM is large relative to the mean, even under baseline conditions in both years, leading to mean NEM values that are statistically indistinguishable from zero. The question arises of whether or not late 2018 could be considered slightly net heterotrophic and Phase-I 2020 slightly net autotrophic as we have stated above.

Regardless of the trophic labeling of these time periods, the result of the model is that both periods appear to be operating in a near steady state of balanced NEM.

The massive red tide which developed during the spring of 2020 along hundreds of miles of coastline began influencing the AHL around mid-April. We defined the bloom onset (corresponding to the transition between Phase-I and II) as the point where both NEM LPF lines have inflected toward net autotrophy. Phase-II culminates in a period of bloom termination and "hyperventilation" (Beck and Bruland, 2000), characterized by pronounced daily amplitude in both DO and DIC. Phase-III, defined as the point when NEM LPF values from both DO and DIC exceed the largest rates observed under baseline conditions (~50 mmol C m^{-2} d^{-1}), represents bloom demise and abnormally high respiration rate, ending in a weeklong period of sustained hypoxia (DO ranging between 0-100 and on average 49 mmol m^{-3}) and sporadic, limited anoxia. Phase-IV, defined by the re-emergence of sustained presence of oxygen represents a weeks-long recovery and return to baseline conditions. Similar to 2018, detiding reduces daily extreme values, while retaining the lower frequency shift to a very low average DO (<100 mmol m^{-3}) and higher average DIC (>2300 mmol m^{-3}) during the peak conditions of Phase-III. Within one month of anoxic conditions, DO and DIC had fully recovered back to baseline conditions (note that, due to temperature change between Phase-I and -IV, DO recovery is slightly lower, but O_2% saturation (Figure 3J) recovers back to 100%.

3.5. Discussion

In general, detided results are devoid of the occasional spikes and steps observed during Phase-I in both DO and DIC (Figure 3.6). As noted by Beck et. al., (2015), suboptimal conditions for estimating NEM with the WRM include high correlation between sun angle and tide, and (surprisingly) decreased magnitude of the advection signal. In our data, the sun angle to tidal correlation was verified to be within the acceptable range for both time series, albeit, closer to the acceptable limit within ±0.2 in 2018. There may also be true metabolic variability as a result of tides (Nidzieko et al., 2014) which the WRM might incidentally remove. Moreover, tidal stage is an imperfect proxy for advection. The effect of advection or,

rather, gradients in general, is more difficult to assess. In their error analysis using simulated data, Beck et al. treat advection as a tidal term, linked to tide height, which is almost certainly the primary driver of signals associated with gradients. However, signals associated with phenomena such as diffusion, internal tides, and intake by the power plant in 2018 or desalination plant in 2020 may escape the detiding process of the WRM. In regard to this, perhaps most noteworthy are two periods during 2020 (April 26-28 and May 22-25) where NEM_{DIC} significantly overshoots NEM_{DO} in the negative (net autotrophic) direction (Figure 3.6 C). Assuming no massive shift in C:O stoichiometry during these two oxygenated periods, the most likely source of the discrepancy is a physical process that escapes detiding. Around both anomalies, the unfiltered DIC and DO (black line, Figure 3.6 A, B) both exhibit pronounced, low amplitude (> daily) variability, however, the detided DIC (blue line Figure 3.6 B) retains a greater slope (particularly in late April). While this subtle retention of low amplitude structure may be the source of discrepancy between NEM_{DO} and NEM_{DIC} at times, we do not believe that it explains the difference observed during peak respiration of Phase-III, when NEM_{DIC} overshoots NEM_{DO} in the positive (net heterotrophic) direction to extreme values.

Performance of the WRM under differing conditions is captured in 7-day snapshots of three different periods (Figure 3.7, Figure 3.8, Figure 3.9). Both 2018 (Figure 3.7) and 2020 Phase-1 (Figure 3.8) demonstrate the remarkable capability of the WRM to isolate the biological signal. In both cases, detided DO and DIC are in phase with the day/night cycle (shown in vertical bars) as expected. Figure 3.9 and Figure 3.4C, D show the one anomalous period (inverted Pg or Rt, as defined above) during the hypoxic event in mid-May 2020. During this period, the tidal signal is observed in the detided time series, and, as discussed next, leads to questionable results.

One of the most intriguing and perplexing features of the 2020 time series is a marked difference between the NEM_{DO} and NEM_{DIC} during Phase-III (Figure 3.6C), indicating a DIC respiration signal much stronger than that of DO. Peak NEM_{DIC} reaches 140 mmol C m^{-2} d^{-1} compared to a peak of around 50 mmol C m^{-2} d^{-1} for DO. A somewhat independent check was performed to verify the approximate magnitude of the daily NEM rates generated by the model (Figure 3.10A, B). This approach involves

applying a simple regression to arbitrarily selected multi-day periods of the detided DIC time series. The difference between the multi-day regression and the model output daily NEM therefore fundamentally lies in the difference between high frequency (daily period, peak-trough diel cycles) and low frequency (trend over multiple days) in the detided data. In theory, if detiding is perfectly efficient and NEM is a constant value, then a linear trend over multiple days will exactly match that obtained from the model's peak-to-trough calculation of daily NEM. Of course, neither of these conditions holds true in practice, but as seen in Figure 3.10, the four trendlines corresponding to Phases I-IV are in reasonably good agreement with the daily NEM output of the model. The trendline check was only performed for NEM_{DIC} because the filtered (detided) DIC is already corrected for gas exchange (in the modified version we fed the model gas exchange corrected DIC), whereas, the original model, as designed for DO, performs a gas exchange correction internally and does not supply a gas exchange corrected detided DO value in the output file. In summary, the leap of faith required to evaluate Phase-III data shown in Figure 3.6C is that one must trust the average (LPF) output even though it is clear that daily NEM contains additional noise due to the tidal signal making it through the filtering process during the week of extreme conditions. While our results are not 100% efficient, the detiding efforts may offer some improvement to the more commonly used methods for assessing estuarine trophic status (Odum, 1956; Caffrey, 2003), which do not account for tidal influences. If the model noise over multiple days is random, then some of the underlying trend in the detided data will still influence the daily calculated P_g, R_t, and NEM. In this case, the LPF value still reflects the correct number as it averages over the 6 days.

If the differences in Phase-III between LPF NEM_{DIC} and NEM_{DO} reflect a real signal, what process is responsible? The simple observation that average pH continues to decrease during the hypoxic portion of Phase-III (Figure 3.3 I, J), suggests that oxic respiration remained the dominant process. In order to visualize the multiple processes that may be present, we present Figure 3.11 to illustrate the effect of selected oxic and anoxic reactions in pH-DO space. The vector origins for each condition (oxic, anoxic) are somewhat arbitrary. For example, the symbol representing oxic conditions at pH = 8, DO = 200 along with the four vectors representing photosynthesis, respiration, calcification, and calcite

dissolution could be located anywhere in the range of observed data where DO > 0. Similarly, the anoxic condition could be selected over a wide range of pH where DO = 0 (note the anoxic vectors in Figure 3.11 are offset from zero DO for clarity). Important features of Figure 3.11 include: 1) a clockwise hysteretic cycle from Phase I through IV; 2) a primary signal due to P-R along with, perhaps, a secondary signal due to either mixing or $CaCO_3$ reactions seen most clearly in Phase I and II as a decrease in slope of the subset; 3) a wide range of pH under near-zero oxygen concentrations.

In regard to the final feature of Figure 3.11, if, for example, denitrification became significant, the A_T increase relative to DIC increase associated with the reaction

$$5(CH_2O)_{106}(NH_3)_{16}(H_3PO_4)_1 + 4(106)NO_3^- \rightarrow$$
$$106CO_2 + 3(106)H_2O + 4(106)HCO_3^- + 2(106)N_2 + 5(16)NH_3 + 5(1)H_3PO_4$$

would be 0.96 rather than the Redfieldian 0.16 (Tromp et al., 1995). Thus, under denitrification in a closed system, ΔDIC:ΔTA is close to 1 resulting in a near-zero pH change, counter to what we observe in Figure 3.3 I and J during Phase-III. Under similar conditions, in the case of sulfate reduction, following the reaction (Tromp et al., 1995),

$$2(CH_2O)_{106}(NH_3)_{16}(H_3PO_4)_1 + 106SO_4^{2-} \rightarrow$$
$$106H_2S + 2(106)HCO_3^- + 2(16)NH_3 + 2(1)H_3PO_4$$

the pH shows an overall increase, which is the opposite of what we observe during Phase-III where pH continues to decrease. Additionally, sulfide (pyrite) precipitation and oxidation reactions (Łukawska-Matuszewska and Graca, 2018)

$$Fe^{2+} + H_2S + S \rightarrow FeS_2 + 2H^+ \text{ (precipitation)}$$

$$HS^- + 2O_2 \rightarrow SO_4^{2-} + 2H^+ \text{ (oxidation)}$$

show that, during these processes, A_T can decrease resulting in a drop in pH. In a closed system, sulfide formation followed by precipitation or oxidation will balance, resulting in no changes in A_T or pH. However, if decoupling occurs when sulfide is formed vs. consumed, this will result in a pH change. In Figure 3.11, the sulfide arrow is shown in the direction of decreasing pH, which could occur from a pulse of sulfide from the upper lagoon or an imbalance in sediment flux. While it is difficult to determine the exact processes responsible for decoupling during the hypoxic/anoxic period in 2020, it is possible that part of the continued decrease in pH was driven by imbalances in the sulfur cycle within the AHL.

We hypothesize that, although several brief (1-6 hr) anoxic periods occurred (Figure 3.9), oxygen remained in sufficient supply (in part through gas exchange) to fuel continued respiration of the terminating bloom. To represent this process, we include an additional vector in Figure 3.11 for cryptic oxygen consumption (Garcia-Robledo et al., 2017) in the direction of negative pH. This vector represents a system poised at near-zero oxygen where oxygen supplied (in this case through gas exchange rather than photosynthesis as proposed for Anoxic Marine Zone (AMZ) systems by Garcia-Robledo et al., (2017) is immediately consumed with little or no accumulation, driving pH lower through normal oxic respiration channels.

Average rates for P_g, R_t, and NEM are reported in Table 3.2, along with ranges from a compilation of US estuaries (Caffrey, 2003; Caffrey, 2004) for comparison. Caffrey's NEM compilation (Table 3.2 in Caffrey, 2004) for US estuaries ranges from -21 to 180 mmol C m^{-2} d^{-1}, with an average of 55 mmol C m^{-2} d^{-1} (g O_2 reported by Caffrey is converted to mmol C using -106 C:138 O_2 and 32 g/mol O_2). Recent estimates of the regional averages for the US East coast fall between 5.5 and 20 mmol C m^{-2} d^{-1} (Najjar et al., 2018). These estimates are in line with our findings for the AHL, where we observed a range of short-term NEM of -50 to 150 mmol C m^{-2} d^{-1} and baseline averages of -8 to 14 mmol C m^{-2} d^{-1}. The P_g and R_t time series (Figure 3.4 A-D) generally fall within the ranges for US estuaries. The 2018 P_g and R_t rates for DO at the AHL (Figure 3.4 A, B) fall within the lower half of the range reported by

Caffrey (2004) with P_g ranging from -62 to -236 mmol C m^{-2} d^{-1} and R_t rates from about 60 to 243 mmol C m^{-2} d^{-1}. We see the P_g and R_t rates reaching the extremes reported by Caffrey (2004) during Phase-II of the 2020 red tide. Perhaps the most noteworthy feature across Table 3.2 (and Figure 3.4 and Figure 3.6) is that the most extreme P_g and R_t occur during Phase-II while the most extreme NEM occurs during Phase-III. This apparent decoupling between gross and net rates is not a widely reported observation, likely due to the requirement of continuous observations to derive the rate terms.

3.6. Conclusions

Applying an open source WRM to observations before, during, and after a red tide event provides insight on the temporal progression of metabolic rates in a tidal estuary. While physical forcing through tidal advection is a major driver of variability in the lagoon, the WRM successfully isolated the local biological signal and quantified metabolic rates that drove the lagoon into a state of hypoxia. Baseline NEM established for 2018 and Phase-I of 2020 are in line with estimates from other estuaries (Caffrey, 2003; Caffrey, 2004; Najjar et al., 2018), providing some confidence in the rates determined by the same model under extreme conditions in 2020. The wide range of pH observed near zero DO suggests that anoxic reactions related to sulfur may have occurred. The low pH signal expected for denitrification makes it impossible to state whether or not this process occurred based solely on pH and DO data. However, it can be stated that processes other than denitrification were at work during the anoxic period since denitrification alone cannot explain the pH variability. In addition to the sulfur cycle decoupling, we hypothesize that there may have been a brief occurrence of a cryptic oxygen cycle similar to those discovered recently in AMZs (Garcia-Robledo et al., 2017). As an opportunistic and unplanned study of hypoxia, the suite of measurements employed was limited for studying anoxic reactions. As such we would recommend that any future study planned expressly for this purpose should include, at minimum, an autonomous nitrate sensor (e.g., Sea-Bird SUNA) alongside the pH and DO sensors.

The WRM was shown to be a useful tool that required minimal inputs to obtain NEM estimates for both baseline and extreme conditions in a coastal ocean setting. The production and respiration rates estimated in the model show the occurrence of anomalous periods, which are likely a result of the WRM

not being able to completely filter out tidal signals under extreme conditions (particularly for DO near anoxia), stratification, or significant calcification (in the case of DIC as a model input). Though beyond the scope of this work, a multi-box model of the AHL, including features of the lagoon such as sediments and aquaculture, would be a useful tool to further investigate the rise in DIC (decrease in pH) during the hypoxic period. Such a model could also demonstrate the influence of the desalination plant on residence time and differences in residence time between DO and DIC that may lead to the decoupling observed in Phase-III.

Given some of the concerns mentioned above, one alternative approach is to estimate NEM from trendlines (or secants, finite differences, etc.) in the detided time series over multiple days to weeks of LPF detided data rather than attempting to pull out meaningful results from short peak to trough diel signals. An additional approach to interpret the data more efficiently and possibly yield better NEM estimates would be to focus on specific time periods in the data that exhibit the lowest sun angle correlation or when the correlation is zero as suggested in Beck (2015). In summary, we found the WRM and the novelty of the DIC addition to be a great resource and hope that our contributions outlined here may encourage others to explore similar uses of this tool.

3.7. Acknowledgements

The authors would like to thank Thomas Grimm and the Carlsbad Aquafarm for providing small boat access to the Lagoon and Matt Steinke who helped with boat operations. We also thank Vicky Rowley from SCCOOS for assistance with the real-time data portal.

Chapter 3, in full has been submitted for publication as: Shipley, K., Martz, T., Bresnahan, P., and Wirth, T. (2022) Metabolic Rates in the Agua Hedionda Lagoon during a Southern California red tide event. *Elementa*. The dissertation author was the primary investigator and first author of this paper.

3.8. Tables and Figures

Table 3.1. Performance metrics (correlation and anomaly) of model output, determined as the optimal set of Weight Settings from 125 model runs. The final weight settings were chosen based on the significant reduction in all or most of the correlation and anomaly parameters listed, when compared to observed correlation and anomaly data.

	Weight ($\beta_{0...5}$)	**Correlation**			**Anomaly (%)**	
Model	**Day, hour, tidal height**	**P_g corr**	**R_t corr**	**DO corr**	**Anom P_g**	**Anom R_t**
2018 DO	9, 6, 0.4	0.42	0.29	-0.22	0	0
2018 DIC	9, 6, 0.4	-0.29	-0.18	0.21	0	0
2020 DO	12, 3, 0.6	-0.01	-0.09	-0.07	3.9	3.9
2020 DIC	9, 6, 0.4	-0.19	-0.02	0.05	28	29

Table 3.2. Summary of metabolic rates, reported as average (±1σ) over period indicated. NEM_{DIC} from slopes in Figure 3.10 are also included for 2020.

Data period	**P_g mmol C m^{-2} d^{-1}**	**R_t mmol C m^{-2} d^{-1}**	**NEM mmol C m^{-2} d^{-1}**
AHL 2018 Nov-Dec	$P_{g\text{-}DO}$: -150 $P_{g\text{-}DIC}$: -144	$R_{r\text{-}DO}$: 156 $R_{t\text{-}DIC}$: 158	NEM_{DO}: 6.75 ± 9 NEM_{DIC}: 14 ± 11
AHL 2020 Phase I	$P_{g\text{-}DO}$: -123.8 $P_{g\text{-}DIC}$: -90.6	$R_{r\text{-}DO}$: 117.2 $R_{t\text{-}DIC}$: 82.7	NEM_{DO}: -6.6 ± 9.6 NEM_{DIC}: -8 ± 16 $NEM_{DIC\text{-}Slope}$: -13
AHL 2020 Phase II	$P_{g\text{-}DO}$: -721.9 $P_{g\text{-}DIC}$: -688.4	$R_{r\text{-}DO}$: 732.9 $R_{t\text{-}DIC}$: 670.5	NEM_{DO}: 11 ± 27 NEM_{DIC}: -17.8 ± 42 $NEM_{DIC\text{-}Slope}$: -67
AHL 2020 Phase III	$P_{g\text{-}DO}$: -112.8 $P_{g\text{-}DIC}$: -78.4	$R_{r\text{-}DO}$: 152.8 $R_{t\text{-}DIC}$: 166.4	NEM_{DO}: 40 ± 27 NEM_{DIC}: 88 ± 40 $NEM_{DIC\text{-}Slope}$: 155
AHL 2020 Phase IV	$P_{g\text{-}DO}$: -126 $P_{g\text{-}DIC}$: -150	$R_{r\text{-}DO}$: 114 $R_{t\text{-}DIC}$: 119	NEM_{DO}: -12 ± 10 NEM_{DIC}: -31 ± 23 $NEM_{DIC\text{-}Slope}$: -30
US Estuaries Caffrey (2004)	-55 - -675	105 - 775	-21 - 180

Figure 3.1. Map of the AHL. Map shows the major features of the lagoon and sites of interest. The location of the mooring deployment for 2018 and 2020 in the outer basin is indicated by the red X. Image from Google Earth.

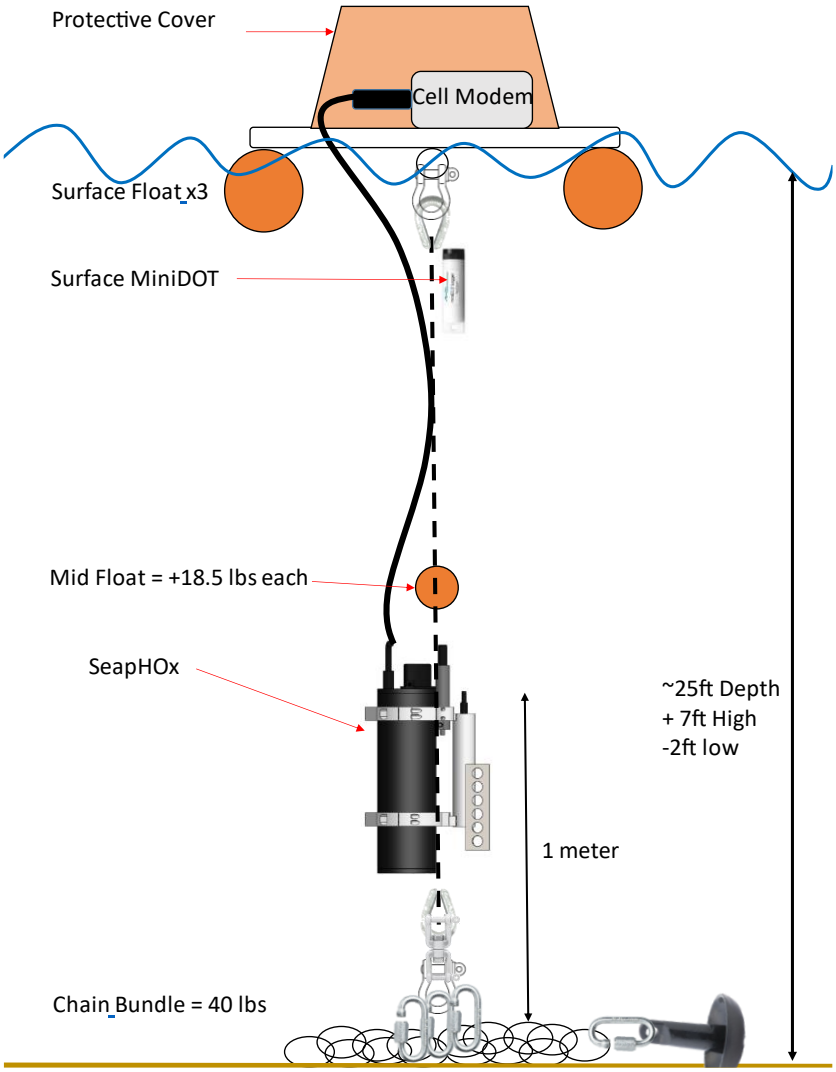

Figure 3.2. Schematic of the mooring design including hardware, sensors, and cellular modem used for real-time data acquisition.

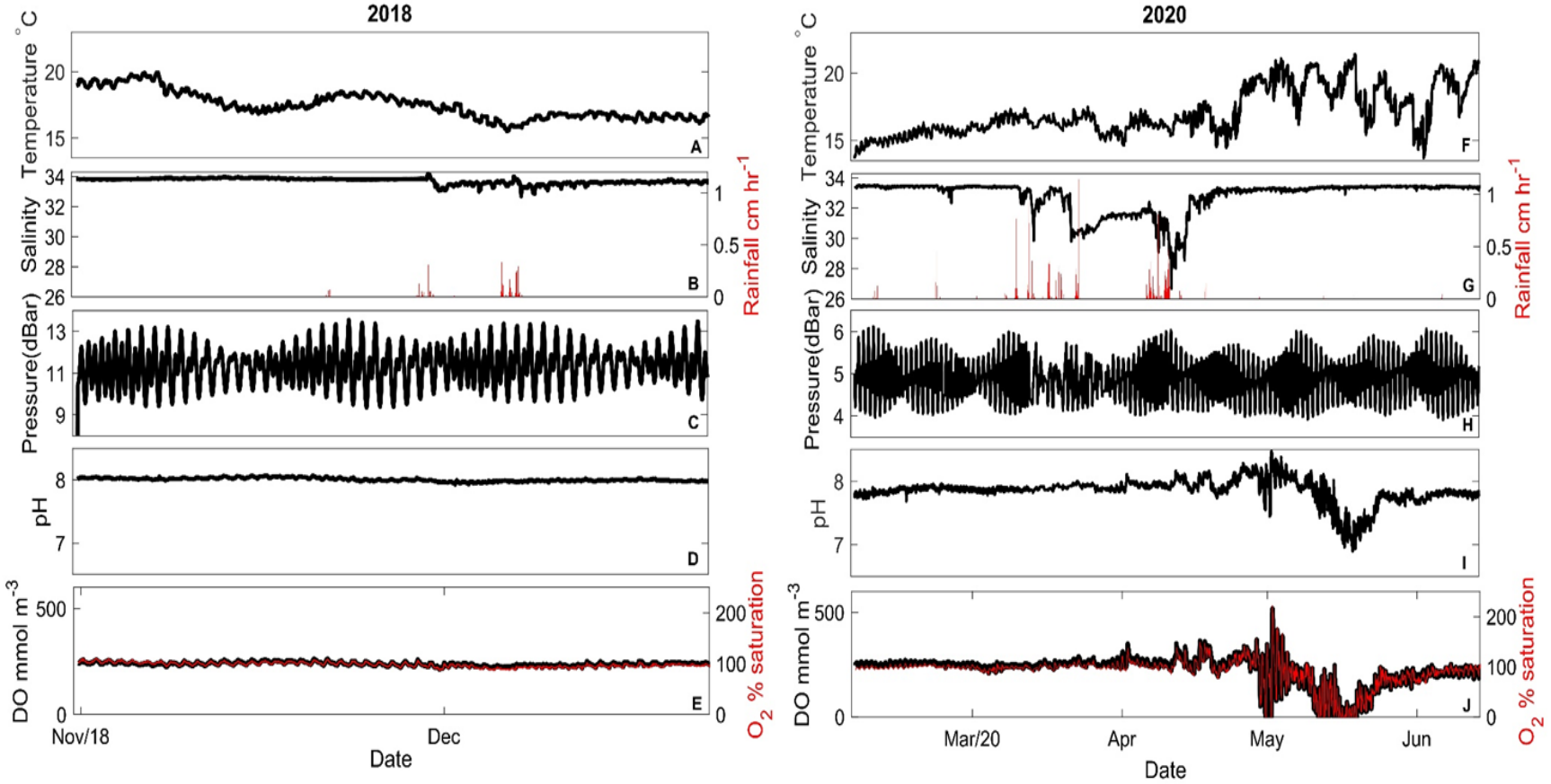

Figure 3.3. AHL outer basin time series for 2018 (left) and 2020 (right). All measured SeapHOx parameters are provided in panels A-E for 2018 and F-J for 2020. Both 2018 and 2020 rainfall data were obtained from the NOAA climatological data resource for their respective time periods, shown here in cm hr^{-1}. (Shipley et al., 2022).

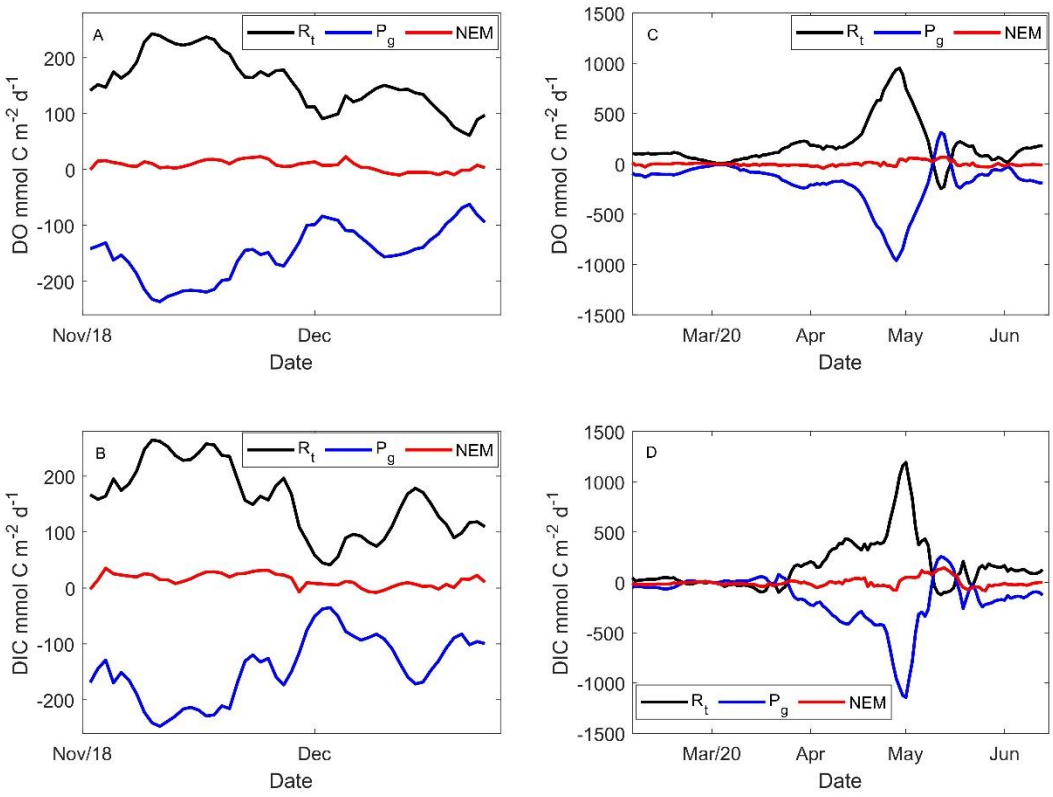

Figure 3.4. WRM output for Pg, Rt, and NEM for 2018 and 2020. Panels A, B show the 2018 output for DO and DIC respectively. Panels C, D are the DO and DIC output for 2020.

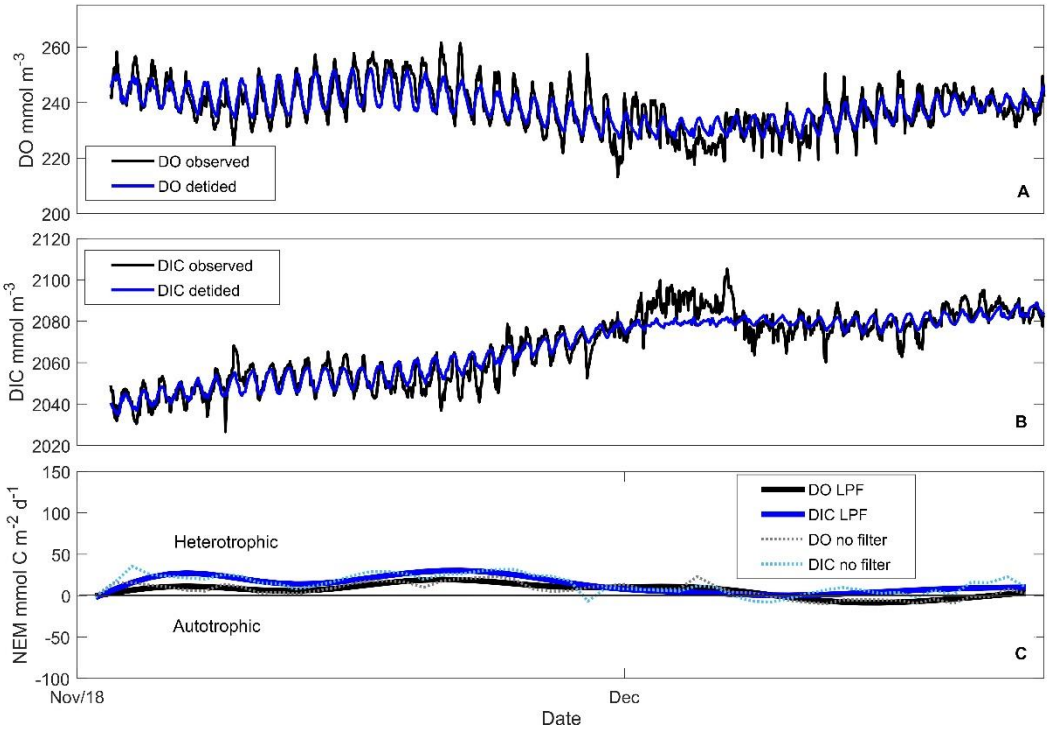

Figure 3.5. 2018 WRM output. Panels A and B provide the initial detiding results in blue along with the observed data in black for DO and DIC, respectively. Panel C includes NEM estimates for DO in C units and DIC after applying a 6 day, lowpass Butterworth filter function shown as solid lines and unfiltered NEM as dotted lines.

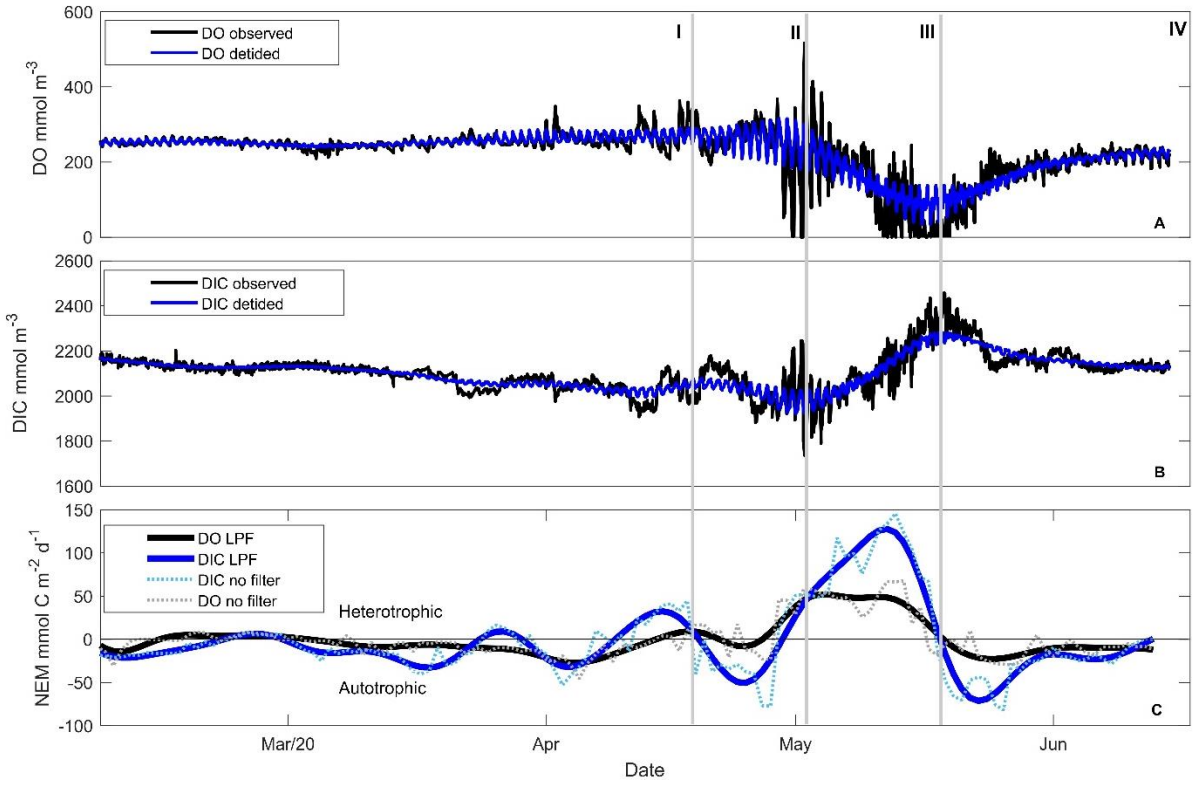

Figure 3.6. 2020 model output. Panel A) 2020 observed and detided DO, B) 2020 observed and detided DIC, C) NEM estimates for DO in C units and DIC after applying a 6 day, lowpass Butterworth filter function shown as solid lines and unfiltered NEM as dotted lines. Panel A and B provide detided results in blue and the original data used as model input in black. Phase I-IV represent the different periods of 2020, Phase I corresponds to baseline conditions, Phase II is the bloom onset, culminating in hyperventilation, Phase III is the bloom termination leading to hypoxic/anoxic conditions. Phase IV represents the post event recovery period characterized by reventilation and a return to near zero NEM.

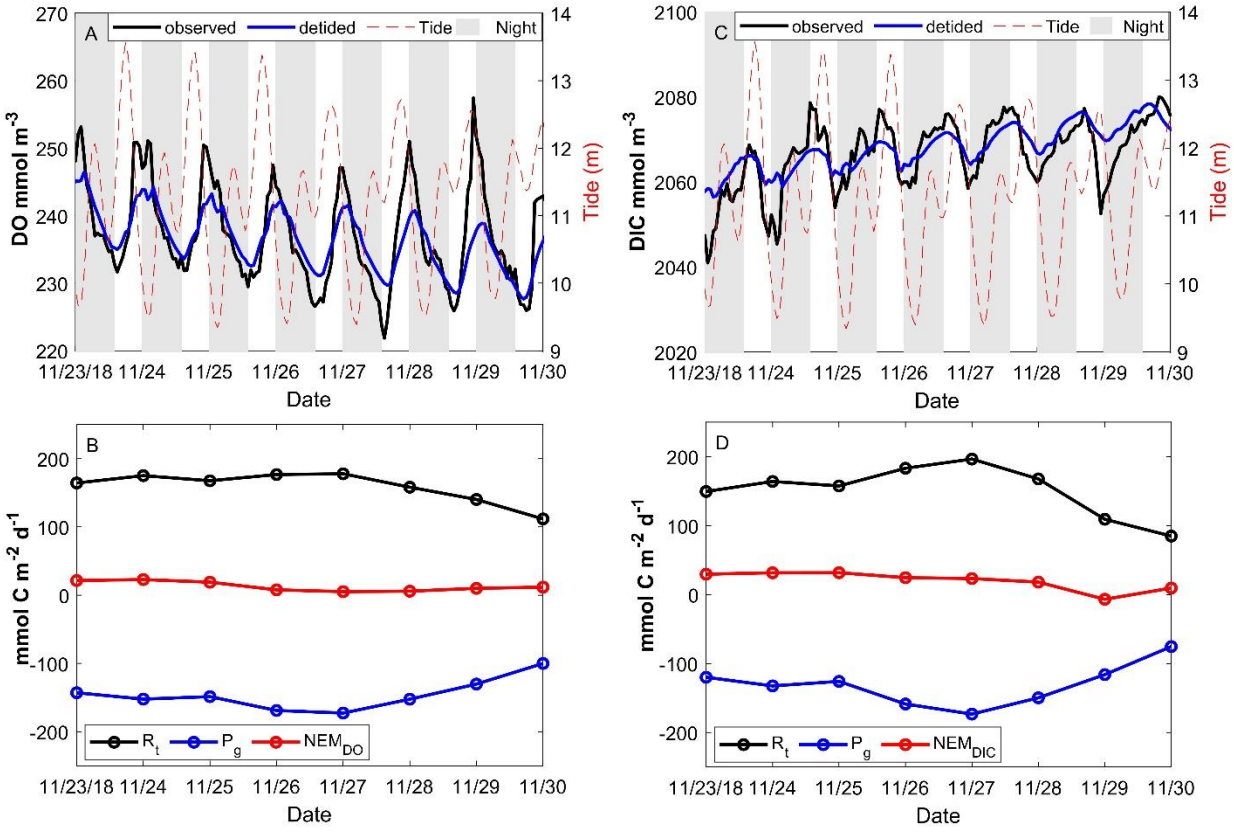

Figure 3.7. 2018 7-day snapshot of a normal period without anomalies. DO output in panels A, B and DIC in C, D. Panel A and C include the observed and detided data, the tide data in red, and grey shaded bars to represent night hours. Bottom panels B and D are the corresponding R_t, P_g, and NEM for the above panels.

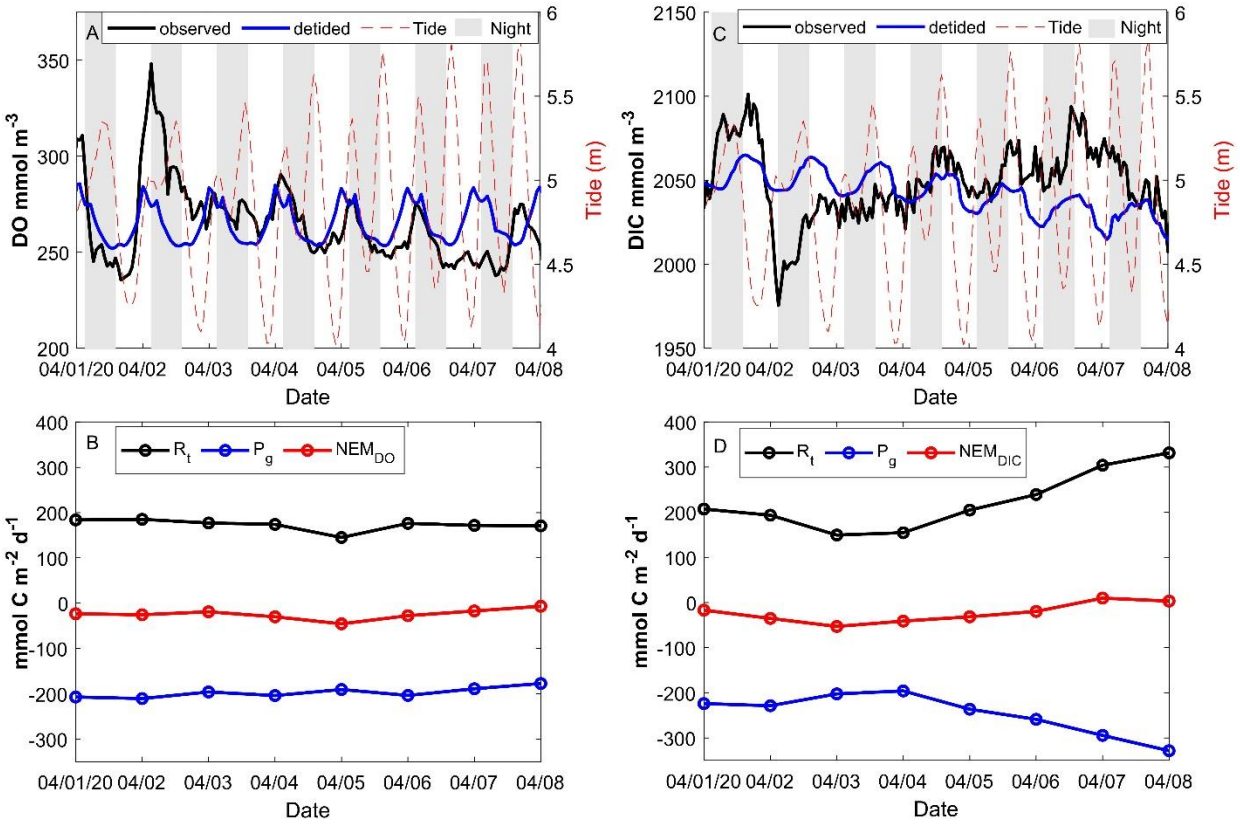

Figure 3.8. 2020 7-day snapshot of a period without anomalies. DO output in panels A, B and DIC in C, D. Panel A and C include the observed and detided data, the tide data in red, and grey shaded bars to represent night hours. Bottom panels B and D are the corresponding R_t, P_g, and NEM for the above panels.

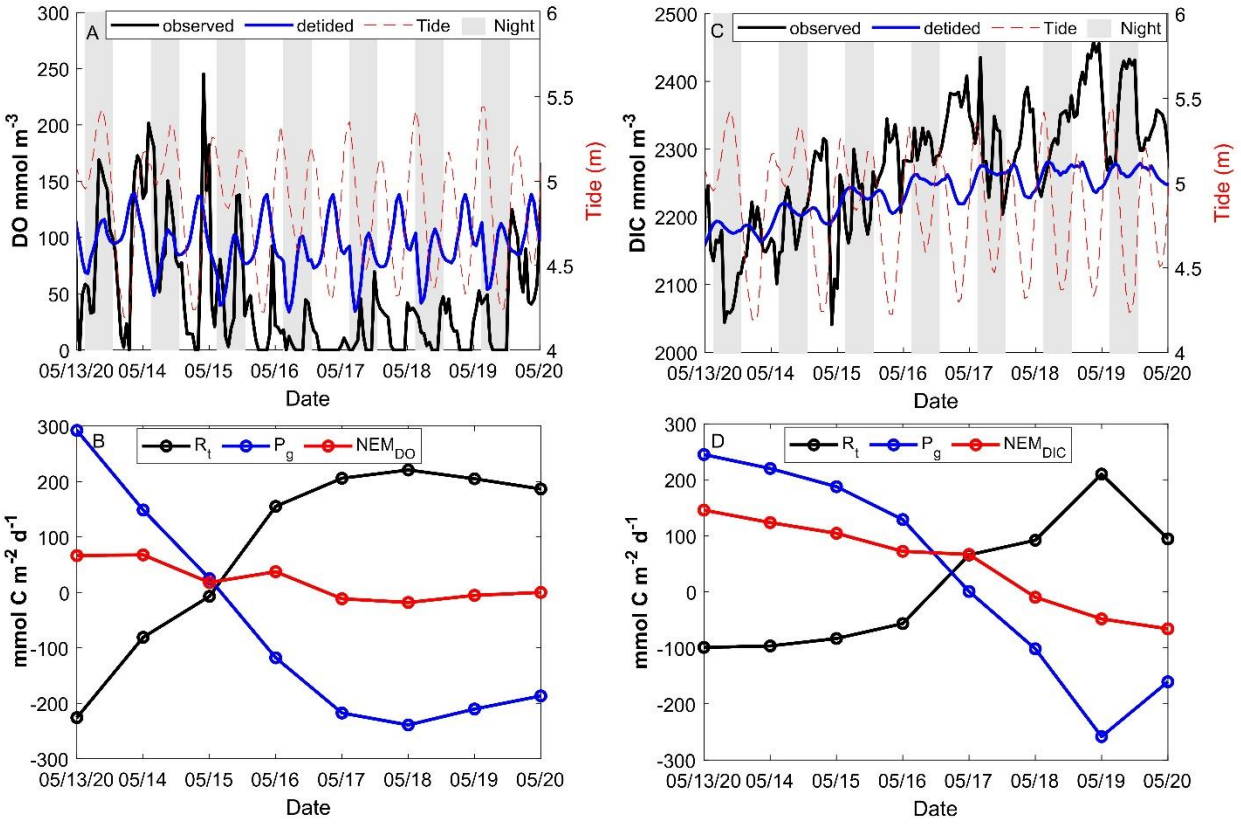

Figure 3.9. 2020 7-day snapshot of a period with anomalies. DO output in panels A, B and DIC in C, D. Panel A and C include the observed and detided data, the tide data in red, and grey shaded bars to represent night hours. Bottom panels B and D are the corresponding R_t, P_g, and NEM for the above panels.

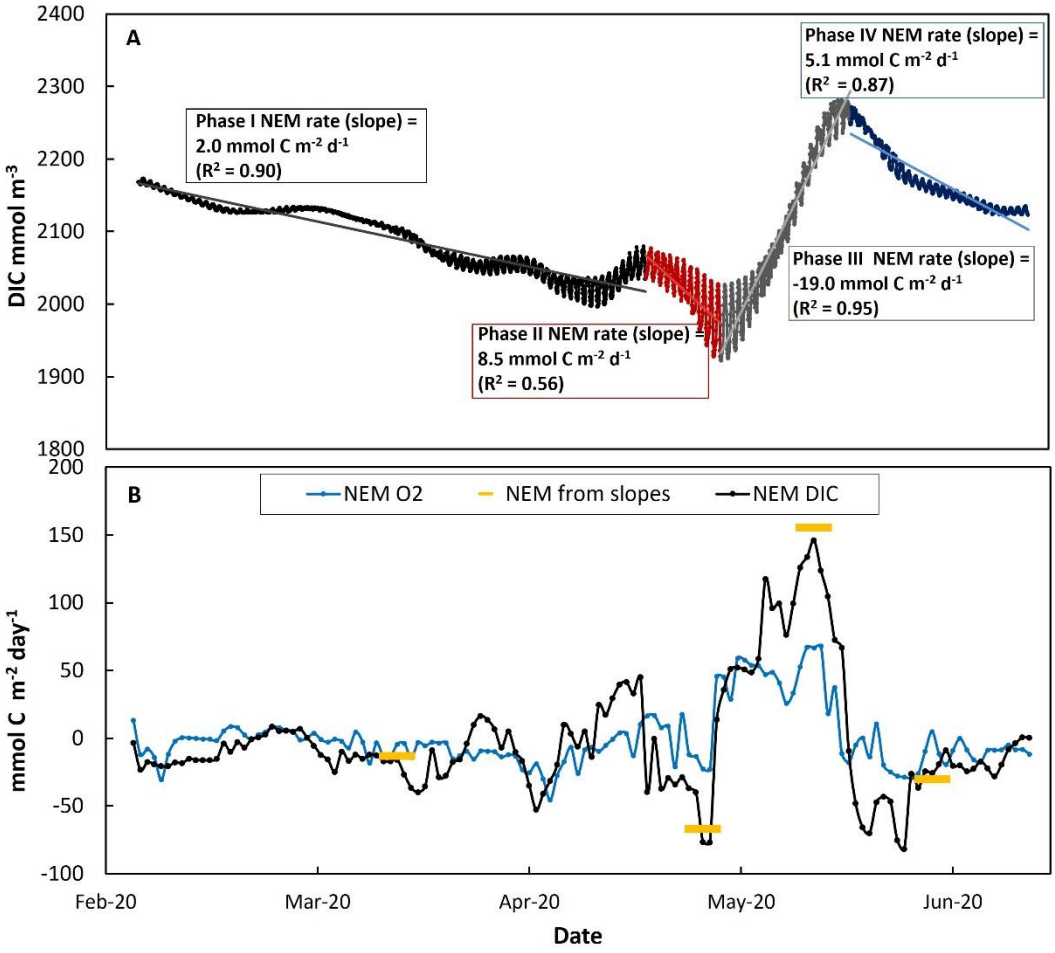

Figure 3.10. (A) 2020 detided DIC data including regression results for each phase as defined in Figure 3.6. (B) 2020 NEM daily rates (from Figure 3.6C) and slopes (yellow bars).

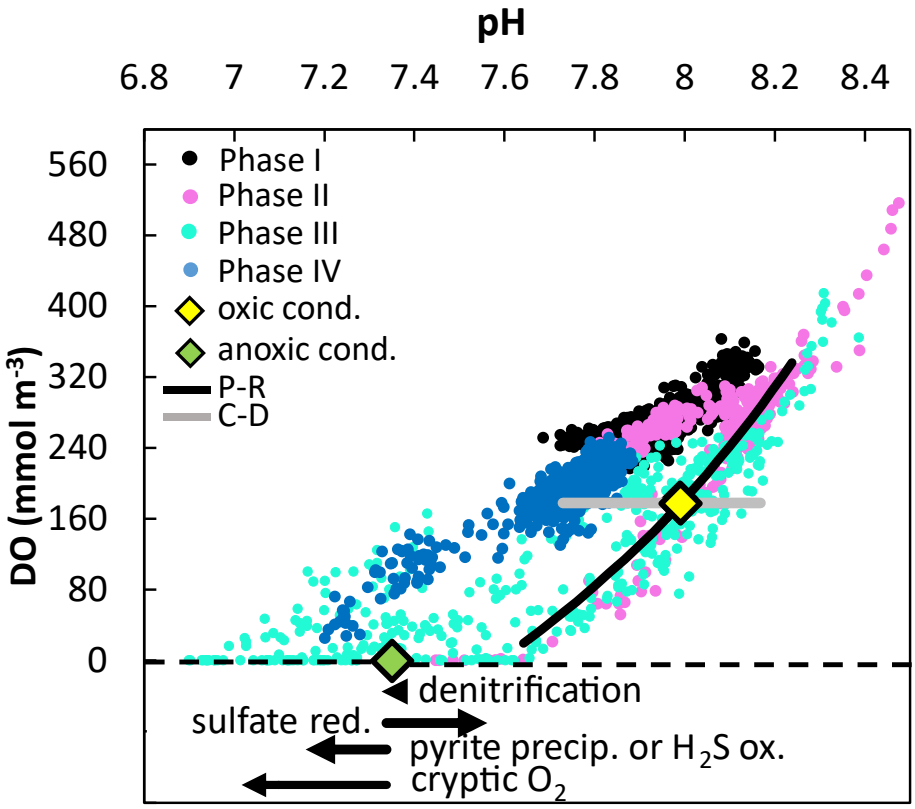

Figure 3.11. DO vs. pH during 2020 (data from Figure 3.3 I, J). Marker color denotes phase, as indicated in Figure 3.6. Line P-R represents photosynthesis and respiration effects under oxic conditions and line C-D shows the effects of calcium carbonate precipitation and dissolution. Anoxic processes shown at zero oxygen (arrows offset negative for clarity) include denitrification, sulfate reduction, sulfide consumption (by precipitation and/or oxidation) and cryptic O_2. P-R, denitrification, sulfate reduction and cryptic O_2 represent the effect of 1 µmol of organic matter and the length of the C-D vector represents ± 100 µmol $CaCO_3$. The sulfide precipitation or oxidation represents the effect of 10 µmol L^{-1}.

3.9. References

Anderson DJ, Cembella AD, Hallegraeff GM. 2012. Progress in understanding harmful algal blooms (HABs): Paradigm shifts and new technologies for research, monitoring and management. *Annual Review of Marine Science*(4): 143–176. doi: 10.1146/annurev-marine-120308-081121

Armstrong M, Kudela R. 2006. Evaluation of California isolates of Lingulodinium polyedrum for the production of yessotoxin. *African Journal of Marine Science* **28**(2): 399–401. doi: 10.2989/18142320609504186

Bauer JE, Cai W-J, Raymond PA, Bianchi TS, Hopkinson CS, Regnier PAG. 2013. The changing carbon cycle of the coastal ocean. *Nature* **504**(7478): 61–70. doi: 10.1038/nature12857

Beck MW, Hagy JD, Murrell MC. 2015. Improving estimates of ecosystem metabolism by reducing effects of tidal advection on dissolved oxygen time series. *Limnology and Oceanography: Methods* **13**(12): 731–745. doi: 10.1002/lom3.10062

Beck NG, Bruland KW. 2000. Diel Biogeochemical Cycling in a Hyperventilating Shallow Estuarine Environment. *Estuaries* **23**(2): 177–187. doi: 10.2307/1352825

Beller E, Baumgarten S, Grossinger R, Longcore T, Stein E, Dark S, Dusterhoff S. 2014. Northern San Diego County lagoons historical ecology investigation. San Francisco Estuary Institute Publication. Richmond. Available at http://www.sfei.org/documents/.

Breitburg DL, Hondorp DW, Davias LA, Diaz RJ. 2008. Hypoxia, nitrogen, and fisheries: Integrating effects across local and global landscapes. *Annual Review of Marine Science* **1**: 329–349. Annual Reviews. doi: 10.1146/annurev.marine.010908.163754

Bresnahan PJ, Martz TR, Takeshita Y, Johnson KS, LaShomb M. 2014. Best practices for autonomous measurement of seawater pH with the Honeywell Durafet. *Methods in Oceanography* **9**(October): 44–60. doi: 10.1016/j.mio.2014.08.003

Bresnahan PJ, Wirth T, Martz T, Shipley K, Rowley V, Anderson C, Grimm T. 2020. Equipping smart coasts with marine water quality IoT sensors. *Results in Engineering* **5**. Elsevier Ltd. doi: 10.1016/j.rineng.2019.100087

Caffrey JM. 2003. Production, respiration and net ecosystem metabolism in u.s. estuaries. *Environmental monitoring and assessment* **81**: 207–219.

Caffrey JM. 2004. Factors controlling net ecosystem metabolism in U.S. estuaries. *Estuaries* **27**(1): 90–101. doi: 10.1007/bf02803563

Conley DJ, Carstensen J, Vaquer-sunyer R, Duarte CM. 2009. Ecosystem threshholds with hypoxia. *Hydrobiologica* **629**. doi: 10.1007/978-90-481-3385-7

Dickson AG, Millero FJ. 1987. A comparison of the equilibrium constants for the dissociation of carbonic acid in seawater media. *Deep Sea Research Part A, Oceanographic Research Papers* **34**(10): 1733–1743. Elsevier. doi: 10.1016/0198-0149(87)90021-5

Elwany H, Flick R, White M. 2005. Agua Hedionda Lagoon hydrodynamic studies.

Garcia-Robledo E, Padilla CC, Aldunate M, Stewart FJ, Ulloa O, Paulmier A, Gregori G, Revsbech NP. 2017. Cryptic oxygen cycling in anoxic marine zones. *Proceedings of the National Academy of Sciences of the United States of America* **114**(31): 8319–8324. doi: 10.1073/pnas.1619844114

Gattuso JP, Frankignoulle M, Wollast R. 1998. Carbon and carbonate metabolism in coastal aquatic ecosystems. *Annual Review of Ecology and Systematics* **29**(1998): 405–434. doi: 10.1146/annurev.ecolsys.29.1.405

van Heuven S, Pierrot D, Rae JWB, Lewis E, Wallace DWR. 2011. MATLAB program developed for CO2 system calculations. Carbon dioxide information analysis center, Oak Ridge National Laboratory, U.S. Department of Energy, Oak Ridge, Tennessee.

Hewitt JE, Anderson MJ, Thrush SF. 2005. Assessing and monitoring ecological community health in marine systems. *Ecological Applications* **15**(3): 942–953. doi: 10.1890/04-0732

Hirsch RM, Moyer DL, Archfield SA. 2010. Weighted regressions on time, discharge, and season (WRTDS), with an application to Chesapeake Bay river inputs. *Journal of the American Water Resources Association* **46**(5). doi: 10.1111/j.1752-1688.2010.00482.x

Hopkinson CS, Vallino JJ. 1995. The relationships among man's activities in watersheds and estuaries: A model of runoff effects on patterns of estuarine community metabolism. *Estuaries* **18**(4): 598–621. doi: 10.2307/1352380

Horner RA, Garrison DL, Plumley FG. 1997. Harmful algal blooms and red tide problems on the U.S. west coast. *Limnology and Oceanography* **42**(5 II): 1076–1088. doi: 10.4319/lo.1997.42.5_part_2.1076

Howarth R, Chan F, Conley DJ, Garnier J, Doney SC, Marino R, Billen G. 2011. Coupled biogeochemical cycles: Eutrophication and hypoxia in temperate estuaries and coastal marine ecosystems. *Frontiers in Ecology and the Environment* **9**(1): 18–26. doi: 10.1890/100008

Jenkins S, Wasyl J. 2006. Coastal process effects of reduced intake flows at Agua Hedionda Lagoon.

Kahru M, Anderson C, Barton AD, Carter ML, Catlett D, Send U, Sosik HM, Weiss EL, Mitchell BG. 2021. Satellite detection of dinoflagellate blooms off California by UV reflectance ratios. *Elementa* **9**(1): 1–10. doi: 10.1525/elementa.2020.00157

Kapsenberg L, Bockmon EE, Bresnahan PJ, Kroeker KJ, Gattuso JP, Martz TR. 2017. Advancing ocean acidification biology using Durafet® pH electrodes. *Frontiers in Marine Science* **4**(321): 1–9. doi: 10.3389/fmars.2017.00321

Łukawska-Matuszewska K, Graca B. 2018. Pore water alkalinity below the permanent halocline in the Gdańsk Deep (Baltic Sea) - Concentration variability and benthic fluxes. *Marine Chemistry* **204**: 49–61. doi: 10.1016/j.marchem.2018.05.011

Najjar RG, Herrmann M, Alexander R, Boyer EW, Burdige DJ, Butman D, Cai WJ, Canuel EA, Chen RF, Friedrichs MAM, Feagin RA, Griffith PC, Hinson AL, Holmquist JR, Hu X, Kemp WM, Kroeger KD, Mannino A, McCallister SL et al. 2018. Carbon budget of tidal wetlands, estuaries, and shelf waters of Eastern North America. *Global Biogeochemical Cycles* **32**(3): 389–416. doi: 10.1002/2017gb005790

Nidzieko NJ, Needoba JA, Monismith SG, Johnson KS. 2014. Fortnightly Tidal Modulations Affect Net Community Production in a Mesotidal Estuary. *Estuaries and Coasts* **37**(S1): 91–110. Springer. doi: 10.1007/s12237-013-9765-2

Odum HT. 1956. Primary production in flowing waters. *Limnology and Oceanography* **1**(2): 102–117. doi: 10.4319/lo.1956.1.2.0102

Paerl HW, Valdes LM, Peierls BL, Adolf JE, Harding LW. 2006. Anthropogenic and climatic influences on the eutrophication of large estuarine ecosystems. *Limnology and Oceanography* **51**(1 II): 448–462. doi: 10.4319/lo.2006.51.1_part_2.0448

Paulsen M-L, Andersson AJ, Aluwihare L, Cyronak T, D'Angelo S, Davidson C, Elwany H, Giddings SN, Page HN, Porrachia M, Schroeter S. 2018. Temporal changes in seawater carbonate chemistry and carbon export from a Southern California estuary. *Estuaries and Coasts* **41**(4): 1050–1068. doi: 10.1007/s12237-017-0345-8

Shangguan Q, Prody A, Wirth TS, Briggs EM, Martz TR, DeGrandpre MD. 2022. An inter-comparison of autonomous in situ instruments for ocean CO2 measurements under laboratory-controlled conditions. *Marine Chemistry* **240**(104085). Elsevier. doi: 10.1016/j.marchem.2022.104085

Shipley K. 2022. Biogeochemical observations and baseline CO2 conditions in the Agua Hedionda Lagoon. University of California San Diego.

Shipley K, Martz T, Bresnahan P, Wirth T. 2022. Data from: Metabolic rates in the Agua Hedionda Lagoon during the 2020 Southern California red tide event. UC San Diego Library Digital Collections. doi: 10.6075/j0mk6d3g

Smith S, Hollibaugh J. 1993. Coastal metabolism and the Oceanic organic carbon balance. *Reviews of Geophysics* **31**(1): 75–89. doi: 10.1029/92rg02584

Takeshita Y, Martz TR, Johnson, Kenneth S. Dickson AG. 2014. Characterization of an ion sensitive field effect transistor and chloride ion selective electrodes for pH measurements in seawater. *Analytical Chemistry* **86**(22): 11189–11195. doi: 10.1021/ac502631z

Tromp TK, Van Cappellen P, Key RM. 1995. A global model for the early diagenesis of organic carbon and organic phosphorus in marine sediments. *Geochimica et Cosmochimica Acta* **59**(7): 1259–1284. doi: 10.1016/0016-7037(95)00042-x

Wanninkhof R. 2014. Relationship between wind speed and gas exchange over the ocean revisited. *Limnology and Oceanography: Methods* **12**: 351–362. doi: 10.4319/lom.2014.12.351

Windham-Myers L, Cai W-J, Alin SR, Andersson A, Crosswell J, Dunton KH, Hernandez-Ayon JM, Herrmann M, Hinson AL, Hopkinson CS, Howard J, Hu X, Knox SH, Kroeger K, Lagomasino D, Megonigal P, Najjar RG, Paulsen M-L, Peteet D et al. 2018. Tidal wetlands and estuaries. Second state of the carbon cycle report (SOCCR2): A sustained assessment report. doi: 10.7930/soccr2.2018.ch15